

APPLICATIONS OF STRUCTURE-FROM-MOTION
PHOTOGRAMMETRY TO FLUVIAL
GEOMORPHOLOGY

by

JAMES THOMAS DIETRICH

A DISSERTATION

Presented to the Department of Geography
and the Graduate School of the University of Oregon
in partial fulfillment of the requirements
for the degree of
Doctor of Philosophy

December 2014

DISSERTATION APPROVAL PAGE

Student: James Thomas Dietrich

Title: Applications of Structure-from-Motion Photogrammetry to Fluvial Geomorphology

This dissertation has been accepted and approved in partial fulfillment of the requirements for the Doctor of Philosophy degree in the Department of Geography by:

Mark Fonstad	Chairperson
Patricia McDowell	Core Member
Christopher Bone	Core Member
Joshua Roering	Institutional Representative

and

J. Andrew Berglund	Dean of the Graduate School
--------------------	-----------------------------

Original approval signatures are on file with the University of Oregon Graduate School.

Degree awarded December 2014

© 2014 James Thomas Dietrich

This work is licensed under a Creative Commons
Attribution-NonCommercial-NoDerivatives 4.0 International License



DISSERTATION ABSTRACT

James Thomas Dietrich

Doctor of Philosophy

Department of Geography

December 2014

Title: Applications of Structure-from-Motion Photogrammetry to Fluvial Geomorphology

Since 2011, Structure-from-Motion Multi-View Stereo Photogrammetry (SfM or SfM-MVS) has gone from an overlooked computer vision technique to an emerging methodology for collecting low-cost, high spatial resolution three-dimensional data for topographic or surface modeling in many academic fields. This dissertation examines the applications of SfM to the field of fluvial geomorphology. My research objectives for this dissertation were to determine the error and uncertainty that are inherent in SfM datasets, the use of SfM to map and monitor geomorphic change in a small river restoration project, and the use of SfM to map and extract data to examine multi-scale geomorphic patterns for 32 kilometers of the Middle Fork John Day River. SfM provides extremely consistent results, although there are systematic errors that result from certain survey patterns that need to be accounted for in future applications. Monitoring change on small restoration stream channels with SfM gave a more complete spatial perspective than traditional cross sections on small-scale geomorphic change. Helicopter-based SfM was an excellent platform for low-cost, large scale fluvial remote sensing, and the data extracted from the imagery provided multi-scalar perspectives of downstream patterns of channel morphology. This dissertation makes many recommendations for better and more

efficient SfM surveys at all of the spatial scales surveyed. By implementing the improvements laid out here and by other authors, SfM will be a powerful tool that will make 3D data collection more accessible to the wider geomorphic community.

CURRICULUM VITAE

NAME OF AUTHOR: James Thomas Dietrich

GRADUATE AND UNDERGRADUATE SCHOOLS ATTENDED:

University of Oregon, Eugene, Oregon
Texas State University-San Marcos, San Marcos, Texas
University of Kansas, Lawrence, Kansas

DEGREES AWARDED:

Doctor of Philosophy, Geography, 2014, University of Oregon
Master of Science, Geography, 2008, Texas State University-San Marcos
Bachelor of Science, Physical Geography, 2006, University of Kansas

AREAS OF SPECIAL INTEREST:

Structure-from-motion and close-range remote sensing methods
Fluvial geomorphology
Remote sensing of rivers
Open source software and hardware for remote sensing and environmental monitoring

PROFESSIONAL EXPERIENCE:

Neukom Postdoctoral Fellow, William H. Neukom Institute for Computational Science, Dartmouth College, Hanover, New Hampshire, 2014 - 2017
Doctoral Teaching Fellow, Department of Geography, University of Oregon, Eugene, 2011 – 2014
Doctoral Teaching Assistant, Department of Geography, Texas State University-San Marcos, San Marcos, Texas, 2010 – 2011
Senior Remote Sensing Analyst & Cartographer. Jeppesen Sanderson, Inc. – a Boeing Company, Englewood, Colorado, 2008 – 2010
Graduate Teaching Assistant, Department of Geography, Texas State University-San Marcos, San Marcos, Texas, 2006 – 2008
Technical Research Assistant, Kansas Geological Survey, Lawrence, Kansas, 2003 – 2006

GRANTS, AWARDS, AND HONORS:

Outstanding Student Paper Award, Hydrology Section, American Geophysical Union Fall Meeting, 2012

PUBLICATIONS

Fonstad, M. A., J.T. Dietrich, B.C. Courville, J.L. Jensen, and P.E. Carbonneau. 2013. Topographic structure from motion: a new development in photogrammetric measurement. *Earth Surface Processes and Landforms*. 38(4): 421–430. DOI: 10.1002/esp.3366

ACKNOWLEDGMENTS

I would like to thank all the people that have helped me make it through graduate school successfully. Mark Fonstad, for being an amazing advisor and agreeing to tote me along to Oregon. Pat McDowell, for welcoming me to Oregon with open arms and providing me with the opportunity to work in the beautiful Middle Fork John Day River. Chris Bone, for providing the right balance of GIScience and practical professional advice. Josh Roering, for your different perspective on geomorphology and your enthusiasm for all of the new toys we were playing with.

The Confederated Tribes of the Warm Springs of Oregon for providing access to the Oxbow Conservation Area and its amazing facilities. Brian Cochran, of the Tribes, for providing data and planning and executing a major restoration project that I could use for my research. Mark Croghan, of the Bureau of Reclamation for taking a huge chance and providing funding for the helicopter flight. The Oregon Watershed Enhancement Board (OWEB) for funding the other portions my work in the Middle Fork. The Middle Fork IMW working group for data sharing and all their support/suggestions. Troy Woydziak of Baker Aircraft for taking on a crazy aerial photography mission and executing it perfectly. Michael Olsen and John Raugust from Oregon State University for collecting and processing the TLS data. Carl Legleiter for the stream normal coordinate transformation code and Patrice Carbonneau for the hyperscale graph code.

The River Rats past and present for all your support and friendship. Sonja, for being a great friend and an amazing administrator who had all the right answers at all the right times. My family, Mom and Dad, Teresa and Mike for your support and advise on this long trip.

For my wonderful wife, Maggie.
Who has supported me through it all.

TABLE OF CONTENTS

Chapter	Page
I. INTRODUCTION.....	1
II. ACCURACY, UNCERTAINTY, AND REPEATABILITY OF STRUCTURE- FROM-MOTION PHOTOGRAMMETRIC DATASETS	6
Introduction.....	6
Data and Methods.....	8
Study Areas	8
SfM Processing.....	9
Uncertainty and Repeatability	10
TLS Comparison	14
Results.....	16
Repeatability.....	16
Uncertainty	16
TLS Comparison	19
Discussion.....	23
Uncertainty and Repeatability	23
TLS Comparison	24
Conclusions.....	30
III. FIRST YEAR GEOMORPHIC MONITORING OF THE GRANITE BOULDER CREEK STREAM RESTORATION PROJECT.....	32
Introduction.....	32
Background.....	34
Study Area	37
Data and Methods.....	40
Results.....	44
Discussion.....	49
Conclusions.....	56
IV. SUB-METER REMOTE SENSING FOR RIVERSCAPE MAPPING WITH HELICOPTER-BASED STRUCTURE-FROM-MOTION PHOTOGRAMMETRY	57
Introduction.....	57
Background.....	58
Study Area	61
Data and Methods.....	63
Aerial Photography Collection	63
Riverscape Data Extraction and Analysis	67
Habitat Mapping.....	71
Results.....	72
Aerial Photography.....	72
Riverscape Mapping.....	76

Chapter	Page
Habitat	80
Discussion.....	83
Aerial Photography.....	83
Riverscape Mapping.....	87
Habitat	91
Conclusions.....	92
V. SUMMARY	94
APPENDIX: DATA MANAGEMENT.....	99
REFERENCES CITED.....	100

LIST OF FIGURES

Figure	Page
1. Overview of the site, Cummins Creek in the background.	11
2. Cummins Creek study area	12
3. Views of the lawn and Weatherford Hall facade (left) and Mary's River bar and cut bank (right).....	15
4. Boxplots showing the distribution of errors for each dataset. The boxes represent the median and interquartile range.....	18
5. Spatial distribution of error for all 250 validation points. DEM provided in the background for reference.	18
6. Weatherford Hall lawn SfM - TLS comparison; SfM natural color point cloud (top left), M3C2 difference map (top right), significant differences (bottom left), and histogram of M3C2 differences (zero highlighted in black, bottom right)	20
7. Weatherford Hall facade SfM - TLS comparison; SfM natural color point cloud (top left), M3C2 difference map (top right), significant differences (bottom left), and histogram of M3C2 differences (zero highlighted in black, bottom right)	21
8. Mary's River bar SfM - TLS comparison; SfM natural color point cloud (top left), M3C2 difference map (top right), significant differences (bottom left), and histogram of M3C2 differences (zero highlighted in black, bottom right)	22
9. Mary's River cut bank SfM - TLS comparison; SfM natural color point cloud (top left), M3C2 difference map (top right), significant differences (bottom left), and histogram of M3C2 differences (zero highlighted in black, bottom right)	22
10. Point density comparison for the lawn study site, TLS (left) and SfM (right). The color ramps are equivalent.	28
11. Point density comparison for a 2m by 2m area of the lawn.....	29
12. Overview of the upper Middle Fork John Day River. The watershed of Granite Boulder Creek is highlighted.	38

Figure	Page
13. Before and after aerial photography of the Oxbow Conservation Area showing the impact of dredge mining and the initial restoration on Granite Boulder Creek and the Middle Fork John Day River. Images from. USGS (1939, 1949), Bureau of Reclamation (2006), and the author (2013).	39
14. Close up aerial photography of the newly constructed channel for Granite Boulder Creek. RTK-GPS cross-section sites are shown.	40
15. SfM survey patterns used in this study, divergent in stream survey for 2012 (left) and convergent bank survey for 2013 (right).	42
16. 2012 - 2013 change in the five RTK-GPS cross-sections.	46
17. 2012 - 2013 change in the longitudinal profile elevations (top) and planform position of the thalweg (bottom).	47
18. SfM - GPS cross section comparisons for XS 1, XS 2, and XS 3.	49
19. SfM - GPS cross section comparisons for XS 4 and XS 5.	50
20. SfM M3C2 difference results for XS 1 with orthophotos for reference. Flow is right to left.	51
21. SfM M3C2 difference results for XS 2 with orthophotos for reference. Flow is right to left.	52
22. SfM M3C2 difference results for XS 3 with orthophotos for reference. Flow is right to left.	53
23. SfM M3C2 difference results for XS 4 and XS 5 with orthophotos for reference. Flow is right to left.	54
24. Map of the upper Middle Fork John Day River, with study area highlighted by the labeled river segments.	62
25. Helicopter aerial photography setup. Canon T5i in the vibration-isolating mount with GPS and intervelometer (upper left). Robinson R44 helicopter at takeoff (upper right). Examples of ground control targets, 1-meter tarps (lower left) and roadside painted targets (lower right).	65
26. Sample orthophotograph located in segment E. The Middle Fork is at the bottom of the photo and tributary is the recently reconstructed Granite Boulder Creek. Flow is right to left.	73
27. Sample DEM of the same area as Figure 3.	74

Figure	Page
28. Examples of the effects of missing photo coverage (left) and orthorectification artifacts (right).	74
29. Map of SfM - LiDAR differences showing systematic errors in the SfM data from the parallel camera geometry and abrupt edges from incomplete coverage. Flow is right to left.	77
30. Primary morphologic variables for the study area. Dotted lines represent river segment breaks, labels are at the top.	78
31. Derived hydrologic variables for the study area. Dotted lines represent river segment breaks, labels are at the top.	79
32. Boxplot of the distribution of active channel widths for each river segment.	80
33. Boxplot of active channel widths for each of the classified channel units. N-values are the number of samples in each class (total = 10,776).....	81
34. Boxplot of active channel widths for the different bedrock geologies. N-values are the number of samples in each class (total = 10,776).....	81
35. Boxplot of the distributions of valley widths for the different bedrock geologies. N-values are the number of samples in each class (total = 10,776).....	82
36. Boxplot of the distributions of active channel widths for each of the current cattle grazing intensities. N-values are the number of samples in each class (total = 10,776).....	82
37. Boxplot of the distribution of active channel widths for the different river restoration treatments. N-values are the number of samples in each class (total = 10,776).....	83
38. Hyperscale graph of Pearson correlation coefficients of active channel width as a function of downstream distance. White areas within the triangle are portions of the analysis that did not meet the significance criteria ($p = 0.05$).....	84
39. Hyperscale graph of Pearson correlation coefficients of active channel width as a function of slope. White areas within the triangle are portions of the analysis that did not meet the significance criteria ($p = 0.05$).	85
40. Hyperscale graph of Pearson correlation coefficients of active channel width as a function of valley width. White areas within the triangle are portions of the analysis that did not meet the significance criteria ($p = 0.05$).	86

Figure	Page
41. Downstream plot of habitat suitability index (HSI) for upstream migrating Chinook salmon.	87
42. Comparison of topographic survey methods and their typical extents and resolutions. ALS = Airbourne LiDAR, rtkGPS = real-time kinematic global positioning system, SfM = Structure-from-Motion, TLS = Terrestrial Laser Scanning, TS = Total Station (After Bangen et al., 2014).....	97

LIST OF TABLES

Table	Page
1. Consistency photoset descriptions	11
2. Georeferencing accuracies reported by Photoscan for the nine photoset combinations	11
3. TLS and SfM dataset comparison.....	14
4. Coefficient of determination (R^2 , below the diagonal), and RMSE (in cm, above the diagonal) for pairwise linear regressions of SfM z values for comparisons of 500 random sample points from all 36 DEM combinations.	16
5. Error statistics for all georeferencing tests and photosets, all value are in cm.	17
6. M3C2 point cloud difference statistics for the four study sites	23
7. River segment details.....	64
8. River segment detail, continued. Human modification codes: CS = channel straightening, DM = dredge mining, G = grazing. Restoration activity codes: RP = riparian planting, LW = large wood placment, CM = channel modification.	64
9. Error, accuracy, and uncertainty for SfM georeferencing (top) and the post-processed GPS points (bottom).....	75

CHAPTER I

INTRODUCTION

Since 2011, Structure-from-Motion Multi-View Stereo Photogrammetry (SfM or SfM-MVS) has gone from an overlooked computer vision technique to an emerging methodology for collecting low-cost, high spatial resolution three-dimensional data for topographic or surface modeling in many academic fields. Some of the applications have included geomorphology (Fonstad et al., 2013; Javernick et al., 2014; Westoby et al., 2012), volcanology (James and Robson, 2012; James and Varley, 2012), forestry and precision agriculture (Dandois and Ellis, 2013; Mathews and Jensen, 2013) and outside the geosciences, in fields like archeology (Koutsoudis et al., 2013, 2014). In geomorphology, SfM has the potential to be a powerful addition to the three-dimensional remote sensing toolkit alongside traditional stereo photogrammetry, terrestrial laser scanning (TLS), and airborne LiDAR (ALS). These tools are being used to construct high-quality digital terrain models in an ever growing number of settings (Brasington et al., 2000; Heritage and Hetherington, 2007; Lague et al., 2013; Lane and Chandler, 2003; Marcus and Fonstad, 2010; Wheaton et al., 2010)

The origins of SfM are from the field of computer vision, beginning with Ullman (1979) and evolving into the current iterations of algorithms (Agarwal et al., 2010; Furukawa and Ponce, 2010; Snavely, 2008; Snavely et al., 2006, 2007). The core concept of SfM is the science of photogrammetry, using photographs to make quantitative measurements of the scene they represent (McGlone and Lee, 2013; Sharp, 1951). In traditional photogrammetry, two overlapping images (a stereo pair) are taken with a

calibrated (metric) camera(s). By knowing the internal camera geometry, lens distortions, and the distance between photos (parallax), the stereo perspective allows users to calculate the distance from the camera to objects in the photographs using trigonometry. Digital photogrammetry software can make thousands of measurements in a stereo pair, building up a three-dimensional dataset of the scene. The downside of this type of photogrammetry is that users need *a priori* knowledge of the exact camera positions, the internal camera geometry, and lens distortions. Stereo photogrammetric datasets also suffer from shadowing, which are areas of missing data from obstructions in the instrument's line of sight. SfM operates in a similar manner, but instead of using two overlapping images, SfM uses multiple (three or more) images to solve the trigonometry and extract the three-dimensional dataset. These multiple views offer three advantages over stereo photogrammetry. SfM is able to back-calculate the relative camera positions so that exact camera locations do not need to be known *a priori*. A non-metric camera can be used to collect imagery, which reduces the cost of collecting imagery, but the internal camera geometry and lens distortions have to be estimated with simplified models. The multiple views allow for multiple trigonometric measurements that help reduce the error in each 3D point that comes from the simplified camera and lens geometries models. Finally, by collecting multiple views of all sides of an object or scene users can eliminate shadowing in the final dataset.

Beyond stereo photogrammetry, SfM also has some distinct advantages over TLS and ALS that make it ideal for a wide range of geomorphic research. The first advantage of SfM is the cost of the instrument. For SfM, researchers can collect imagery with just about any off-the-shelf digital camera, ranging from \$100 for a basic point-and-shoot to

\$1000 for a mid-range digital single lens reflex (SLR) camera, compared to TLS and ALS systems that cost upward of \$10,000. The second advantage is SfM flexibility to capture data at a wide range of spatial scales. TLS has a minimum detection distance of roughly 1 meter and a maximum distance of 500 meters, while ALS is used primarily for large area surveys. SfM has been used to capture 3D models of archeological artifacts a few centimeters long (Koutsoudis et al., 2013) and up to areas tens of kilometers square (see Chapter IV).

The basic SfM workflow produces two datasets, a sparse point cloud and a dense point cloud. SfM produces the sparse point cloud in its initial alignment stage; these points are both the result of the initial trigonometric measurements and used to help align all of the camera positions. After all of the cameras are coarsely aligned, the sparse point cloud is used to optimize the camera positions through a bundle adjustment process (Hartley and Zisserman, 2003). After the alignment stage, dense matching algorithms are used to increase the volume of photogrammetrically measured points (Furukawa and Ponce, 2010). For smaller area SfM surveys ($10^1 - 10^2 \text{ m}^2$) sparse point clouds have an average density of 10 to 100 points per square meter and dense point clouds can easily reach densities of thousands to tens of thousands of points per square meter. One of the disadvantages of the way that SfM reconstructs a scene is that it does so in an arbitrary coordinate system, meaning that the relative distances between camera locations and all of the 3D points are consistent, but not metric. To transform the model from arbitrary space to metric/geographic space, multiple ground control points are needed throughout the scene. Advanced workflows can interpolate the point clouds into surface models and create topographically corrected mosaic orthophotographs. The surface models can be

produced using standard GIS data models, triangulated irregular networks (TIN) or raster DEM or advanced CAD-based volumetric models, voxels (volumetric pixels) or tetrahedral network (TEN) data models.

My research objectives for this dissertation were three-fold, and relate to the three main chapters in this volume. The first objective was to determine the error and uncertainty that are inherent in SfM datasets. The second objective was to use SfM to map and monitor geomorphic change in a small river restoration project, and thirdly use SfM to map and extract data to examine multi-scale geomorphic patterns for 32 kilometers of the Middle Fork John Day River.

In Chapter II, I examine the consistency, error, and uncertainty associated with SfM datasets at scales of $10^1 - 10^2$ square meters. Understanding the sources and magnitude of error and uncertainty are important in being able to interpret the results of any change detection between two terrain datasets because SfM is a new method and establishing these values is important for future geomorphic change detection studies.

Chapter III explores first year geomorphic changes in the Granite Boulder Creek stream restoration project and the application of SfM as a 3D geomorphic monitoring tool. The channel of Granite Boulder Creek, where it meets the Middle Fork John Day, was destroyed by dredge mining in the Middle Fork valley during 1939 -1942. In 2012, the Confederated Tribes of the Warm Springs Reservation of Oregon (CTWSRO), as part of a larger restoration effort, constructed a new channel for Granite Boulder Creek, connecting it to the main stem of the Middle Fork. I used RTK-GPS cross-sections and longitudinal profiles from the CTWSRO and my own SfM surveys to look at changes in the newly constructed channel between 2012 and 2013.

In Chapter IV, I used a digital SLR camera mounted on a helicopter to collect aerial imagery for 32 km of the Middle Fork John Day River, from Bates State Park downstream to Jungle Creek, in order to examine larger spatial scale applications of SfM. My goal was to create a high-resolution digital terrain model and orthophotos using SfM and use these to extract spatially contiguous datasets of river morphology. Using a combination of statistical methods, including hyperscale analysis, I examine the current downstream patterns in channel morphology and how they relate to the imprint of human modification on the river and the effects of those modifications on Chinook salmon habitat.

This research will contribute to several fields, beginning with the science of SfM and its use in geomorphic applications. By determining the inherent error and uncertainty in SfM datasets, geomorphologists and others that use SfM for change detection will have a better understanding of the limitation of SfM when used for change detection. The lessons learned from the application of SfM at two different spatial scales will help improve survey methodologies for future studies. The second field this research will contribute to is stream restoration monitoring. The data from this chapter are important baseline data for future studies on Granite Boulder Creek that will evaluate the success of the project and help inform the design and monitoring of future restoration projects. Lastly, by testing new techniques for data collection and assessing how well those data integrate with established data analysis methods, SfM could provide a new dimension to fluvial remote sensing.

CHAPTER II
ACCURACY, UNCERTAINTY, AND REPEATABILITY OF
STRUCTURE-FROM-MOTION PHOTOGRAMMETRIC DATASETS

Introduction

Structure-from-Motion and multi-view stereo photogrammetry (SfM or SfM-MVS) have been a recent addition to the three-dimensional topographic data collection toolkit in the geosciences. Since 2012 there has been an explosion of the application of SfM to fields like geomorphology (Fonstad et al., 2013; Javernick et al., 2014; Westoby et al., 2012), volcanology (James and Robson, 2012; James and Varley, 2012), and outside the geosciences, in fields like archeology (Koutsoudis et al., 2013, 2014). SfM-MVS is a photogrammetric technique that allows users to produce high-resolution point cloud datasets from multiple overlapping photographs. A majority of the development of SfM has been in the field of computer vision beginning with Ullman (1979). The current generation of SfM has primarily come from research at the University of Washington (Agarwal et al., 2010; Furukawa and Ponce, 2010; Snavely et al., 2007; Szeliski and Kang, 1994). The details of the SfM-MVS process have been extensively reviewed elsewhere and will not be covered here (Fonstad et al., 2013; James and Robson, 2012; Javernick et al., 2014; Westoby et al., 2012).

With any new method, it is important to quantify the inherent error in the technique so the limits can be established. Given the recent emergence of SfM, most studies have focused on the error and accuracy in individual datasets (e.g. Westoby et al., 2012) and not between repeat datasets. By comparing the accuracy and error across

multiple SfM datasets collected over the same area in quick succession, I can establish the uncertainty that underlies the method. It is important to establish uncertainty levels for topographic data collection methods because the quality of topographic datasets influences the accuracy of data that are derived from them, which include topographic parameters as simple as slope and aspect to more complex derivatives like geomorphic change detection (Lane et al., 2003; Wechsler and Kroll, 2006). My first objective for this research was to ascertain the repeatability and uncertainty in SfM datasets at spatial scales of tens of meters ($10^1 - 10^2$ meters). I compared multiple SfM datasets collected over one site to examine how consistent or repeatable SfM point clouds are and then used those data to calculate a spatially uniform uncertainty estimate as a first step toward understanding the uncertainties in SfM datasets. The second objective applied the calculated uncertainty to a comparison of SfM data against a comparable 3D surveying technology, terrestrial laser scanning (TLS) at different study site. By comparing these two 3D surveying techniques as independent datasets, it is possible to assess how the uncertainty in SfM might affect the results of a possible change detection study that uses multiple data collection methods.

Repeat topographic datasets are an important part of geomorphology because they allow researchers to quantify rates of change and can help infer process (James et al., 2012; Wheaton et al., 2010). Topographic datasets have differing amounts of uncertainty associated with them depending on the method used to collect the data (Bangen et al., 2014). As with a lot of the terminology that geographers use to describe the quality of their data, the term uncertainty is borrowed from statistics (Taylor, 1997; Mowrer, 2000). The basic definition of measurement uncertainty from Taylor (1997) is $x_{best} \pm \delta x$, with

x_{best} representing the researcher's best estimate of the true value and $\pm\delta x$, the range of uncertainty in the measurement. By Taylor's definition, uncertainty equals the error in a measurement and if multiple measurements are made, the standard deviation of error between the measured and actual value is a good estimate of the uncertainty (Taylor, 1997). In the geospatial literature, uncertainty has come to embody more than just error in individual measurements. It has evolved to become an umbrella term for all of the potential measures of data quality that encompasses all of the error that is propagated through to the final data outputs (Zhang and Goodchild, 2002; Longley et al., 2011).

If uncertainty is not accounted for in change detection studies, it can cause over- or under-estimation in the magnitude of change, which can lead to the misinterpretation of the results (Milan et al., 2011; Wheaton et al., 2010). A variety of methods have been used to calculate uncertainty to differentiate insignificant change, which lies within the range of uncertainty and statistically significant change, which exceeds the uncertainty level. These include spatially uniform uncertainty estimates (Brasington et al., 2000, 2003; Lane et al., 2003) and spatially variable estimates of uncertainty (Wheaton et al., 2010; Legleiter et al., 2011; Milan et al., 2011; Lague et al., 2013).

Data and Methods

Study Areas

This research used multiple study areas because of the availability of the TLS system used for the second research objective. The datasets for the first portion of this study were collected at the mouth of Cummins Creek at Neptune State Park on the central Oregon Coast. For the SfM/TLS comparison the data were collected on the campus of

Oregon State University in Corvallis, Oregon and on the Mary's River in Philomath, Oregon.

SfM Processing

For the SfM datasets used in this study, I collected large sets of overlapping photographs (photosets) with a Canon T5i digital SLR camera (18-55mm lens, fixed at 18mm focal length). The photographs for the larger ground areas were collected with the camera mounted on a pole that extended to 4.5 meters and tilted down to take photographs at ~35 degrees off-nadir. Photographs for the vertical surfaces in the TLS comparisons were collected by hand without the use of the pole. After collecting each photoset, I examined each photo by eye and removed blurry photographs and any with duplicate adjacent images. I processed the photosets using the commercial SfM software PhotoScan Professional v.1.0.4 by Agisoft (Agisoft LLC, 2014). All of the photosets were processed with the same workflow in Photoscan using the default settings (for version 1.0.4) at each step. The photo alignment was processed with the high quality setting, pair pre-selection disabled, and with a point limit of 40,000. Georeferencing was accomplished using 20 cm checkerboard-style targets placed in regularly spaced grid pattern throughout the study area(s). I collected the position of the ground control points (GCP) with a Topcon GR-3 RTK GNSS base and rover in UTM coordinates. The ground control points had an average horizontal and vertical RMS error of 0.9 cm. The initial georeferencing in Photoscan is a linear 7-parameter Helmert transformation using the default measurement accuracy settings. To refine the initial georeferencing and optimize the camera alignment for non-linear distortions, a calibrated camera model was applied to the aligned cameras. The next step was to create a dense point cloud reconstruction. For

point cloud comparisons, the dense point cloud was exported to the LAS file format. For the GIS outputs, it was necessary to create a TIN mesh over the dense point cloud. From the TIN, a raster DEM was exported from Photoscan as a GeoTIFF file. The TIN can also be used to create and export ortho-rectified photo-mosaics.

Uncertainty and Repeatability

To test the uncertainty and repeatability of SfM, I chose to collect data at a spatial scale of tens of meters to represent a typical bar-scale survey in fluvial geomorphology. The study area was an area approximately 20 meters by 15 meters at the mouth of Cummins Creek at Neptune Beach State Park, south of Yachats, Oregon (Figure 1). The area was a mix of packed sand, coarse gravel, and small woody debris. I collected three photosets over the study area using two different out-and-back patterns similar to traditional aerial photography flight lines (Table 1). The photosets were collected in quick succession to ensure that there was no perceptible change in the surface. Twenty GCPs were visible in the study area and an additional 250 validation points were collected to assess the uncertainty in SfM outputs (Figure 2).

Because uncertainty and repeatability in the SfM outputs are linked to the accuracy of the georeferencing and optimization steps, I processed each photoset with three different combinations of ground control points, resulting in nine total datasets. The first georeferencing test case (T1) was georeferenced using the four corner GCPs, the second (T2) added two additional points (one each in the middle of the north and south edges), and the third (T3) used all twenty GPCs (Table 2). Each of the nine resulting datasets were exported from Photoscan as GeoTIFF raster DEMs with a cell size of 0.005 meters to retain the detail present in the dense point cloud.

Table 1: Consistency photoset descriptions

	Pattern direction	# of photos	Point Cloud Size (Density)	Output DEM resolution
Photoset #1 (PS1)	North-South	131	68 million (226k pts / m ²)	0.5 cm
Photoset #2 (PS2)	East-West	161	64 million (216k pts / m ²)	0.5 cm
Photoset #3 (PS3)	East-West	167	66 million (221k pts / m ²)	0.5 cm

Table 2: Georeferencing accuracies reported by Photoscan for the nine photoset combinations

Georeferencing Test	Photoset	X error (cm)	Y Error (cm)	Z Error (cm)	Total RMS Error (cm)
T1	PS1	0.9	0.6	1.1	1.6
T1	PS2	0.8	0.3	0.8	1.2
T1	PS3	0.7	0.6	0.8	1.3
T2	PS1	1.1	0.6	1.6	2.1
T2	PS2	1.0	0.5	1.4	1.8
T2	PS3	1.0	0.6	1.4	1.9
T3	PS1	1.5	0.9	1.4	2.3
T3	PS2	1.4	0.8	1.6	2.3
T3	PS3	1.5	0.8	1.2	2.1



Figure 1: Overview of the site, Cummins Creek in the background.

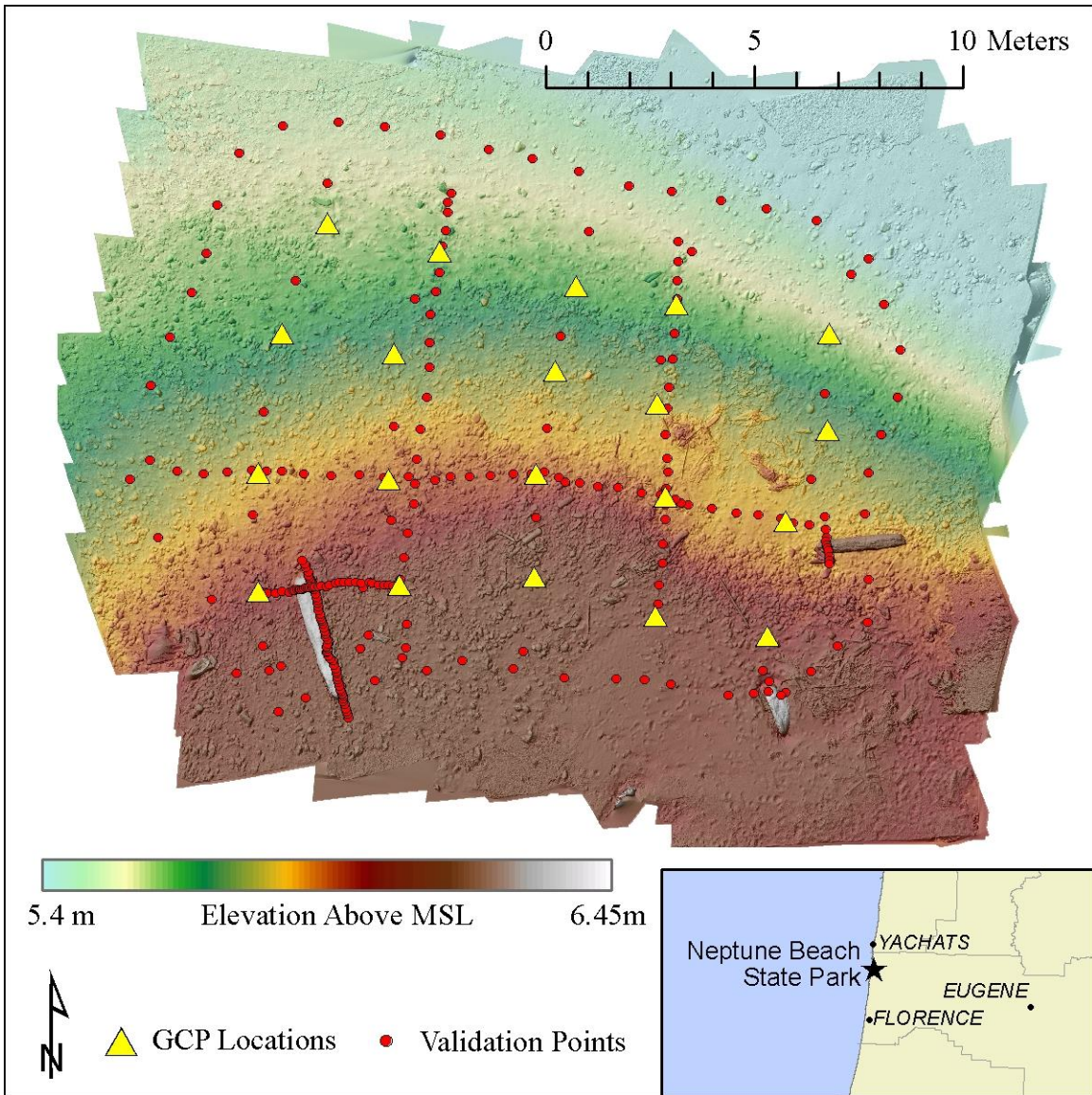


Figure 2: Cummins Creek study area

Testing the repeatability of SfM also has important implications for its usefulness in change detection studies. If the SfM process cannot produce consistent results, its usefulness as a survey technique should be called into question. By creating 500 random points within the study area and extracting the values of the nine DEMs to each point, it was possible to assess the repeatability of SfM. The average coefficient of determination (R^2) and average adjusted RMSE were calculated to test the repeatability between photosets within the confines of each georeferencing test case. Constructing a correlation

matrix allowed for the testing of repeatability across all of the datasets, which permitted the evaluation of the correlation coefficients and RMSE values between all of the 36 possible combinations of DEMs.

To calculate the elevation uncertainty in each dataset, I used several statistical measures based on the elevation error between the GPS elevation and the nine DEM elevations for each of the 250 GPS validation points, $\Delta z = \text{SfM}(z) - \text{GPS}(z)$. The two primary statistical measures of uncertainty are the standard deviation of the error distribution (Eq. 1) and adjusted root mean squared error of a linear regression of GPS elevations versus SfM elevations (Eq. 2) (Taylor, 1997).

$$s = \sqrt{\frac{1}{N} \sum_{i=1}^N (x_i - \bar{x})^2} \quad (1)$$

$$\text{Adj. RMSE} = \sqrt{\frac{1}{n-1} \sum_{i=1}^N (\hat{y}_i - y_i)^2} \quad (2)$$

In Equation 1, s is the standard deviation, N is the number of observations, x_i are the observed values, and \bar{x} is the mean. For Equation 2, n is the total number of observations, \hat{y}_i are the predicted values from a linear regression of GPS elevations versus SfM elevations, and y_i are the actual, SfM, observation values. Additional statistical measures of accuracy and precision are the mean error and mean absolute error, which illustrate any statistical bias in the data and overall magnitude of the errors (Butler et al., 1998; Chandler, 1999; Lane et al., 2000). The global statistics are an important measure of the global error in these datasets. The spatial distribution of error in these datasets is an important indicator of any spatial bias in the data. To test for any broad spatial patterns in

the error, I mapped the error values for the 250 validation points for each of the nine datasets.

TLS Comparison

Terrestrial laser scan and SfM data were collected at two sites, each with a horizontal and vertical component. A Riegl VZ-400 scanner with a Trimble R8 network-RTK GNSS receiver collected the TLS data at both sites. Previous studies comparing TLS and SfM data (i.e James and Quinton, 2014; Westoby et al., 2012) co-registered the SfM and TLS using common GCPs. For this study, the goal was to compare the accuracy of SfM to an independently collected TLS dataset. Therefore, the SfM data were georeferenced with GCPs collected with a Topcon RTK GNSS system and the TLS data were georeferenced with a Trimble network-RTK receiver mounted on the instrument. The first site was a lawn (approximately 50 m by 50 m) and adjacent building (the southeastern façade of Weatherford Hall, 60 m wide by 30 m tall) on the campus of Oregon State University in Corvallis, Oregon. The second site was a bar and cut bank combination on the Mary’s River in Philomath, Oregon. The bar measured 50 m by 16 m and the cut bank 10 m wide by 4.5 m high. Representative site photos are shown in Figure 3 and comparisons on the raw data (SfM and TLS) are outlined in Table 3.

Table 3: TLS and SfM dataset comparison

		TLS	SfM
Lawn	Number of TLS Stations / SfM Photos	5	471
	Number of Points	12.2 million	104.9 million
Building	Number of TLS Stations / SfM Photos	Same 5 as Lawn	130
	Number of Points	2.4 million	28.9 million
Bar	Number of TLS Stations / SfM Photos	3	170
	Number of Points	4.7 million	21.2 million
Cut Bank	Number of TLS Stations / SfM Photos	1	55
	Number of Points	698,500	1.4 million



Figure 3: Views of the lawn and Weatherford Hall facade (left) and Mary's River bar and cut bank (right)

To take advantage of the full point cloud resolution of both the TLS and SfM datasets, I used the Multiscale Model to Model Cloud Comparison (M3C2) method developed by Lague et al. (2013) to assess the differences between each of the four datasets. The M3C2 method allows the user to calculate the cloud-to-cloud distances based on the local orientation of the points relative to the surface normal (a vector perpendicular to the surface), which creates accurate comparisons of the differences in the point clouds in a true 3D environment. In addition to the signed differences between the point clouds, M3C2 can calculate a spatial variable confidence interval to determine areas of significant difference using uncertainty associated with each point cloud. Uncertainty in the point clouds is calculated as a function of the surface roughness in the immediate neighborhood of a point (local surface roughness) and a spatially uniform registration error. To account for differences in the GPS systems, errors in the TLS point cloud registration (Olsen et al., 2009) and the SfM uncertainty, a uniform registration error of 2 cm was included into the M3C2 calculations.

Results

Repeatability

Although there are differences in the uncertainty statistics, the repeatability results (Table 4) show that SfM produces consistent results with all of the datasets, exhibiting agreement at 99.7% or better, with most comparisons having sub-centimeter RMSE values. Within each georeferencing test, the agreement between photosets was very good; for both T1 and T2 the average R^2 was 0.9996 and the average RMSE was 0.6 cm, while the T3 photosets have slightly less agreement with an average R^2 of 0.9985 and a RMSE of 0.84 cm.

Table 4: Coefficient of determination (R^2 , below the diagonal), and RMSE (in cm, above the diagonal) for pairwise linear regressions of SfM z values for comparisons of 500 random sample points from all 36 DEM combinations.

		T1	T1	T1	T2	T2	T2	T3	T3	T3
		PS1	PS2	PS3	PS1	PS2	PS3	PS1	PS2	PS3
T1	PS1	-	0.572	0.643	0.321	0.723	0.780	1.211	1.003	0.914
T1	PS2	0.9993	-	0.596	0.620	0.514	0.662	1.122	0.727	0.975
T1	PS3	0.9991	0.9992	-	0.661	0.636	0.400	0.897	0.942	0.986
T2	PS1	0.9998	0.9992	0.9991	-	0.587	0.683	1.093	0.960	0.805
T2	PS2	0.9989	0.9994	0.9992	0.9993	-	0.525	0.923	0.739	0.867
T2	PS3	0.9987	0.9991	0.9997	0.9990	0.9994	-	0.809	0.885	0.968
T3	PS1	0.9970	0.9974	0.9983	0.9975	0.9982	0.9987	-	0.971	0.803
T3	PS2	0.9980	0.9989	0.9982	0.9981	0.9989	0.9984	0.9981	-	0.775
T3	PS3	0.9983	0.9980	0.9980	0.9987	0.9985	0.9981	0.9987	0.9988	-

Uncertainty

The overall error statistics for all of the SfM datasets are shown in Table 5. In this table there is a range of small negative biases in the SfM datasets, with mean errors ranging from sub-millimeter (-0.07 cm) to the centimeter (-1.68 cm) scale. These values suggest that there is a systematic component to the error in these datasets in addition to random error. The ranges of the uncertainty metrics (standard deviation and RMSE) are

all relatively narrow and show that the magnitude of error in all of the datasets is consistent (as seen in the boxplots in Figure 4). The different surveying patterns seem to have a small effect on uncertainty. The PS1 datasets, with their North-South orientation, have consistently larger mean errors and larger uncertainties than the East-West oriented PS2 and PS3. The georeferencing tests also show variation; the T1 datasets have the lowest average mean error, but the T3 datasets utilizing all 20 GCPs had the largest uncertainties and the highest mean errors.

The spatial distribution of error (Figure 5) shows a pronounced pattern of positive errors in the middle of the study area and negative errors at the edges. The balancing of the positive and negative errors explain the near-zero mean errors for most of the datasets. The strong negative mean errors in the T3 datasets are a result of the minimization of positive errors in the center and an increase in the negative errors at the edges.

Table 5: Error statistics for all georeferencing tests and photosets, all value are in cm.

<i>All values in cm</i>		Mean Error (ME)	Mean Abs. Error (MAE)	St. Dev. Error (σ)	RMSE	R ²
T1	PS1	-0.23	1.72	2.13	1.97	0.995
T1	PS2	-0.07	1.56	1.93	1.84	0.995
T1	PS3	-0.18	1.58	2.12	2.05	0.994
T1 Average		-0.16	1.62	2.06	1.95	0.995
T2	PS1	-0.91	1.70	1.97	1.92	0.995
T2	PS2	-0.73	1.44	1.70	1.70	0.996
T2	PS3	-0.74	1.50	1.81	1.80	0.996
T2 Average		-0.79	1.55	1.83	1.80	0.996
T3	PS1	-1.68	2.14	2.11	2.07	0.994
T3	PS2	-1.67	2.06	2.01	2.01	0.995
T3	PS3	-1.35	1.63	1.63	1.63	0.997
T3 Average		-1.57	1.94	1.92	1.90	0.995
Overall Average		-0.84	1.70	1.94	1.88	0.995

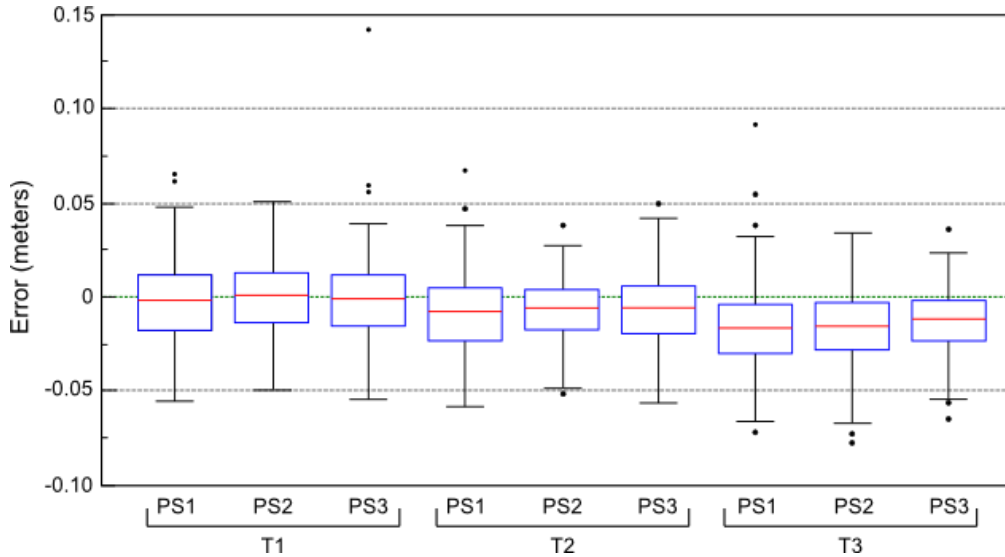


Figure 4: Boxplots showing the distribution of errors for each dataset. The boxes represent the median and interquartile range.

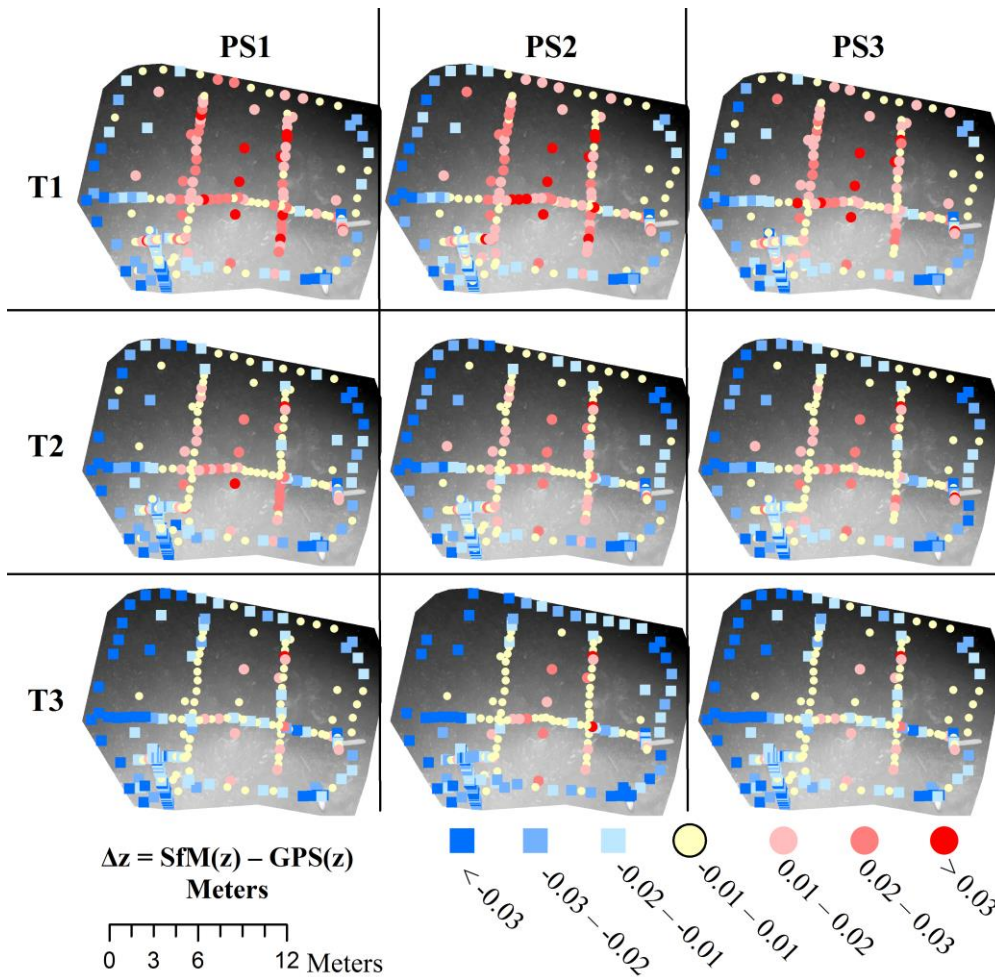


Figure 5: Spatial distribution of error for all 250 validation points. DEM provided in the background for reference.

TLS Comparison

The M3C2 results for the lawn are shown in Figure 6. For all of the TLS/SfM comparisons, the difference is SfM minus TLS so that positive values indicate that the SfM point cloud is above the TLS and negative values indicate that the SfM points are below the TLS points. The small missing areas in the northwest corner of the lawn was the result of incomplete photo coverage for that portion of the dataset and the hexagonal shapes are the TLS scanning locations where the TLS point density was lower. The mean difference between the TLS and SfM point clouds was -0.07 cm with a standard deviation of 2.38 cm and a mean absolute difference of 1.84 cm. From the M3C2 statistics on significance, only 8% of the compared area was statistically significantly different.

The façade of Weatherford Hall had considerably larger and had more varied discrepancies (Figure 7), which are reflected in the difference statistics. The mean difference was 5.06 cm with a standard deviation of 27.07 cm and an absolute mean difference of 9.55 cm. The uniform difference in the center part of the façade suggests a systematic offset in the range of 1 to 2 cm. Large trees shadowed the areas on either side of the center section, which also had lower numbers of contributing photos, leading to the larger differences. The systematic offset and large differences in this scene contributed to over 50% of the points classified as significantly different.

The Mary's River bar results (Figure 8) show that the SfM data are consistently lower by 2 to 4 cm compared to the TLS with the exception of the eastern edge that has a slight positive difference (1-2 cm). The area of significant difference along the south edge of the bar relates to the area of the bar that also has the lowest TLS point density. The cut bank (Figure 9), like the building, had higher difference values compared to its adjacent

bar surface. The high difference values at the top of the cut bank are the result of overhanging vegetation.

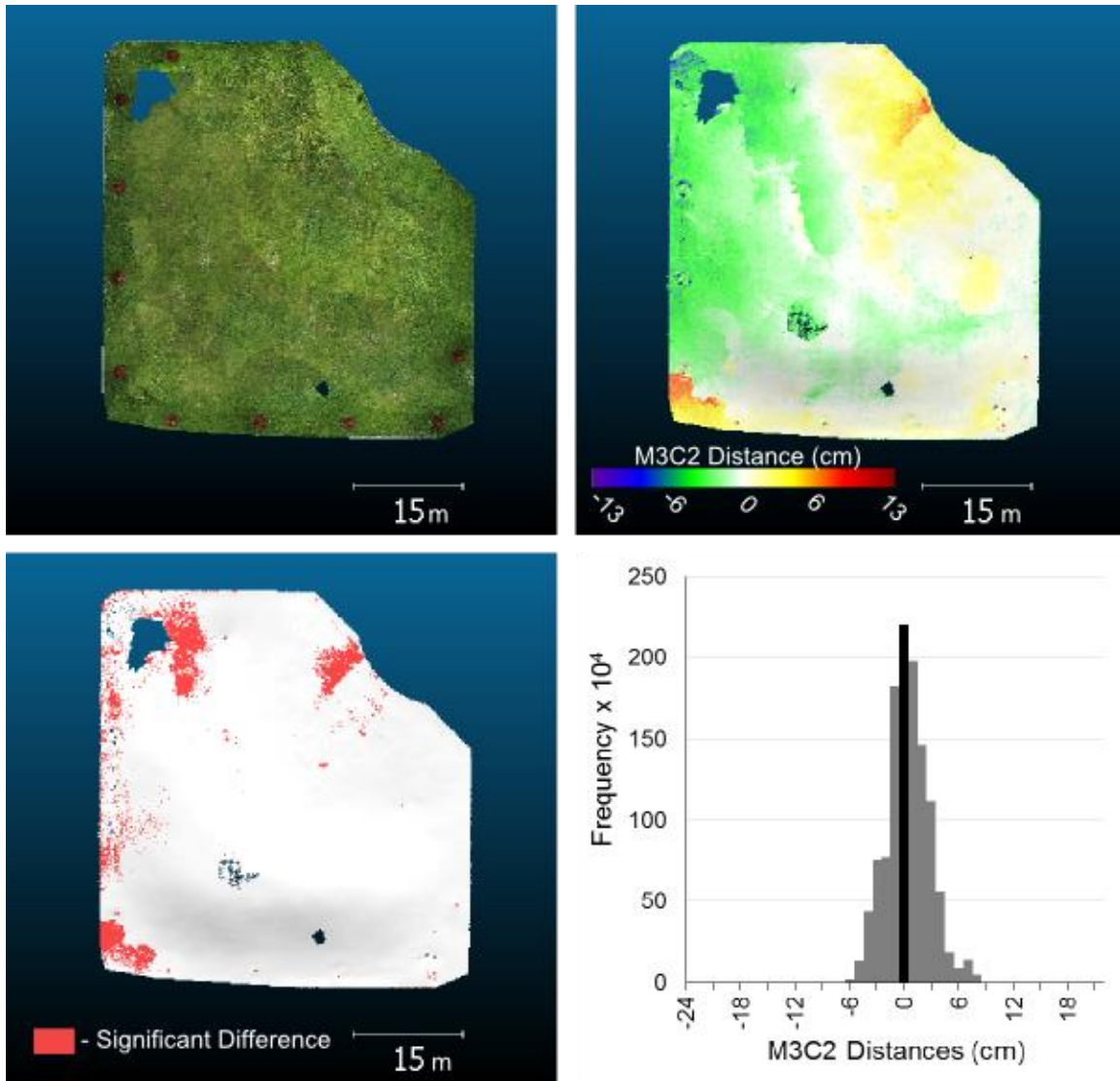


Figure 6: Weatherford Hall lawn SfM - TLS comparison; SfM natural color point cloud (top left), M3C2 difference map (top right), significant differences (bottom left), and histogram of M3C2 differences (zero highlighted in black, bottom right)

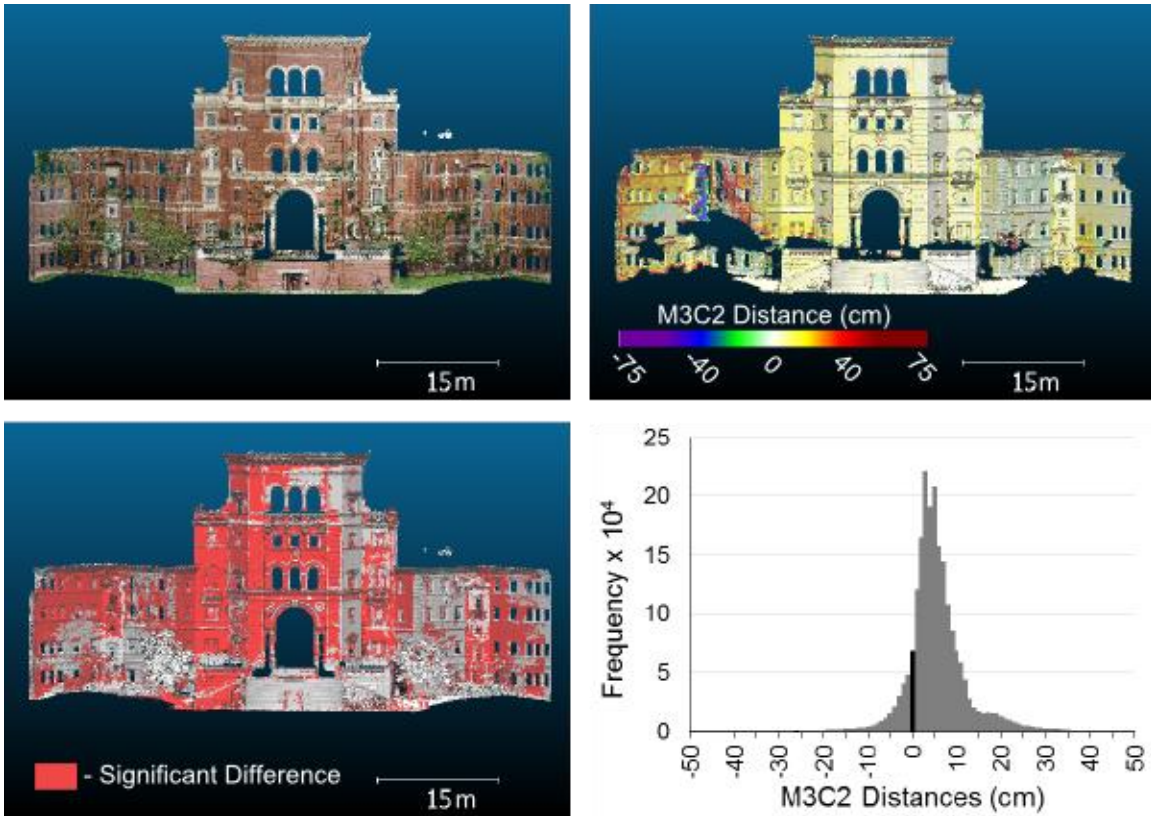


Figure 7: Weatherford Hall facade SfM - TLS comparison; SfM natural color point cloud (top left), M3C2 difference map (top right), significant differences (bottom left), and histogram of M3C2 differences (zero highlighted in black, bottom right)

The Mary's River bar results (Figure 8) show that the SfM data are consistently lower by 2 to 4 cm compared to the TLS with the exception of the eastern edge that has a slight positive difference (1-2 cm). The area of significant difference along the south edge of the bar relates to the area of the bar that also has the lowest TLS point density. The cut bank (Figure 9), like the building, had higher difference values compared to its adjacent bar surface. The high difference values at the top of the cut bank are the result of overhanging vegetation. The overall SfM/TLS point cloud difference statistics for the four TLS sites are shown in Table 6

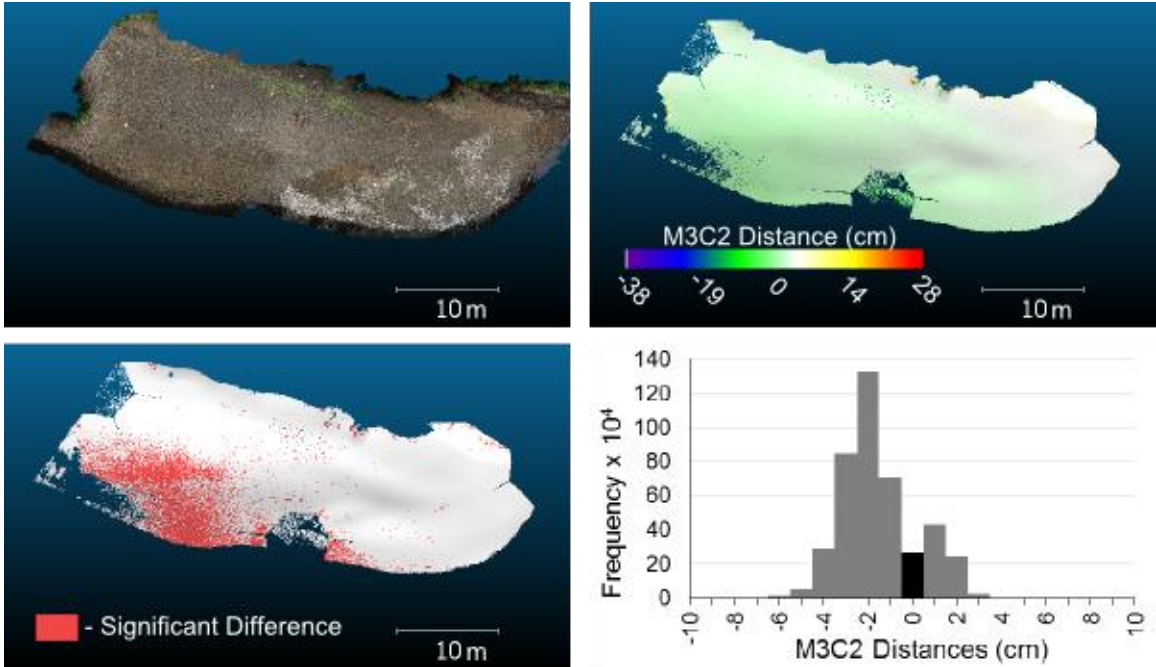


Figure 8: Mary's River bar SfM - TLS comparison; SfM natural color point cloud (top left), M3C2 difference map (top right), significant differences (bottom left), and histogram of M3C2 differences (zero highlighted in black, bottom right)

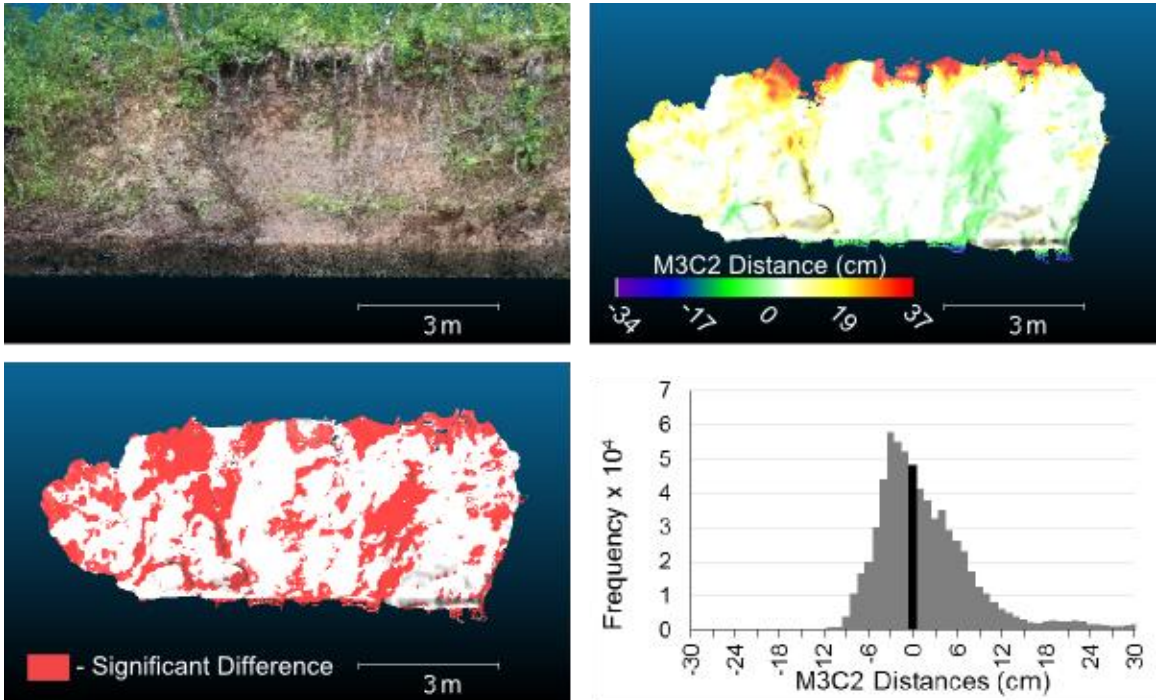


Figure 9: Mary's River cut bank SfM - TLS comparison; SfM natural color point cloud (top left), M3C2 difference map (top right), significant differences (bottom left), and histogram of M3C2 differences (zero highlighted in black, bottom right)

Table 6: M3C2 point cloud difference statistics for the four study sites

	Mean Difference	Standard Deviation	Mean Absolute Difference	Significant Difference
Lawn	-0.07 cm	2.38 cm	1.84 cm	8.1%
Building	5.06 cm	27.07 cm	9.55 cm	54.2%
Bar	-2.01 cm	1.77 cm	0.23 cm	7.8%
Cut bank	1.63 cm	7.62 cm	5.28 cm	42.9%

Discussion

Uncertainty and Repeatability

The range of values for each of the uncertainty metrics is quite small; the mean absolute error has a range of 0.7 cm, the range of the standard deviation is 0.5 cm, and the RMSE a range of 0.4 cm. The differences between the georeferencing tests are small, but it appears that the T1 results are an outcome of a georeferencing solution where the number of GCPs is not sufficient to provide a robust transformation. This is in contrast to the T3 results, where the large number of GCPs provide an accurate transformation in the areas that they cover while increasing the error outside the GCPs.

The negative bias in the mean error and the spatial patterns of error (Figure 5) suggest that there is a systematic component to the errors. These radial error patterns are like those described by James and Robson (2014) and similar to those seen by Woodget et al. (2014) and Ouédraogo (2014) and are the result of a combination of factors. The major contributing causes are the strict parallel camera orientations and an incomplete or incorrect camera/lens calibration (James and Robson, 2014; Ouédraogo et al., 2014). Radial distortion in camera lenses, especially those with wider fields of view, will cause non-linear artifacts in the SfM reconstructions, and by utilizing parallel camera orientations the software cannot correctly optimize the reconstruction to eliminate the

radial distortions. In Photoscan, the optimization step is meant to correct these non-linear distortions in the 3D surface models. When using an incorrect or incomplete calibration the radial errors can persist into the final outputs. As Ouédraogo (2014) points out, Photoscan uses a 3-parameter lens calibration model rather than a more complex calibration model that could help reduce the non-linear distortions. Additional errors in SfM reconstructions can come from the fewer number of overlapping photos at the edges of the study area. The points derived from the photos along the edges have less robust photogrammetric solutions and can be prone to higher errors (Yuan, 2009).

Despite the systematic error associated with lens distortion, SfM does produce extremely consistent datasets. The amount of uncertainty in this study is comparable to the study conducted by James and Robson (2012), who reported an RMSE of 3.6 cm on a slightly larger study area. These results also demonstrate a precision comparable to other topographic surveying techniques (Bangen et al., 2014). As long as uncertainty is accounted for and the systematic errors corrected, SfM will be a reliable source of high-resolution 3D topographic data for change detection studies. The high R^2 and low RMSE values (Table 4) along with the uncertainty statistics (Table 5) show that the variation between datasets are low and there is a high-level of consistency. These results are for SfM reconstructions using Agisoft Photoscan, but other software packages use different algorithms and different camera calibration models (James and Robson, 2012, 2014; Ouédraogo et al., 2014), which will likely result in different uncertainty values.

TLS Comparison

Overall, the SfM datasets compared favorably to the TLS datasets. The key differences were that the horizontal SfM surfaces performed much better than the vertical

surfaces. Another important observation is the lack of systematic radial errors like those seen in the Neptune Beach SfM data. If the lens distortion/camera calibration errors were consistent, then we would expect to see similar radial error patterns (Figure 5) when differencing the SfM and TLS datasets. Because the TLS comparison photosets were not collected with a strictly parallel orientation, optimization corrected the radial distortion.

For the lawn dataset, the spatial pattern of differences can be broken into two sections, separated by a northeast to southwest dividing line. The differences in the southeastern half of the lawn seem to be mostly random, while the northwest half has some larger positive and negative differences (approximately ± 3 cm). These differences can be partially attributed to error in the GCPs used to georeference the SfM. The average vertical RMS (VRMS) for several of the GCP exceeded 2 cm; these points were close to the building and the high VRMS was probably the result of a lower GNSS satellite count and multipathing off the building. There are also two areas (labeled A and B in Figure 6) that show abrupt changes in the difference values. These areas are small errors in the SfM point cloud that resulted from the misalignment of several photos, causing the photogrammetric points associated with those photos to be above/below the mean elevation of the neighboring points.

The other horizontal surface, the bar on the Mary's river, also lacks any signal of radial distortion. The differences here show a more uniform pattern, with a negative bias except for the area surrounding the most easterly TLS scan location, which shows a slight positive bias. The histogram of the differences for this site clearly shows (Figure 8) these biases. These differences do not correlate with the GPS VRMS error despite being under

a moderate canopy of cottonwood trees as the points with significant differences are concentrated in the areas of lower TLS point density.

Both of the vertical surfaces, the cut bank at the Mary's River site and the façade of Weatherford Hall, had considerably higher differences. One of the shared attributes of both of these sites was the lack of control points on the vertical surfaces. The photographs for both of these sites were processed in conjunction with the photographs of horizontal surfaces and tied into the same ground control points used to georeference the horizontal surfaces. Most of the building façade was 20 meters away from the nearest control points and the cut bank was across the channel and approximately 15 meters away from the control points on the bar. The distance to the nearest control points and the lack of control points on the vertical surface contributed to larger errors associated with the georeferencing of the SfM models and in turn resulted in larger variations when compared to the TLS. For future SfM reconstructions of large vertical surfaces, it will be important to have control points on the surfaces; this will require the use of a total station to collect GCPs rather than GPS. An additional consideration for large vertical surface mapping with SfM is that photographs can only be collected from one angle so it is important to collect from a variety of angles to the subject to create a better SfM reconstruction.

Many of the small-scale differences between the SfM and TLS datasets are at the scale of GPS error (1-2 cm). Because of the independent GPS units used to georeference the two datasets, the differences can be partially attributed to variability in error between the two GPS units and not systematic errors in either dataset. This is an important factor in establishing the propagation of errors and uncertainty when trying to establish areas of

statistically significant differences between two datasets. Considering the uncertainty that exists in the GPS, TLS, and SfM datasets, I would suggest a larger limit of detection (Brasington et al., 2000; Milan et al., 2011; Wheaton et al., 2010), 3-4 cm, for establishing a threshold for statistically significant differences between TLS and SfM datasets.

One of the most fundamental differences between the TLS and SfM datasets is the density of the collected data points by each method. This difference is most apparent at the lawn site (Figure 10) where the total number of points are an order of magnitude different (104 million for SfM versus 12.2 million for TLS) and the average point density is almost two orders of magnitude different. The TLS densities are highest adjacent to scanner locations and become lower as a function of distance from the scanner, with densities in between scanner locations ranging from an average 500 to 3,000 points·m⁻². The SfM point densities have a more uniform distribution, with overall mean density of 56,000 points·m⁻². The variations in the SfM densities are associated with the number of overlapping photos and pattern used to collect the photographs. Lague et al. (2013) suggest that point density differences affect the calculation of point cloud to point cloud differences and that density differences will also affect the calculation of significant change in the M3C2 algorithm. The point densities may also be contributing to some of the variations we see between the datasets. In a 4 m² area of the lawn (Figure 11), the point density difference show that SfM is capturing more of the microtopography of the grass surface than the TLS. This is a function of how these distinct survey technologies are sensing the landscape. The laser pulses from the TLS intersect horizontal surfaces, like the grass, at an acute angle that results in a shadowing effect, which limits the

sensing of the fine-scale microtopography. The near-nadir viewing angle of the SfM photographs gives a better overall perspective and allows for the extraction of SfM points, which precisely capture the microtopography. These differences in density and viewing angles, which affect resolution and precision, could account for some of the vertical differences between the TLS and SfM datasets and could be significant depending on the roughness of the surface.

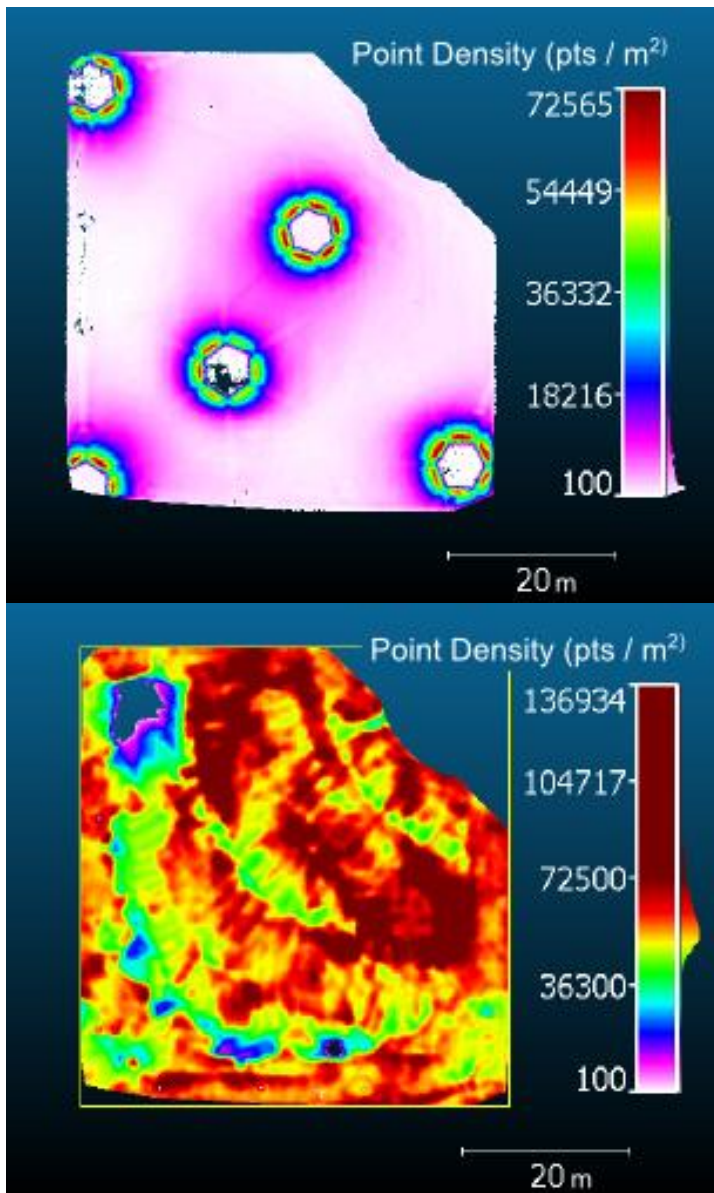


Figure 10: Point density comparison for the lawn study site, TLS (top) and SfM (bottom). The color ramps are equivalent.

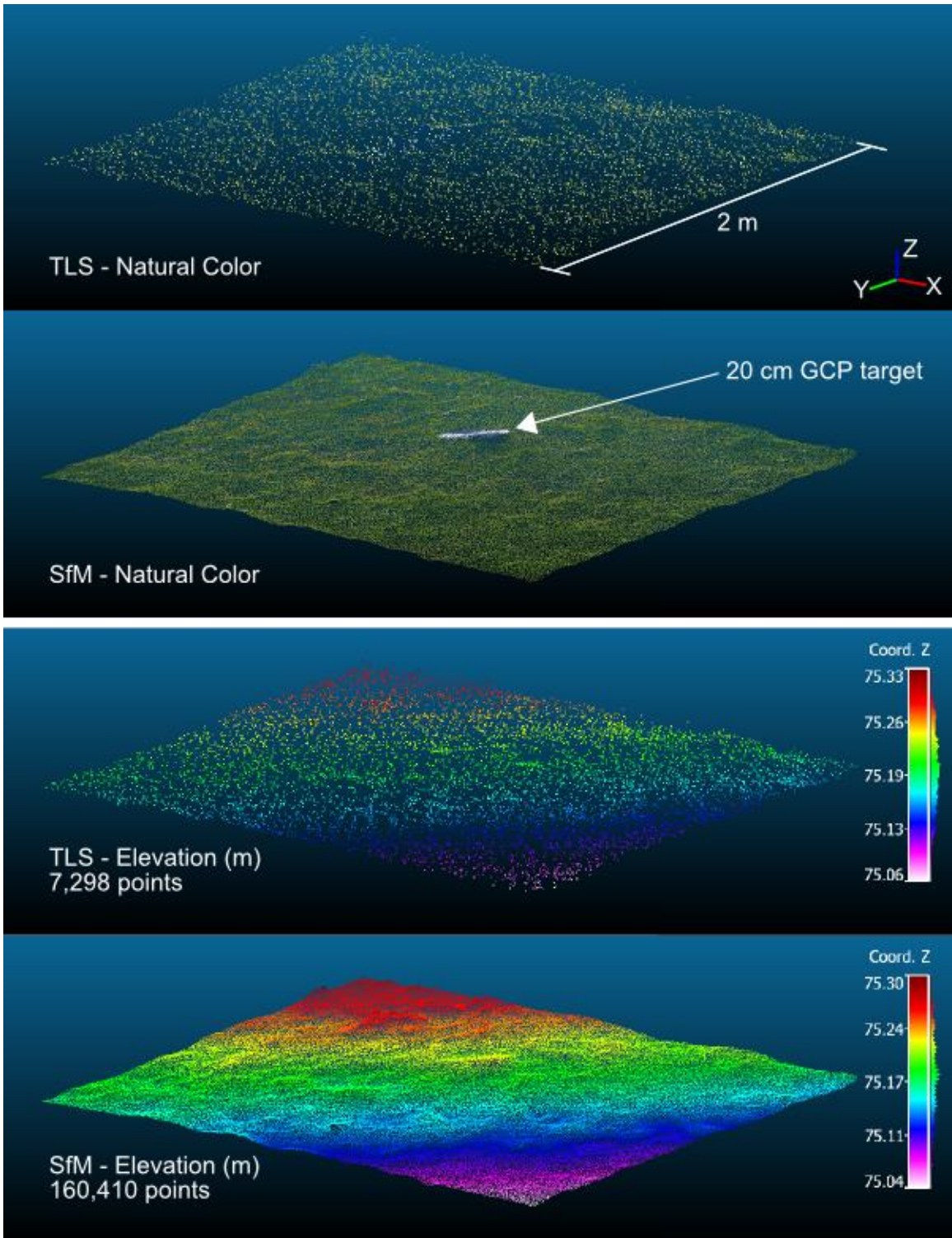


Figure 11: Point density comparison for a 2m by 2m area of the lawn.

Conclusions

In this paper, I have demonstrated that Structure-from-Motion (SfM) reconstructions of topographic surfaces at the scale of 10^1 - 10^2 meters produce extremely consistent results that make this survey method a good option for repeat topographic surveys. The topographic surfaces exhibited an average uncertainty of approximately two centimeters, which in this case includes a pronounced systematic distortion resulting from the survey method and camera calibration. This level of uncertainty is in line with other high spatial resolution survey methods and is probably sufficient for most topographic survey applications. The uncertainty could be improved using a more convergent survey pattern to eliminate the systematic distortions. SfM and TLS are collecting comparable datasets; the one key difference is SfM produces higher point densities that make SfM a better option for applications that require a higher-level of precision. The error propagation and uncertainty in both techniques will require a larger level of detection when doing comparisons between these datasets for change detection.

This research has also given some insight into the sources of error that we need to consider when doing SfM surveys, especially blunders from incorrect photo alignment or incomplete photo coverage, the importance of accurate ground control, and the choice of survey pattern. To get a better handle on uncertainty, it will be important to do future research on the scale dependent nature of uncertainty in SfM so that accurate levels of uncertainty can be established for change detection studies at a variety of spatial scales. Additional research should also be done on the effects of the non-linear errors in SfM (James and Robson, 2014) and how differences in georeferencing affect uncertainty at different spatial scales. By conducting this research early in the development of SfM as a

3D survey technique, the community can create a simple set of “best practices” for SfM surveys, helping those getting started and help lay the groundwork for the successful future for this revolutionary technique.

CHAPTER III
FIRST YEAR GEOMORPHIC MONITORING OF THE GRANITE BOULDER
CREEK STREAM RESTORATION PROJECT

Introduction

Stream restoration in the Pacific Northwest has been driven by work to revitalize anthropogenically altered streams, enhancing the habitat for endangered salmonids (Bash and Ryan, 2002; Roni et al., 2002). The Middle Fork John Day River in east-central Oregon (the Middle Fork) has had a long history of human disturbance affecting in-stream habitat and has been recently designated as critical habitat in the Columbia River system for Chinook salmon (*Oncorhynchus tshawytscha*), Steelhead (*Oncorhynchus mykiss*), and Bull Trout (*Salvelinus confluentus*) (NOAA, 2005; U.S. Fish & Wildlife Service, 2010). The legacy of human modifications on the Middle Fork include channel modifications to increase grazable land, bank trampling and the decline in riparian vegetation from grazing cattle, logging and mill operations, and the most disruptive, dredge mining for placer deposits of gold.

As part of basin-wide restoration and conservation efforts on the Middle Fork, in 2011, the Confederated Tribes of the Warm Spring Reservation of Oregon (CTWSRO) undertook a major, multi-phase channel reconstruction project on land they owned. The goal of this project is to rehabilitate about 3 km of the Middle Fork affected by dredge mining from 1939 to 1943. Granite Boulder Creek is a significant tributary that joins the Middle Fork on the CTWSRO property at the site of the dredge mining. The mining destroyed the lower portion of Granite Boulder Creek that flowed across the floodplain,

so the creek instead drained into the remnant dredge channel. In 2012, the remnant dredge channel was filled in and Granite Boulder Creek was given a new channel through the dredge tailings to reconnect it with the main stem of the Middle Fork (Cochran, 2013).

Biological and geomorphic monitoring of the new channel is ongoing by the CTWSRO, university researchers, as well as state and federal agencies. Geomorphic monitoring is important because the physical structure of the river is the basis for lotic and riparian habitat (Gregory et al., 1991; Kondolf and Micheli, 1995) and quantifying geomorphic change provides information on rates that can be used to study process-form feedbacks (James et al., 2012; Lane et al., 1994; Wheaton et al., 2010). The CTWSRO are using traditional fluvial geomorphic survey methods, RTK-GPS cross sections and longitudinal profiles, to monitor the geomorphology of the stream. Cross-sectional surveys have two fundamental flaws. They tie the monitoring to specific sites on the river that may not be ideal locations for characterizing change as the river evolves (Lane et al., 1994). Secondly, the discrete nature of cross-sectional measurements characterizes the stream as discontinuous, not as a spatially varied system, which means that the limited extent and coarse spatial resolution are not sufficient to represent the small scale changes likely to be expressed over short time periods (1 – 10 years) (Marcus and Fonstad, 2008, 2010). The short-term changes are likely to be related to local scale changes in sediment: sorting, packing, and the formation of bed forms (textural patches, ripples, bars) (Buffington, 2012).

To increase the spatial resolution of geomorphic monitoring data, I am using Granite Boulder Creek as the test bed for a new, lost-cost photogrammetric remote

sensing technique, Structure-from-Motion (SfM). SfM has the ability to create high spatial resolution three-dimensional topographic datasets from multiple, overlapping photographs from a standard digital camera. These three-dimensional data provide a broader spatial perspective on geomorphic change than the limited scope of traditional survey methods. This paper seeks to examine the best methods to monitor geomorphic change in a newly constructed restoration channel by comparing the RTK-GPS cross-sections and 3D SfM data and to examine how these types of new channels evolve in the short-term (one year, 2012 - 2013). After my initial SfM survey in 2012, I expected to see settling and sorting of the sediment that was placed in the channel during construction, but I did not expect any major changes in the channel because the 2012 winter snowpack was below average and there were no major spring flood events.

Background

Stream restoration or rehabilitation are terms used to describe a wide spectrum of river management activities that are aimed primarily at improving the health of river corridors that have been impaired or degraded by human activities (Bennett et al., 2011; Wohl et al., 2005). To counteract the human activities, restoration projects often include ecological goals, such as improving aquatic and terrestrial wildlife habitat, geomorphic/hydrologic goals, including channel reconstruction or improving floodplain connectivity, or societal goals, like improved water quality (Kondolf and Micheli, 1995; Palmer and Allen, 2006; Wohl et al., 2005)

Stream restoration in the US has grown into a multi-billion dollar industry (Bennett et al., 2011; Bernhardt et al., 2005). One aspect that most projects are still lacking is post-project monitoring, Palmer and Allen (2006) estimated that less than ten

percent of projects include any assessment or evaluation. Post-project monitoring is critical to gauge whether the project goals are being met, assessing the long-term success or failure of a project, and informing future management actions (Bash and Ryan, 2002; Downs and Kondolf, 2002; Kondolf and Micheli, 1995; Palmer and Allen, 2006). Some of the key variables used in appraising the success or failure of a project are ecological success, stakeholder success, geomorphic success, and most importantly whether successes can be built upon and failures learned from for future restoration projects (Kondolf, 1995; Palmer et al., 2005). Bash and Ryan (2002) reported that the major impediments for post-project monitoring were budgetary (lack or insufficient funding) and insufficient personnel and time to conduct monitoring.

For geomorphic monitoring, traditional survey methods like GPS or total station are some of the most economical methods for capturing topographic information, but it takes time to achieve high spatial resolution coverage with these techniques (Bangen et al., 2014). Remote sensing techniques could provide a more efficient method for post-project monitoring than a traditional survey. These techniques would also provide managers and researchers with more holistic spatial views of projects and provide more spatial data for evaluating the geomorphic conditions and ultimately the success or failure of a project.

A majority of remote sensing technologies are inherently capital intensive, like custom aerial/satellite imagery, airborne LiDAR (ALS), and terrestrial laser scanning (TLS). The recent introduction of Structure-from-Motion photogrammetry to geomorphology could act a lower-cost bridge between traditional survey techniques and higher cost remote sensing methods (Fonstad et al., 2013; James and Robson, 2012). SfM

is based on multi-view stereo photogrammetry (MVS) and has its origins in computer vision (Ullman, 1979), which have given rise to the current iterations of SfM algorithms (Agarwal et al., 2010; Furukawa and Ponce, 2010; Hartley and Zisserman, 2003; Snavely, 2008). SfM differs from traditional stereo photogrammetry in its multi-view approach to constructing three-dimensional surface models of a scene. The multiple views (camera positions) allow for increased accuracy and precision from a standard digital camera and can achieve greater coverage of a scene by reducing shadowing, areas of missing data from obstructions in the instruments line of sight that occur with stereo photogrammetry or TLS surveys. The two basic requirements for a SfM survey are multiple overlapping photographs, as few as ten for small scenes (10^0 m^2) and many thousands for larger scenes (10^1 km^2), and in-photo ground control points to either scale or georeference the final surface models. The data outputs of the SfM process vary with the different software packages, but the basic three-dimensional data outputs are XYZ point clouds (similar to ALS and TLS data) that represent the surface/topography of a scene. Interpolating the point cloud data in three-dimensions can produce digital surface models (DSM) or be converted to two-dimensional raster digital elevation models (DEM). One additional dataset created through the SfM process are topographically corrected orthophotographs from the mosaicked input photographs. There are many software packages, both commercial, free, and open-source, to process SfM data. For a full review of the methods and details of SfM see Westoby et al. (2012), James and Robson (2012, 2014), Fonstad et al.(2013), and Javernick et al. (2014).

Study Area

Granite Boulder Creek is a medium sized tributary of the Middle Fork John Day River with a drainage area of 30.2 km² in the Greenhorn Mountains in east-central Oregon (Figure 12). The geology of the basin consists of predominantly Permian to Jurassic sedimentary, volcanic, and metamorphic rocks of the Baker Terrane accreted to North American craton. The lower elevations of the basin contain Eocene volcanic conglomerates, tuffs, and ash of the Clarno formation. The upper elevations contain early Cretaceous granitic intrusions that experienced limited alpine glaciation in the Quaternary (Ferns and Brooks, 1995; Schwartz et al., 2009).

The basin has a maximum elevation of 2472 m at Vinegar Hill down to its confluence with the Middle Fork John Day at 1136 m. The main channel length is 12.8 km with an average gradient of 0.078. Where the stream reaches the base of the Greenhorns it has formed an 0.82 km² alluvial fan before joining the Middle Fork that was mostly unaffected by the dredge mining (Jett, 1998). The stream morphology is step-pool transitioning to plane-bed and straight riffle-pool at lower elevations and the dominant grain sizes range from gravels to cobbles.

Between 1939 and 1943, a placer dredge mining operation overturned approximately 50 hectares of the Middle Fork valley floor, obliterating the last 350 meters of the channel (Figure 13). The mining left a straight, entrenched channel through the dredge tailings that bifurcated the Middle Fork; the channel on the north side of the valley (the north channel) captured Granite Boulder Creek and has been the terminus for the creek for nearly 70 years. The meandering channel on the southern side of the valley (the south channel) had a significant decrease in discharge because of the bifurcated flow.

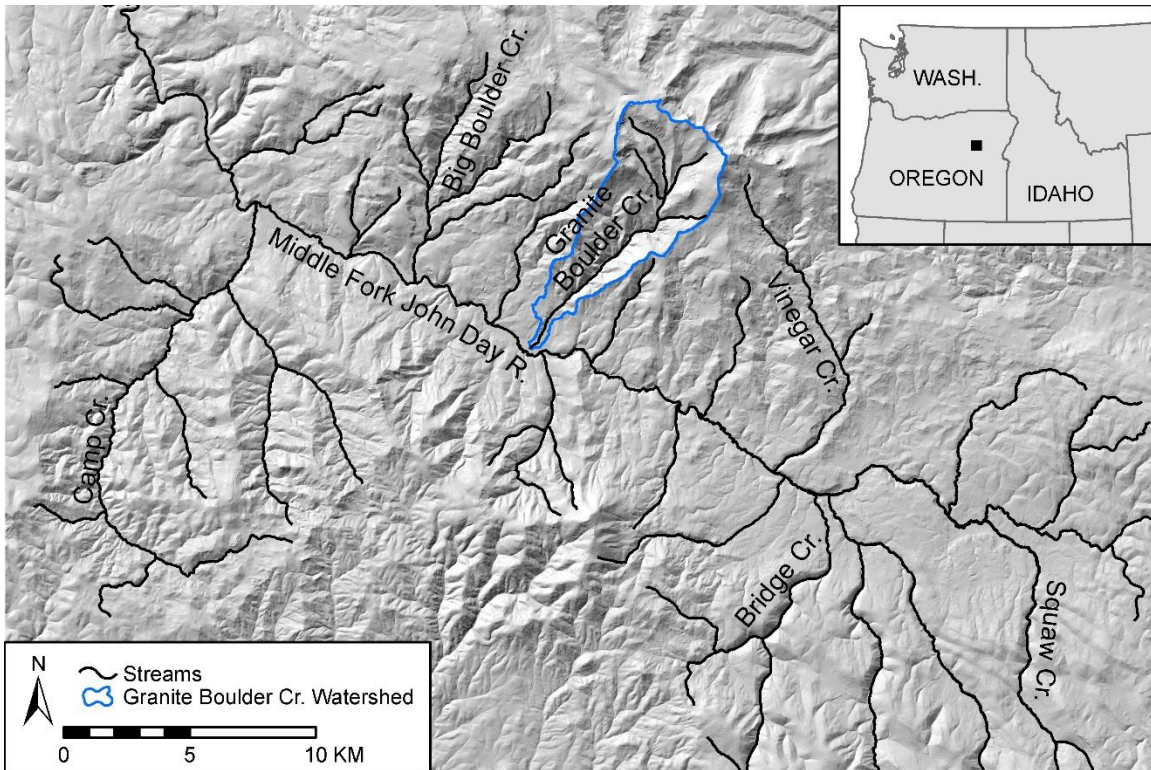


Figure 12: Overview of the upper Middle Fork John Day River. The watershed of Granite Boulder Creek is highlighted.

Until 2001, the only efforts to repair the damage to the Middle Fork valley were the smoothing of the dredge tailings to make the disturbed areas marginally better for cattle grazing. In 2001, the CTWSRO purchased the 413-hectare property as a conservation and stream restoration project site, and rechristened the property as the Oxbow Conservation Area (OCA). The CTWSRO, collaborating with federal and state government agencies, developed a three-phase restoration plan for the OCA to enhance salmonid habitat. The first phase of restoration at OCA started in 2011 and involved riparian plantings and the installation of four hundred full-size logs as engineered logjams, channel spanning and floodplain log structures along the south channel. The second phase, completed in 2012, involved filling in the north channel, reconnecting Granite Boulder Creek to the south channel, planting new vegetation along the riparian zone of Granite Boulder Creek, and regrading the dredge tailings in-between the north

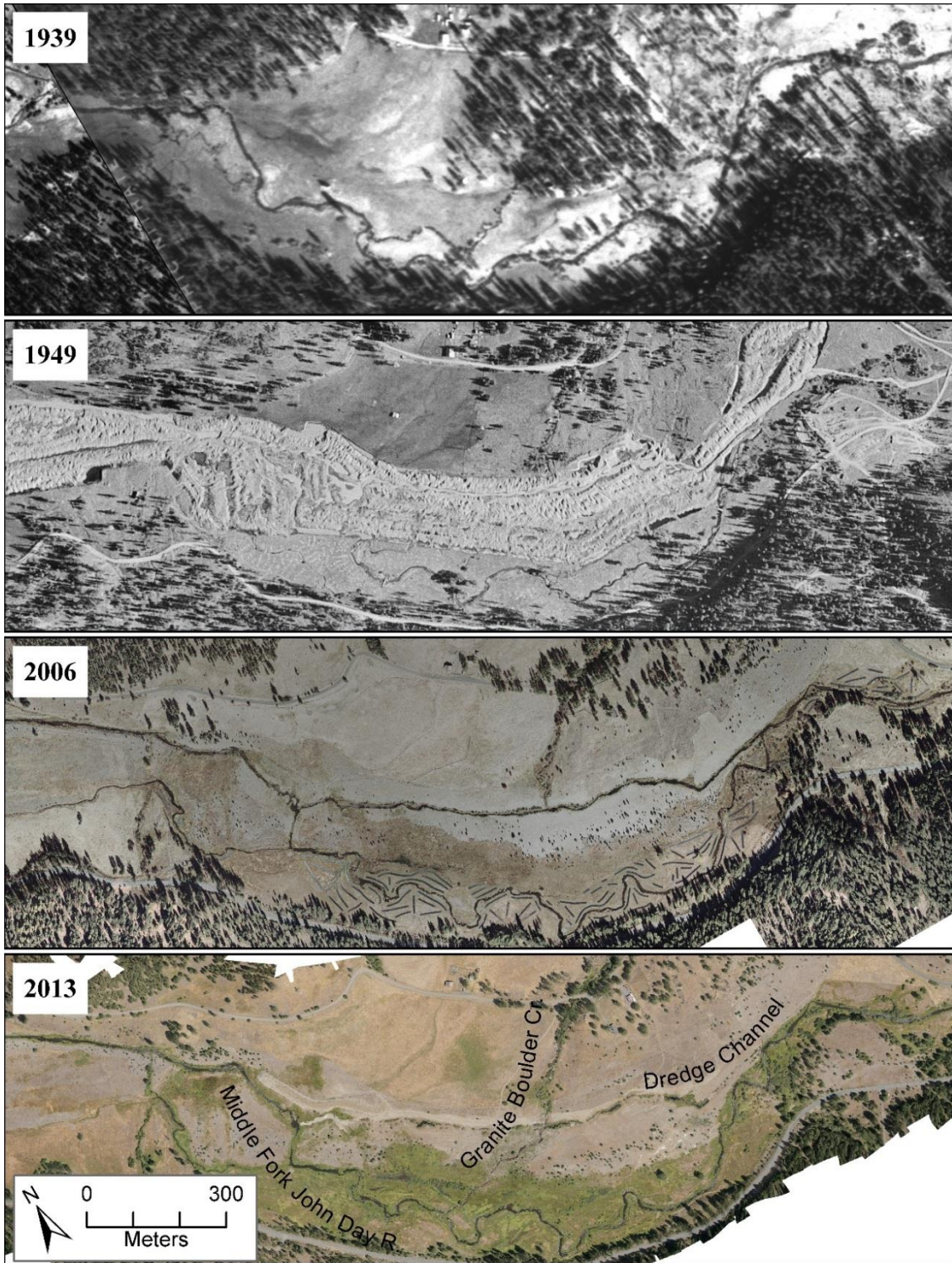


Figure 13: Before and after aerial photography of the Oxbow Conservation Area showing the impact of dredge mining and the initial restoration on Granite Boulder Creek and the Middle Fork John Day River. Images from: USGS (1939, 1949), Bureau of Reclamation (2006), and the author (2013).

and south channels to enlarge the floodplain of the south channel. The third phase began in 2014 and is focused on restoring and reconstructing the dredge affected channel of the Middle Fork downstream of Granite Boulder Creek (Cochran, 2013). By designing the new channel for Granite Boulder Creek (Figure 14) as a meandering riffle-pool channel, the goal was to return to the channel shape seen in the 1939 aerial photographs. The design incorporated carefully sorted sediments for the different channel units to mimic the sediment in the channel upstream of the dredge channel and engineered logjams throughout the new channel to promote scouring and add habitat.

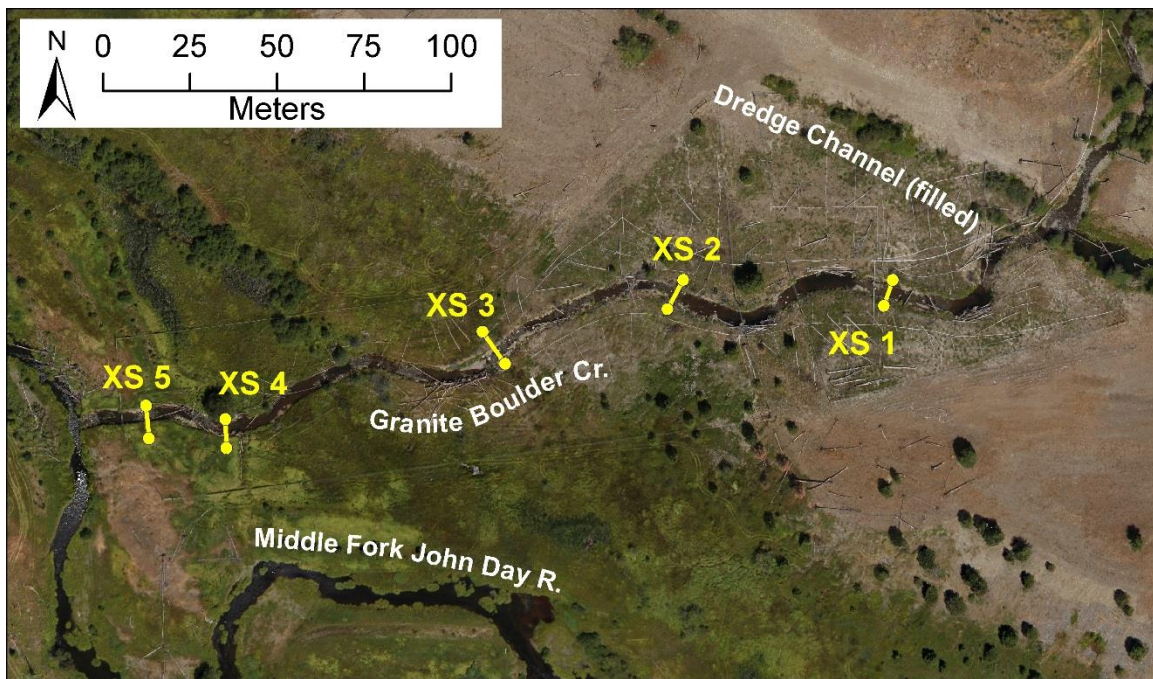


Figure 14: Close up aerial photography of the newly constructed channel for Granite Boulder Creek. RTK-GPS cross-section sites are shown.

Data and Methods

In order to examine the best methods for monitoring small restoration channels, I analyzed the CTWSRO GPS cross-section data and my own SfM data for geomorphic change between 2012, at the completion of construction, and in 2013, the first year mark

of the restoration project. These geomorphic change detection data provided information on where and what features changed in the channel and how those changes related to the evolution of the channel.

As part of their broader monitoring plan, the CTWSRO is using repeat RTK-GPS surveys at five cross-sections located at riffles and longitudinal surveys of the thalweg to evaluate the stability of the channel. Both GPS surveys were conducted in July, with each cross-section averaging 16 points, and the longitudinal surveys containing 160 points in 2012 and 133 in 2013. I evaluated each cross-section for elevation change by first converting the X and Y GPS coordinates into a stream normal coordinate system (Legleiter and Kyriakidis, 2006), which normalizes the data points into cross-stream distances from the bankfull channel centerline, and downstream distances from the upstream end of the restored channel. In the cross-sections, the GPS points for both years do not all fall along the exact same lines, making direct comparisons difficult. The stream normal coordinates mitigate these differences by allowing me to compare the GPS points by their relative positions in the cross-stream direction. The stream normal coordinate transformation also benefits the analysis of longitudinal profiles. The elevations of the channel thalweg can be compared in relation to their relative downstream distances. Differences in the cross-stream position would indicate a shift in the planform location of the thalweg. I calculated the distribution of elevation change in each cross-section and the longitudinal profiles by interpolating the GPS points and sampling the interpolated line at 10 cm intervals and differencing these samples.

I collected sets of digital photographs and GPS ground control points for SfM mapping of the entire length of the channel in August of both years. I used a Canon T5i

mounted on a 4-meter pole tilted downwards to take photographs at $\sim 35^\circ$ off-nadir. For the first series of photographs from 2012, I positioned the pole in the stream and at 1-stride increments (~ 1 meters) up the channel, and I took five divergent photographs starting with the right bank, before rotating the camera pole 45° after each photo, until the camera was facing the left bank (Figure 15). After processing the 2012 photosets there were problems reconstructing the scenes, which led to a different survey pattern in 2013 in an attempt to get more convergent camera geometry, shown to provide better imagery for SfM surveys (James and Robson, 2014). For the 2013 survey, I collected photographs at 1-stride increments from the banks with the camera aimed at the center of the channel (Figure 15). For both years, I placed checkerboard-style targets along the bank at 6-7 meter increments to georeference the SfM reconstructions and recorded their positions with an RTK-GPS.

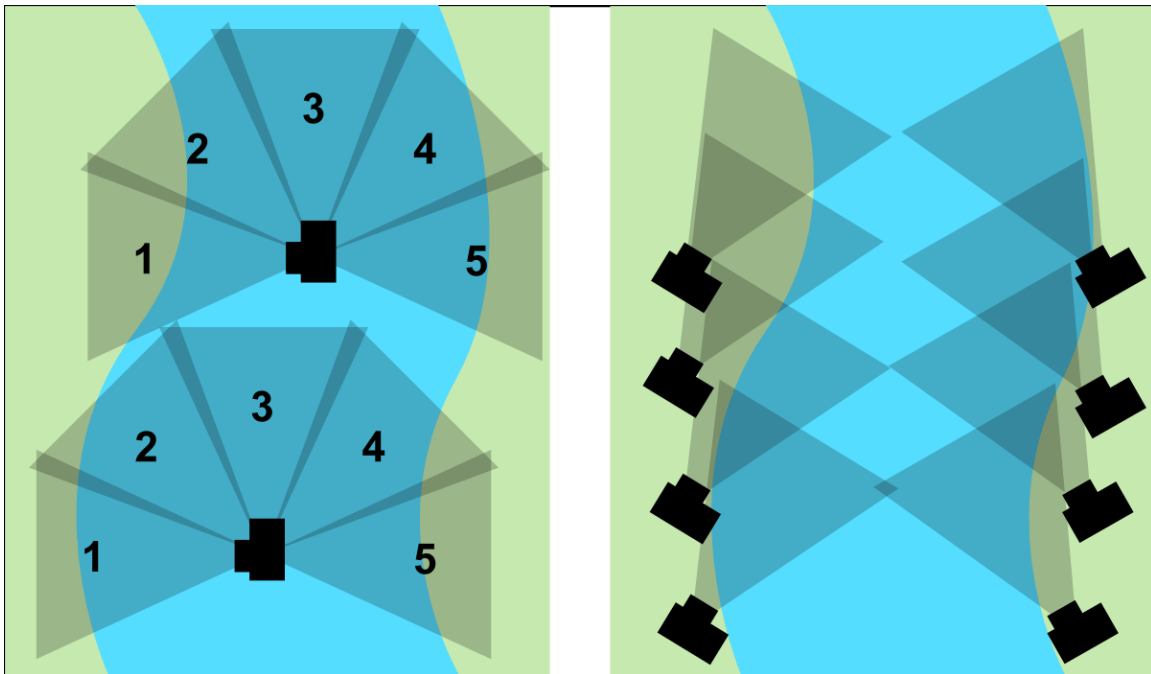


Figure 15: SfM survey patterns used in this study, divergent in stream survey for 2012 (left) and convergent bank survey for 2013 (right).

I processed the photo sets for each year using AgiSoft Photoscan Professional v. 1.0.4 (AgiSoft LLC, 2014) using the default settings for high-quality reconstructions and a pre-calibrated lens model to increase the accuracy of the reconstructions. I split the photosets into 16 overlapping chunks to facilitate processing; only those that coincided with the five GPS cross-sections will be presented in this study. I processed each chunk to a dense point cloud, to take advantage of recent developments in point cloud differencing algorithms, and produced a mosaicked orthophoto to aid in the interpretation of the cross-section and point cloud results. To quantify the change in the SfM point cloud, I used Lague et al.'s (2013) Multiscale Model to Model Cloud Comparison (M3C2) method implemented in CloudCompare v. 2.5.5.2 (Girardeau-Montaut, 2014). The M3C2 method provides a way to difference point cloud datasets in relation to the orientations of the various surfaces in the point cloud. By considering the orientation, M3C2 provides a three-dimensional way to assess change between two point clouds and evaluates significant change as a function of surface roughness in the immediate neighborhood of a point (local surface roughness) and a spatially uniform registration error between the two clouds.

The georeferencing accuracy statistics from Photoscan showed an average root mean squared error (RMSE) for the 2012 chunks as 1.21 cm and for 2013 as 1.24 cm. However, when I overlaid the point clouds prior to differencing there was an unexplained vertical offset between the 2012 and 2013 datasets. The individual chunks had uniform offsets between 2.7 and 3.4 cm. To correct this offset, I co-registered the two point clouds to each other using a range of four and six pseudo-invariant features, mainly large boulders embedded in the banks. The 2013 point clouds were transformed to match the

2012 data with an average co-registration RMSE of 1.03 cm. The co-registration error was factored into the total uncertainty for the SfM datasets for a minimum level of detection of 3 cm, slightly higher than the uncertainty values calculated in Chapter II. I included this minimum level of detection in the M3C2 results and they are included as part of the white area of the color ramp indicating no or insignificant change.

Results

Each of the five cross-sections showed varying amounts of change, but the majority of the changes were small magnitude, ± 10 cm (Figure 16). Because the cross-section points were not taken on the exact same lines and were transformed to a stream normal coordinate system, these direct comparisons have a considerable amount of uncertainty associated with them. Given the inherent measurement uncertainty of RTK-GPS and the horizontal and vertical shifts in the misaligned cross-sections, I approximated the minimum level of detection for these cross-sections to changes greater than 5 cm. This means any change less than 5 cm cannot be considered actual change and should be treated as insignificant. The largest negative elevation changes were on the right bank of XS 3 and the middle of XS 4. The in-channel portion of XS 1 showed an increase in bed elevation and XS 2 and XS 5 both had small lateral changes. For the cumulative change chart in Figure 16, 79% of the measurements do not meet the minimum level of detection, leaving only the largest changes considered measurable change.

The longitudinal profile comparison (Figure 17) shows that the riffles have experienced erosion while the pools have all seen deposition. The areas with more

significant erosion is located at 73 and 200 meters downstream and are associated with cross-stream wood pieces that have created small scour pools. The riffle between 120 – 130 meters downstream experienced approximately 20 cm of erosion, which would account for the higher than normal deposition in the pool immediately downstream. The planform position of the thalweg in Figure 17 remained consistent apart from a few large deviations. At 30 – 40 meters downstream, the thalweg shifted 3.5 meters toward the left bank. This location is the former confluence of Granite Boulder Creek with the north channel, and a portion of the dredge channel was kept intact as a backwater habitat site. The riffle upstream of this pool enters the pool on a wider fan of sediment; in 2012, the main flow over the fan was toward the right bank and in 2013, the flow had migrated across to the left bank side of the fan. These data are also subject to the same uncertainty and minimum level of detection as the cross-section data, but these data show more measurable change with only 13% of the length of the profile falling below the minimum level of detection.

The SfM results provide context for the cross sectional and longitudinal results as well as spatial information beyond the narrow focus of the GPS survey. Several problems arose in the processing of the SfM data, which can be corrected in future surveys, but they had an effect on the data quality and can be seen in the results. The photoset from 2012 contained too many photos, resulting in long processing times, and the divergent geometry caused errors during the alignment step in Photoscan. I was able to fix a majority of the alignment problems through a labor-intensive process aligning small groups of photos and merging these small groups to complete the reconstructions. From

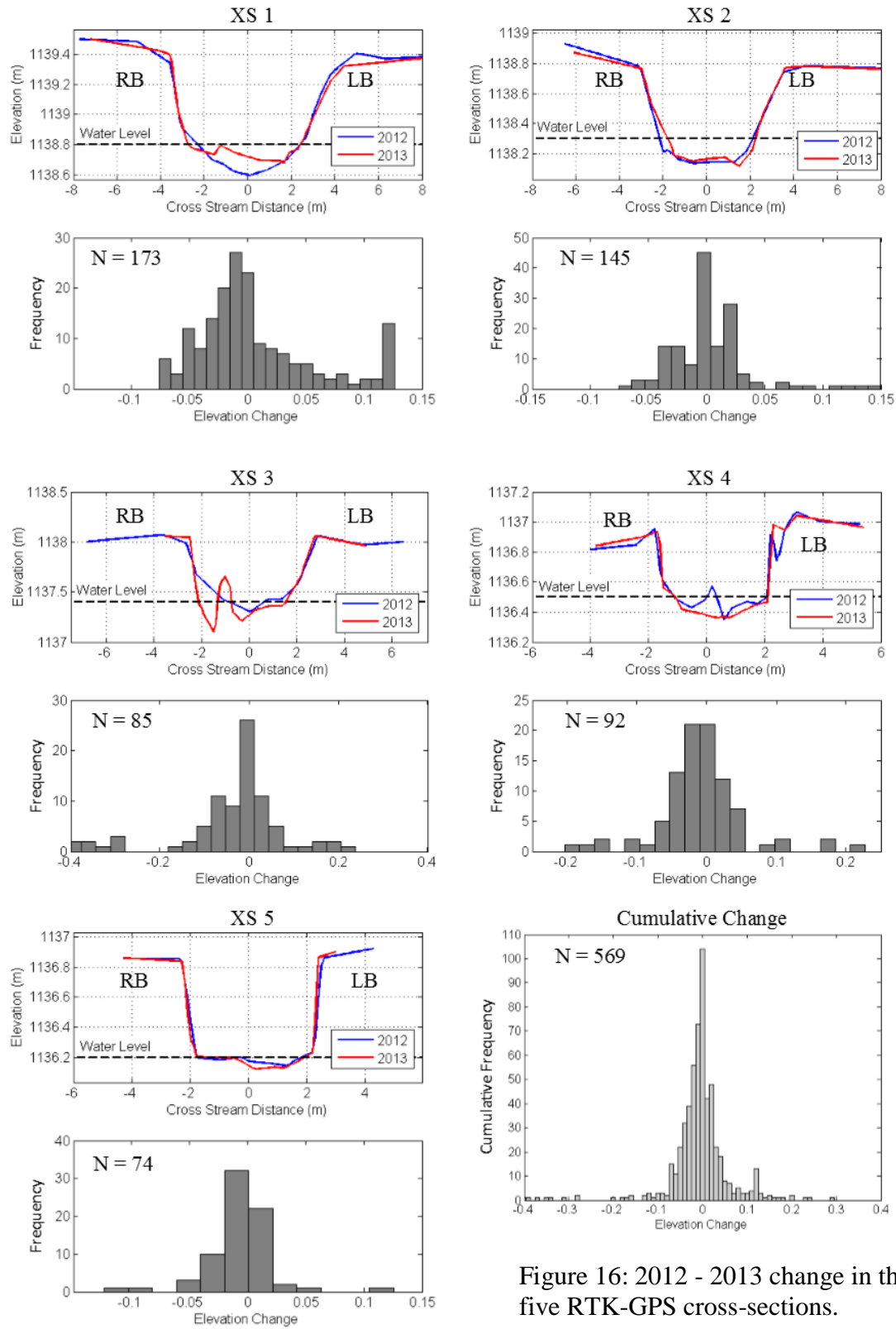


Figure 16: 2012 - 2013 change in the five RTK-GPS cross-sections.

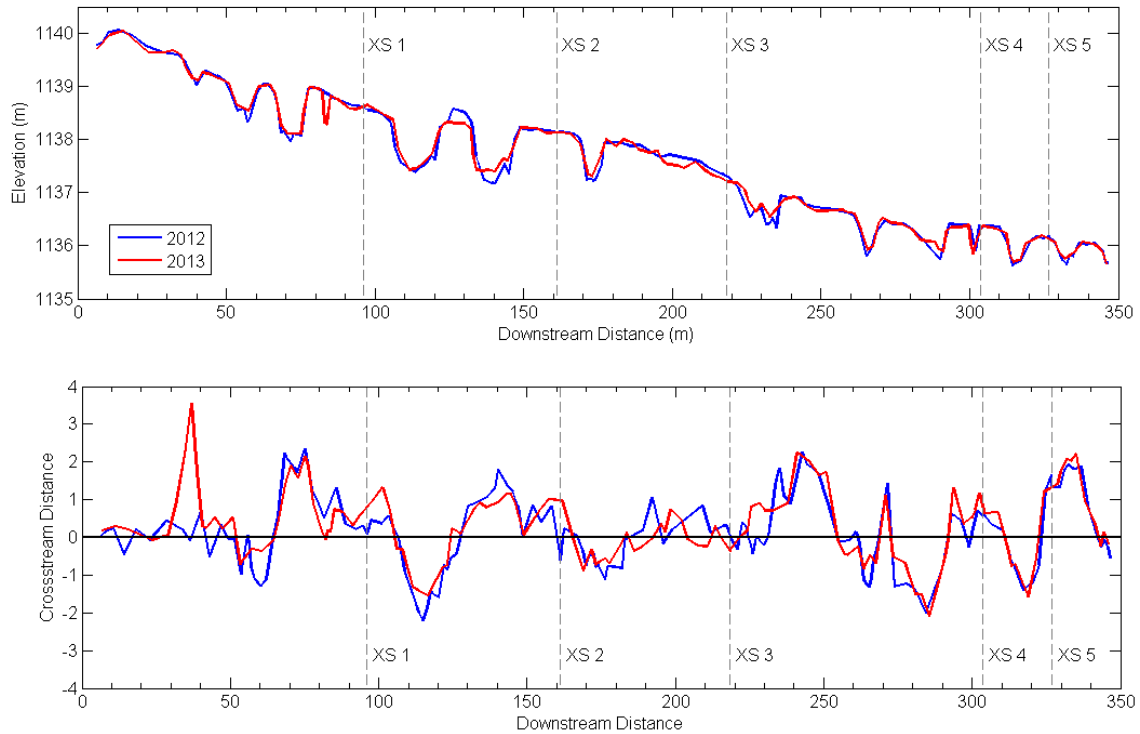


Figure 17: 2012 - 2013 change in the longitudinal profile elevations (top) and planform position of the thalweg (bottom).

the lessons learned in 2012, I took fewer photos and changed to a convergent geometry in 2013. The 2013 survey approach led to photos with insufficient overlap in many areas of the channel and led to inconsistent results in the final dense point clouds. In the reconstructions for both years, the moving surface of the water coupled with off-nadir viewing angles led to high errors in the point cloud in wetted portions of the channel. The high error in the wetted areas led to blank areas or noisy data that did not reflect the actual topography or bathymetry.

At all five cross-section the SfM results resemble the GPS results (Figure 18 and Figure 19), however, SfM orthophotos and M3C2 difference maps give a broader perspective beyond the narrow slice of the cross-sections. The erosion along the right bank below the middle channel-spanning log surrounding XS 1 (Figure 20) shows a similar pattern to the GPS cross-section data. The GPS data shows an aggraded bed,

which is confirmed by a small mid-channel bar that formed in between the middle and upper log structures and the widening of the channel in 2013. At XS 2 (Figure 21), the M3C2 difference map shows erosion on the left bank at XS 2 and upstream while there is a small amount of deposition on the right bank. Downstream of XS 2, the log structure appears to have trapped sediment on its upstream side and caused erosion on the downstream end. The in-channel logs upstream of XS 3 (Figure 22) have also caused some significant change to the downstream channel. The changes at the cross section reflect the shift from a narrow riffle in 2012 to a much wider channel, with the erosion along the right bank. The shift to the right bank gave rise to a bar on the left bank just downstream of the logs and a slight change in the thalweg. In between the two logs, there were changes caused when two *Carex nudata* (torrent sedge) tussocks planted in stream became dislodged. The stream washed away the downstream tussock and shifted the upstream one about 0.5 meters. The changes at XS 4 (Figure 23) were small; the in-channel changes in the profile appear to be from several cobbles exposed in 2012 and redistributed by 2013. The left bank of the GPS profile for XS 4 has the appearance of deposition high up on the bank. I plotted the sample points on the SfM data and found that this was the result of a sampling error on the log structure on that bank, caused because the 2012 data contained an extra point in between two of the logs. Unfortunately, where XS 5 crosses the stream the SfM difference data are incomplete, but in this section of the stream the high banks are made of cohesive clay soils and I was not expecting much change in this portion of the river. The other changes in the XS 4/XS 5 sections were changes in bar sediment at the left bank bar in the middle of the log structure and the right bank bar downstream of XS5.

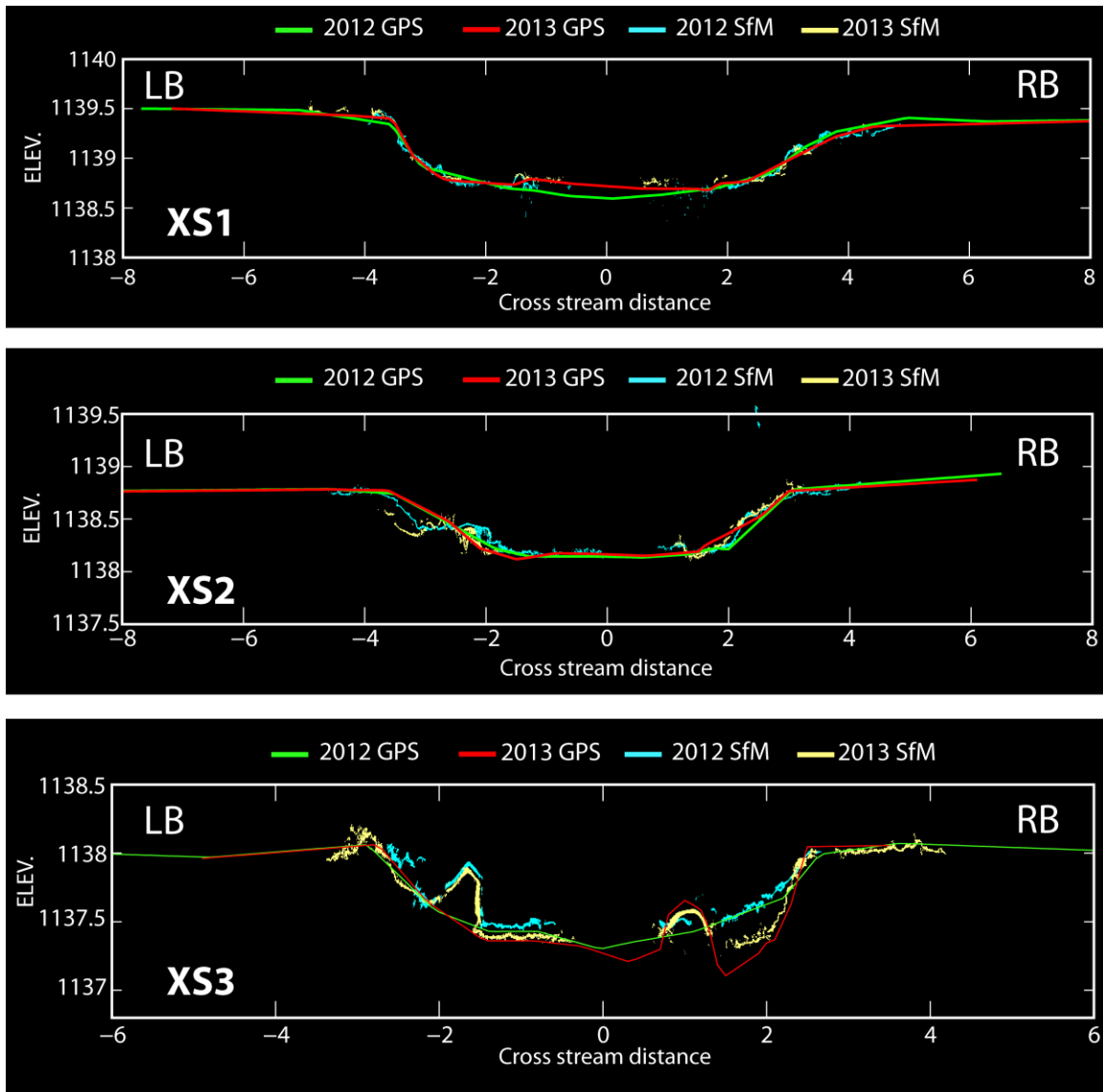


Figure 18: SfM - GPS cross section comparisons for XS 1, XS 2, and XS 3.

Discussion

One year after construction, the newly constructed channel for Granite Boulder Creek is already showing some signs of change. I did not expect any major changes in the channel because the winter snowpack was below average and there were no spring flood events. Most of change appears to be minor, focused in the surficial bed and bank sediments as the stream adjusts to its new channel. Beyond the geomorphic aspects of the stream, the SfM orthophotos provide important information on monitoring the riparian

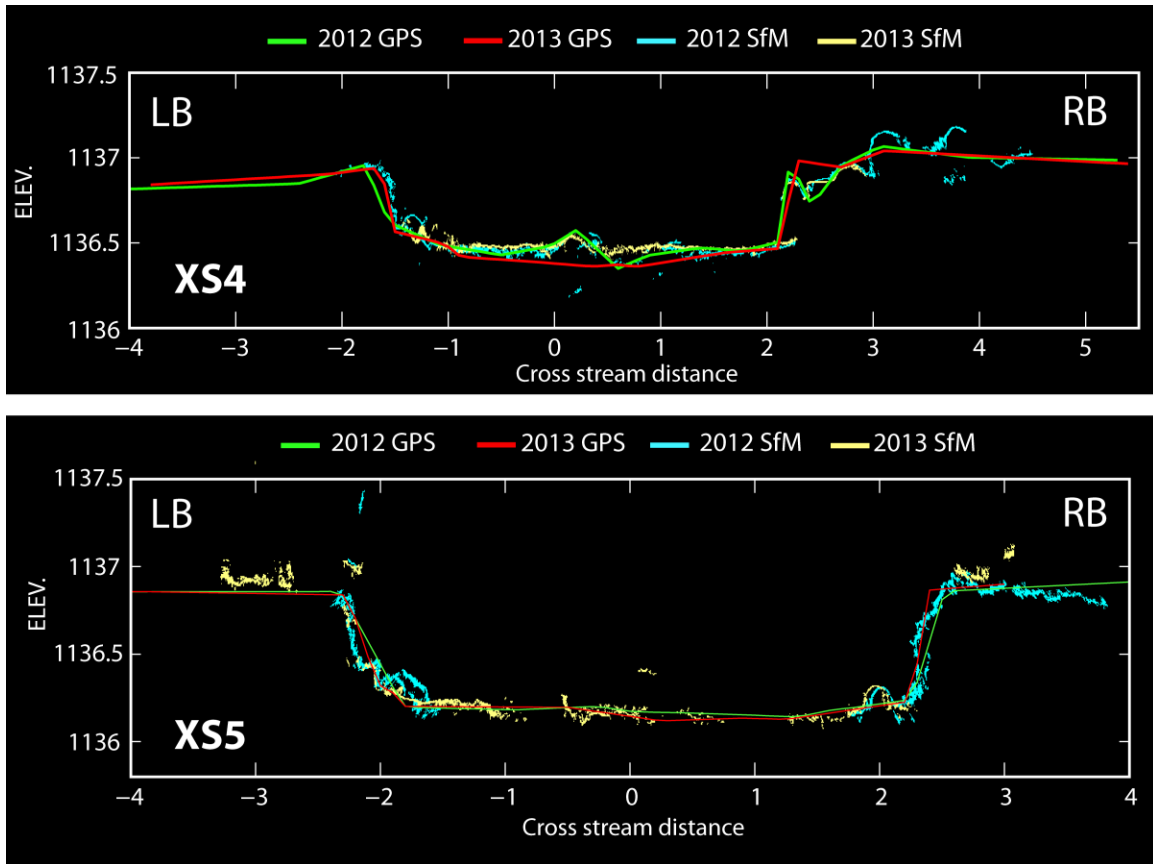


Figure 19: SfM - GPS cross section comparisons for XS 4 and XS 5.

vegetation planted as part of the channel construction. In the areas surrounding the cross-sections, the grasses and sedges along the channel were actively establishing while some of the woody plantings, mainly Alder shrubs, were less successful.

The repeat GPS cross-sections and longitudinal profiles provided a narrow, simplified view of the stream and were an easy way to visualize change. However, without context, the results were difficult to interpret and the high uncertainty diminished the value of the data. By fusing the GPS data with the SfM photosets, I could provide that context and create a map of change beyond the thin slice of the cross section. This broader perspective on channel change not only provides site-specific erosion and deposition volumes, but also provides a three-dimensional perspective on channel

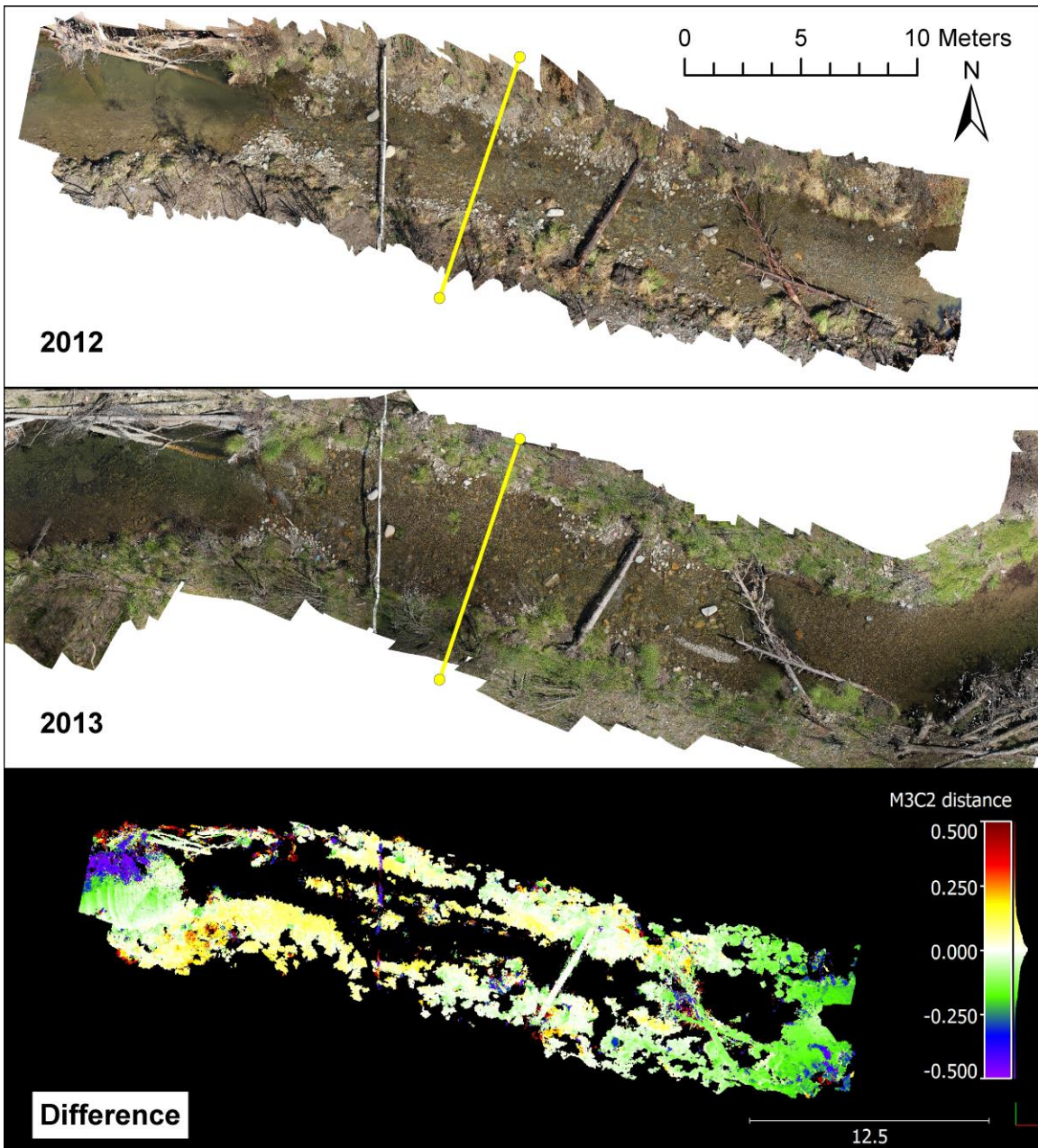


Figure 20: SfM M3C2 difference results for XS 1 with orthophotos for reference. Flow is right to left.

hydraulics in newly constructed stream channels. A clear example of this is in the SfM data surrounding XS 3 (Figure 22), where the riffle section was constructed as a straight conduit between two pools. The effect of the cross-stream wood structure is visible in the 2013 data. By diverting flow toward the right bank, the wood structure has induced erosion along the right bank and promoted bar deposition on the left bank.

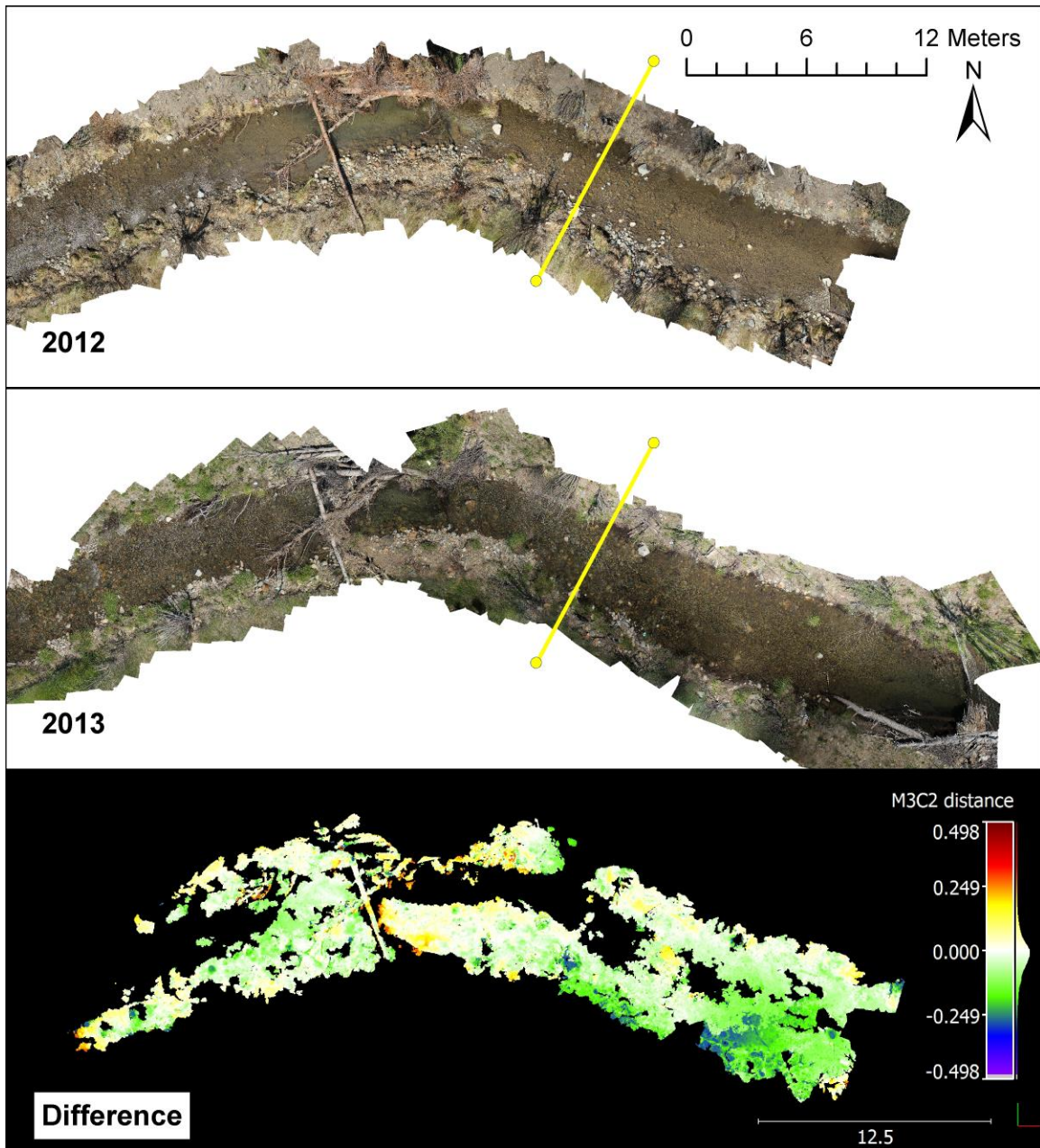


Figure 21: SfM M3C2 difference results for XS 2 with orthophotos for reference. Flow is right to left.

Despite the problems with the SfM surveys, the method still has a lot of promise as a low-cost option for three-dimensional geomorphic monitoring of small streams like Granite Boulder Creek. With several refinements to the survey methodology, from the lessons learned in this study and potential additions from other research, it is possible to

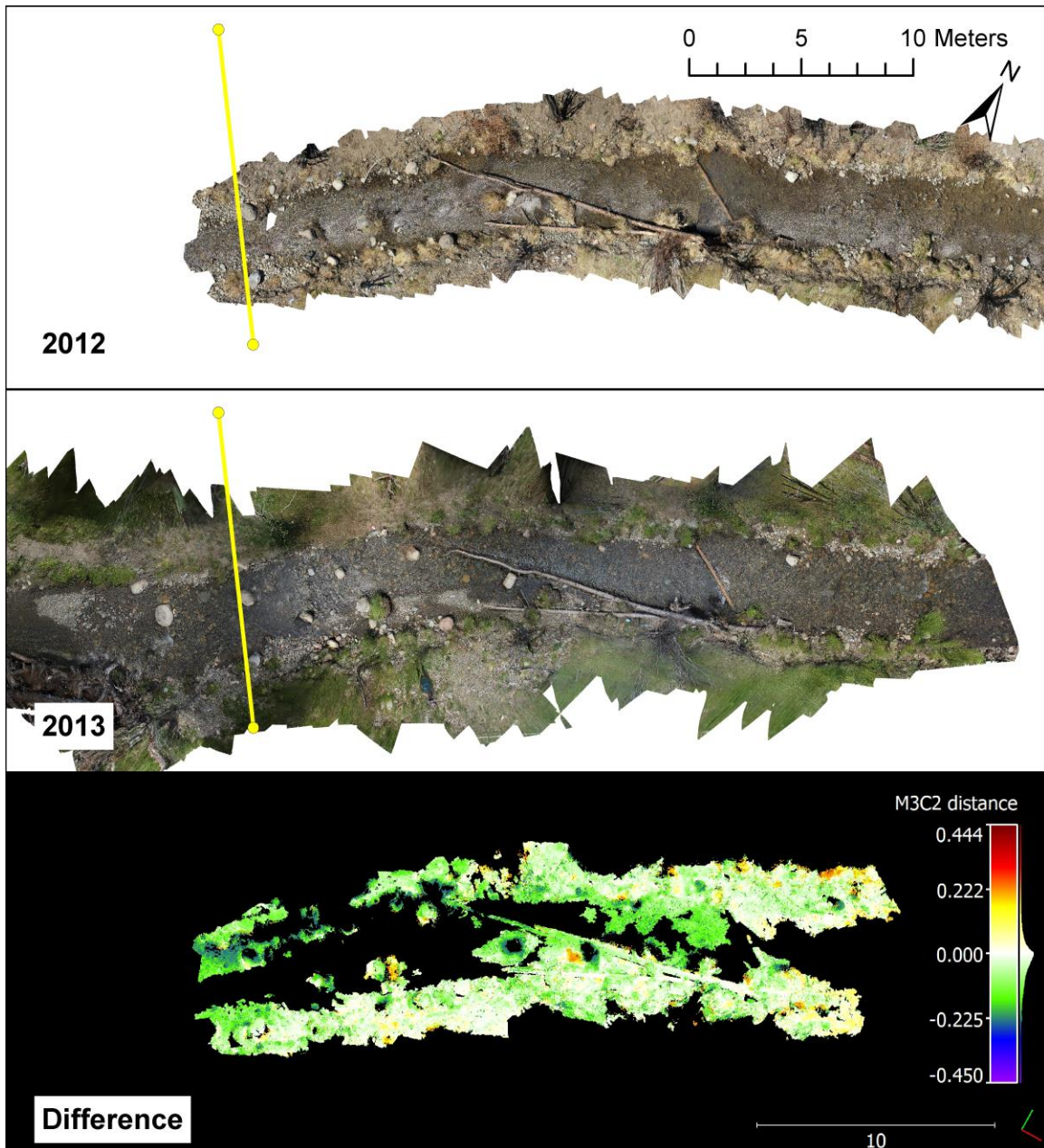


Figure 22: SfM M3C2 difference results for XS 3 with orthophotos for reference. Flow is right to left.

improve the quality and accuracy of the results. The first improvement would be in the ground control used to georeference the SfM reconstructions; the seven-meter spacing of the targets in this study was too far apart to make smaller sections for more efficient processing. The distance between targets also meant that they were all needed for calibration and none could be held back for validation purposes. My use of temporary

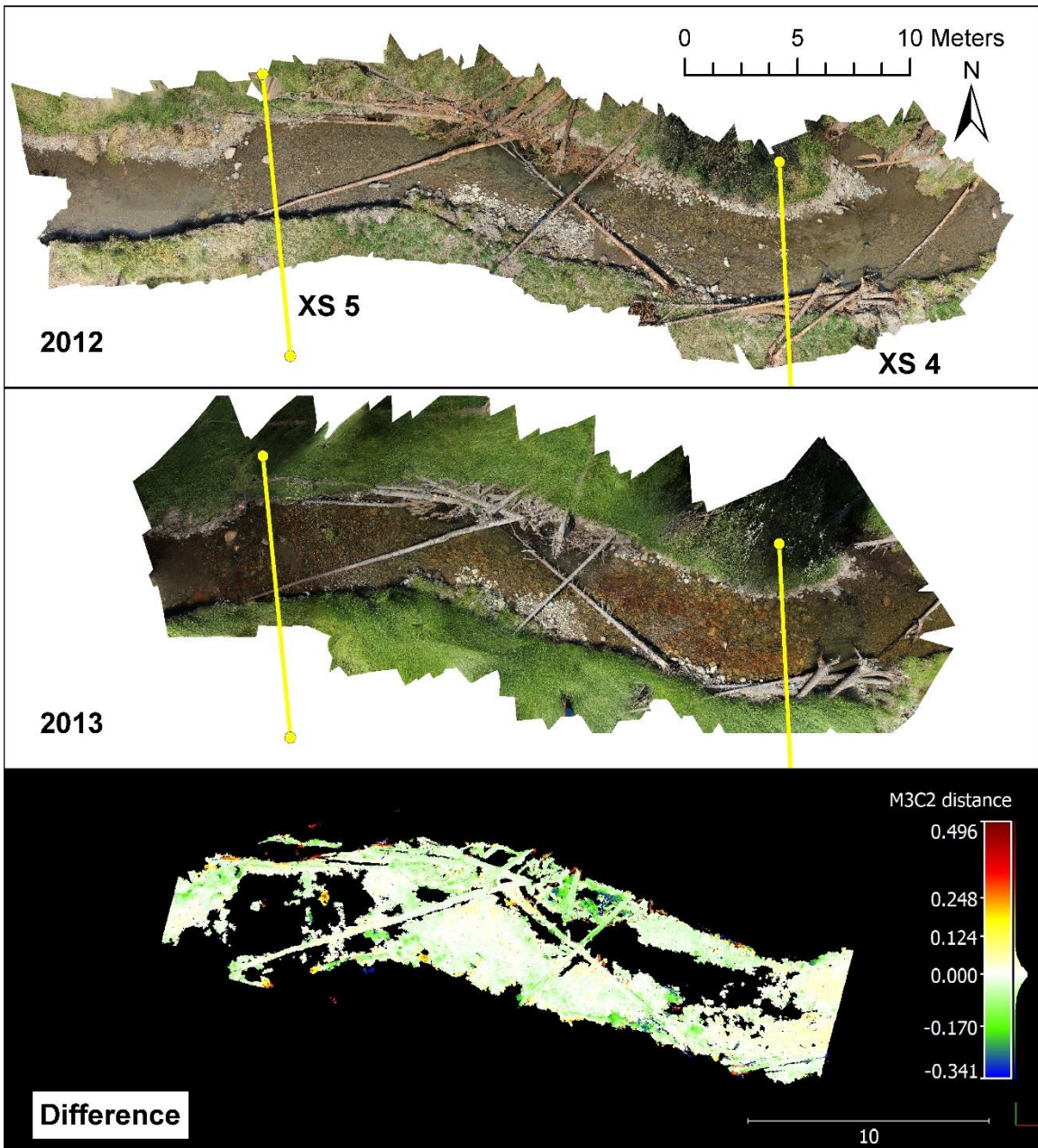


Figure 23: SfM M3C2 difference results for XS 4 and XS 5 with orthophotos for reference. Flow is right to left.

targets improves flexibility in their placement, but they do not provide any common reference points used to gauge error between the temporal datasets. In future monitoring studies, I would recommend monumenting several permanent ground control locations on the banks of the channel and supplementing these permanent ground control points with additional temporary targets with spacing of two meters or less.

The second improvement is change to the SfM survey pattern. Every SfM survey location is going to have its peculiarities that will require special considerations to achieve the best coverage. The two most important aspects in any SfM survey are large overlaps between photos and convergent camera geometry (Fonstad et al., 2013; James and Robson, 2014; Westoby et al., 2012). The platform for photography is an important consideration that will determine the survey pattern. Hand-held or pole photography are the lowest cost options for collecting imagery; hand-held is the most efficient option for small areas ($10^0 - 10^2 \text{ m}^2$) and can be done quickly, while pole photography, with its increased field of view, helps speed up surveys of larger areas. Another option for SfM surveys are low altitude aerial platforms like tethered balloons or unmanned aerial vehicles/systems (UAV or UAS, fixed-wing or rotorcraft). These platforms afford an even larger field of view, but the cost and training requirements can put these platforms out of the reach for many researchers. For small streams, I would recommend the pole photography platform and a photography pattern that includes both bank and in stream photo locations to ensure the broadest possible coverage.

Being able to extract water depths and stream bathymetry would also increase the usefulness of SfM surveys. Unfortunately, the multi-view nature of SfM and the characteristics of water restrict SfM's ability to measure accurately the bathymetry. The movement, aeration, suspended sediment, and bidirectional reflectance of water all change in between photographs, making it difficult for the algorithms to find matching features in multiple photographs. This leads the software to reject most in-water points because they do not meet the threshold for accuracy to be included in the final model. Some successful research has been done in this area by Woodget et al. (2014) using nadir

photography from a UAV, but more research and validation needs to be done for other platforms and fluvial environments. At present, the most efficient option to capture both topography and bathymetry is the combined use of SfM for the above water portions and GPS/total station surveys for underwater portions.

Conclusions

In this research, I have demonstrated that SfM has potential to be a low-cost tool for stream restoration monitoring. The high spatial resolution of SfM is able to provide data on the small scale changes that occur in the short-term and the spatially continuous perspective is able to capture the variability in the system. However, because of the youth of the method more research is needed on the optimal number and spacing of ground control points, the best survey patterns and platforms, and the possibility of extracting bathymetry from the images and point clouds. With these improvements, SfM paired with GPS surveys will be an efficient way to collect high-resolution three-dimensional datasets for stream restoration projects, providing a broader perspective on change.

Granite Boulder Creek has shown some minor channel and vegetation changes in the first year since its restoration. The changes are visible throughout the new channel and relate to surficial changes in bed and bank sediments. These first year data are an important baseline for future monitoring and management activities in this part of the Middle Fork. In the future, joining these data with other geomorphic and ecologic monitoring data collected in the larger restoration project of the dredge mined portion of the Middle Fork will provide a comprehensive view of the progress toward the restoration project goals.

CHAPTER IV
SUB-METER REMOTE SENSING FOR RIVERSCAPE MAPPING WITH
HELICOPTER-BASED STRUCTURE-FROM-MOTION PHOTOGRAMMETRY

Introduction

Remote sensing has proven to be an invaluable tool for river research giving researchers the opportunity to collect spatially continuous datasets of key river morphologic variables (i.e. width, depth, bed sediment size) at high spatial resolutions over entire river basins (Carbonneau et al., 2012; Fonstad and Marcus, 2010). Some studies have focused on continental scale mapping with satellite imagery (Yamazaki et al., 2014) and others have used aerial photography to map grain size distributions (Dugdale et al., 2010). These measured morphologic variables, along with other derived hydraulic variables, can be used to produce detailed spatially continuous maps of the physical structure of rivers that can be used to study both geomorphology and lotic habitats, creating a holistic view of the riverscape (Carbonneau et al., 2012; Fausch et al., 2002). Collecting imagery and elevation data for this type of mapping can be an expensive endeavor, especially over large areas. New developments in computer vision-based Structure-from-Motion multi-view stereo photogrammetry (SfM or SfM-MVS) have made the collection of high-quality elevation data and accurate orthophotographs easily obtainable for anyone with a high-quality GPS and a modest digital camera (Fonstad et al., 2013; James and Robson, 2012; Javernick et al., 2014).

The Middle Fork John Day River (hereafter the Middle Fork) has been designated as critical habitat in the Columbia River system for Chinook salmon (*Oncorhynchus*

tshawytscha), steelhead (*Oncorhynchus mykiss*), and bull trout (*Salvelinus confluentus*) (NOAA, 2005; U.S. Fish & Wildlife Service, 2010). However, humans have affected this critical habitat in the Middle Fork over the past 200 years with channel modifications, cattle grazing, and placer mining. Over the last 20 years, conservation-minded landowners have purchased large portions of land in the upper portion of the basin and have begun to rehabilitate and restore the river in order to improve instream habitat.

The goals of this study were twofold. The first objective was to collect aerial photography with a helicopter-mounted digital SLR camera and process it with SfM to create high-resolution orthophotographs and digital elevation models (DEMs) for a 32-km segment of the Middle Fork John Day River. The second goal of the study was to extract spatially continuous datasets of river morphology from the SfM data and examine the current downstream patterns in channel morphology, specifically how they relate to the imprint of human modification and the effects of those modifications on Chinook salmon habitat.

Background

Traditional sampling in rivers has either been done intensively over small areas or extensively over large areas with widely spaced measurements. Both of these methods have the potential to undersample river environments and miss critical elements of the river (Marcus and Fonstad, 2010). By employing remote sensing, researchers are able to collect spatially extensive measurements of both primary physical variables (e.g. width, depth, slope, and sediment sizes) and secondary hydraulic variables such as velocity and stream power (Carbonneau et al., 2012; Carbonneau, 2005; Dugdale et al., 2010; Fonstad and Marcus, 2010; Walther et al., 2011). In this study, I will focus on the primary

physical variables, specifically the bankfull or active channel width. Bankfull channel width is a fundamental variable to describe stream morphology (Andrews, 1982; Faustini et al., 2009). Width is an important variable in hydrology and geomorphology because it is the basis for determining discharge using the continuity equation (discharge = width × depth × velocity) (Leopold and Maddock, 1953). Width is also one of the major degrees of freedom that streams can adjust in response to natural fluctuations in discharge and disturbances (Hey and Thorne, 1986; Knighton, 1998; Pizzuto, 2008; Whittaker et al., 2007). Because width is the most accessible variable in remotely sensed imagery (Pavelsky and Smith, 2008), I will be using width as the primary indicator for channel morphology.

Theoretically, the only limiting factor for the scale of these measurements is the spatial resolution of the imagery. The measurements can be aggregated to provide spatially averaged data at any spatial scale. These multi-scale data are helping challenge classic conceptual models of rivers such as downstream hydraulic geometry (Leopold and Maddock, 1953) or the river continuum concept (Vannote et al., 1980), which view rivers as smooth downstream trends in morphology and energy. These models are being replaced with conceptualizations that embrace the heterogeneity of the river as key to understanding both geomorphic and ecologic patterns (Carbonneau et al., 2012; Fausch et al., 2002; Fonstad and Marcus, 2010; Frissell et al., 1986; Montgomery and Buffington, 1998; Poole, 2002; Ward and Stanford, 1995).

The Middle Fork, like many montane rivers, is also complicated by the mixed alluvial and bedrock channel substrates that can interrupt any downstream trends and lead to changes in channel morphology that are independent of larger variables like drainage

area (McDowell, 2001). The main human influences in the Middle Fork valley have been cattle grazing in the floodplain and riparian zones, channel modification to accommodate grazing, water diversion for irrigation, and placer mining in the channel. Grazing along the Middle Fork has resulted in a reduction of riparian vegetation and in some areas bank erosion caused by trampling, which is consistent with previous studies on the impact of grazing on river channels (Magilligan and McDowell, 1997; Marston et al., 1995; Trimble and Mendel, 1995). Channel modification reduces meandering and habitat diversity while increasing velocities and altering sediment transport (Korpak, 2007). Irrigation diversions affect instream flows, which have a negative effect on sediment transport and aquatic habitat (Angelaki and Harbor, 1995; Richards and Wood, 1977; Ryan, 1997). Placer mining causes a complete reconfiguration of the valley and channel, which affects the entire local river system, but also alters the sediment and water supply to downstream reaches (Graf, 2000; Kondolf, 1994, 1997; Kondolf and Larson, 1995).

While photogrammetry is not a new tool in the remote sensing of rivers toolkit (Lane et al., 1994, 2003), the recent introduction of SfM photogrammetry has given researchers new opportunities to collect aerial imagery and create highly detailed digital elevation models at far lower costs than traditional aerial photo collection methods. SfM has already proven to be useful in rivers at a variety of spatial scales from smaller areas of tens and hundreds of meters (Fonstad et al., 2013; Woodget et al., 2014) to kilometers (Javernick et al., 2014). The original algorithms for SfM were developed in the field of computer vision in the 1970s (Ullman, 1979) and the newest iterations were synthesized in the late 2000s (Agarwal et al., 2009; Snavely et al., 2007). SfM provides an alternative to traditional photogrammetry because it can be done with an off the shelf digital camera

and there are fewer requirements for the number of ground control points needed for the final reconstruction (Fonstad et al., 2013; James and Robson, 2012; Javernick et al., 2014; Westoby et al., 2012). SfM is able to do this by using multiple camera views to increase the accuracy of photogrammetrically derived three-dimensional points that result in a dense three-dimensional point cloud dataset, not unlike an aerial or terrestrial LiDAR dataset. By converting the point clouds into TIN or raster digital elevation models (DEMs), the input photographs can then be mosaicked and orthorectified to the DEM.

Study Area

I performed this research on the Middle Fork of the John Day River, in eastern Oregon, USA. The segment of interest is in the upper portion of the basin and covers 32 river kilometers from Bates State Park downstream to 700 m below the USGS stream gauge above the confluence with Camp Creek (Figure 24). The Middle Fork is one of three main branches of the John Day River, which drains to the Columbia River. To aid in the analysis and discussion, I divided the river into eleven segments based on land use and valley width. Major tributary junctions act as boundaries, appearing in Figure 24, with specific details for each segment outlined in Table 7 and Table 8.

Euro-American settlement in the area started in the mid-1800s. The Middle Fork watershed has been subject to a range of human impacts in that time. Beginning in the late 1800s, cattle ranchers used the valleys as summer pasture. The primary effects of ranching have been a reduction in riparian vegetation, channel straightening, water diversion for irrigation, and bank trampling by cattle. Logging led to the establishment of a mill at the upper end of the study area, at Bates State Park, and the extension of a railroad spur down the valley. One of the most dramatic impacts on the river was placer

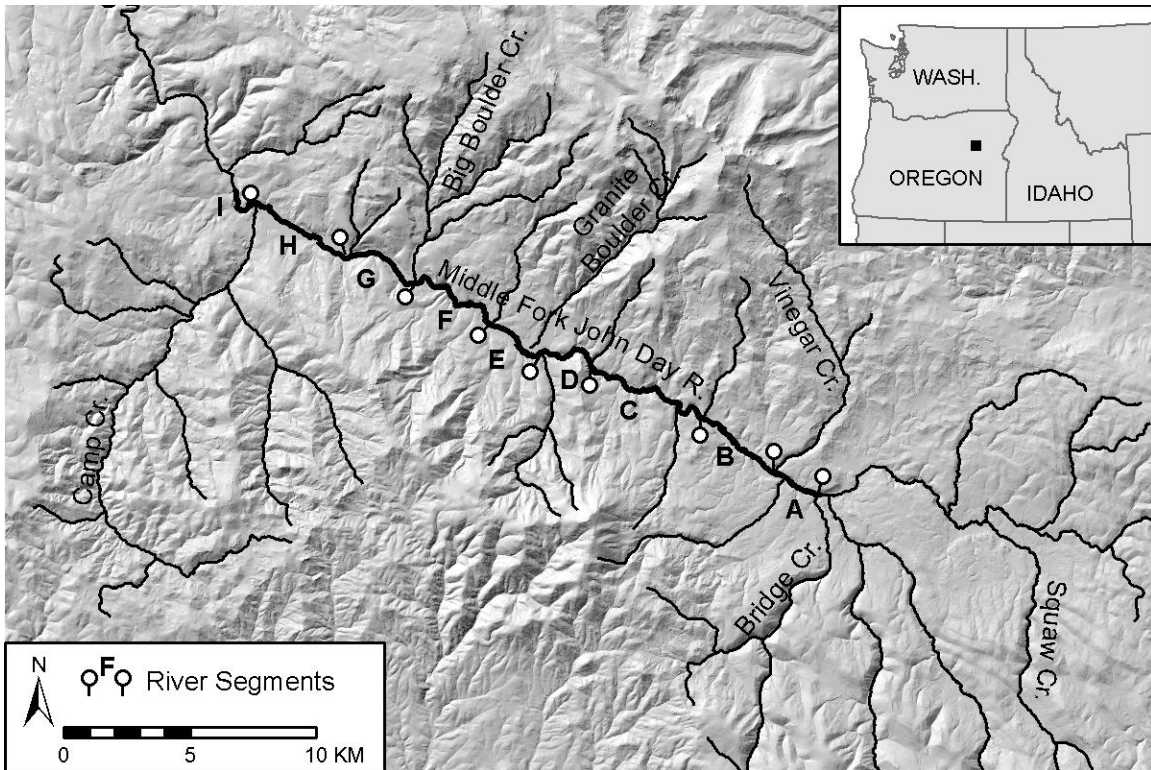


Figure 24: Map of the upper Middle Fork John Day River, with study area highlighted by the labeled river segments.

gold mining operations that used dredges to overturn the valley floor sediment for gold extraction. Mining in the basin has been ongoing since the 1860's, but the primary dredging operations operated in the late 1930's – 1940's along the middle of the study area, section E, around Granite Boulder Creek.

The Middle Fork is home to populations of anadromous fish, Chinook (*Oncorhynchus tshawytscha*) and steelhead (*Oncorhynchus mykiss*). Steelhead along with bull trout (*Salvelinus confluentus*) are listed as threatened under the Endangered Species Act, while Chinook in the Middle Fork are listed as a species of concern. The Middle Fork, and the entire John Day River system, has been critical habitat for the anadromous species because there are no barriers to fish passage after the three lower dams on the Columbia River. The critical habitat designation has led a significant effort to rehabilitate and restore the Middle Fork to improve fish habitat for all life stages. The restoration

activities have included riparian plantings to improve shading of the river, the installation of large wood structures to increase habitat in pools, and channel construction to reverse the effects of channel straightening and dredge mining.

The geology of the area is volcanic bedrock, including Miocene basaltic-andesites of the Strawberry Volcanics at the higher elevations and mixed Eocene basaltic flows, tuffs, and conglomerates of the Clarno Formation at the lower elevations (Ferns and Brooks, 1995; Jett, 1998). The hillslope vegetation is predominantly Ponderosa pine forest, while grass meadows cover the valley floodplains. The riparian vegetation consists of mainly grasses and sedges with sparse woody vegetation. Throughout the study area, there are clumps of in-channel vegetation that primarily are *Carex nudata*, or torrent sedge, that can form significant obstacles to flow, especially at lower flows. The hydrology of the Middle Fork mirrors many rivers of the Mountain West of the USA with peak flows coinciding with spring snowmelt in late April to early May and low flows corresponding to the dryer summer months, August and September. At the USGS gauge above Camp Creek, peak flows average 30 cms and low flows average 0.5 cms.

Data and Methods

Aerial Photography Collection

I collected aerial photography for this research on August 13, 2013 using a Canon T5i digital SLR flown on a Robinson R44 Raven helicopter (Figure 25). The camera was mounted in a nadir position within the helicopter's cargo box using a vibration isolation mount to reduce the effect of aircraft vibration on image quality. A Garmin GPSMAP60 CSx handheld GNSS receiver recorded the camera's approximate location during the

Table 7: River segment details. Segments are mapped in Figure 24.

Segment	Length (km)	Drainage Area at Downstream Boundary (km ²)	Downstream Boundary	Valley Type	Channel Type
A	2.44	345	Vinegar Cr.	Intermediate	Riffle/Pool
B	4.50	404	Caribou Cr.	Wide	Riffle/Pool
C	7.19	462	Tin Cup Cr.	Narrow	Mixed – Riffle Pool, Plane bed
D	1.78	467	Butte Cr.	Wide	Riffle/Pool
E	3.01	538	Beaver Cr.	Wide	Riffle/Pool
F	4.79	579	Big Boulder Cr.	Wide to Narrow	Mixed – Riffle Pool, Plane bed
G	3.31	640	Coyote Cr	Mixed	Riffle/Pool
H	4.90	667	Camp Cr.	Wide	Riffle/Pool
I	0.38	829	-	Narrow	Plane bed

Table 8: River segment detail, continued. Human modification codes: CS = channel straightening, DM = dredge mining, G = grazing. Restoration activity codes: RP = riparian planting, LW = large wood placement, CM = channel modification. Segments are mapped in Figure 24.

Segment	Present Land Ownership	Current Land Use	Human Modifications	Restoration Activity
A	State Park	Recreation	CS	None
B	Private	Conservation	CS, RRG	Minor – RP, LW,
C	Nat. Forest	Recreation / Limited grazing	None	None
D	Private	Conservation	None	Minor – LW
E	Private	Conservation	CS, DM	Major – LW, RP
F	Private / Nat. Forest	Conservation / Limited Grazing		Minor – RP, LW
G	Private	Conservation	CS	Minor - LW
H	Private	Conservation / Intense Grazing	CS, G	Minor – RP, LW
I	Nat. Forest	Grazing	None	None

flight. The use of the Garmin was strictly to speed up the processing of the images in was strictly to speed up the processing of the images in Photoscan. By geotagging each photo with an approximate X, Y, and Z location the software can limit its search for nearby

camera locations, reducing the time needed for the image alignment stage of the SfM processing.

The spatial resolution of the imagery and image overlap are two key variables in any SfM survey. Higher spatial resolutions allow for higher point cloud precision and because SfM is a multi-view photogrammetric process, a minimum of 60% overlap in the imagery is needed to guarantee at least four different perspectives of any area in the imagery (Fonstad et al., 2013; James and Robson, 2012). For this study, I planned for a ground resolution of 5 cm; to achieve this the helicopter flew at an altitude of 200 m above ground level (AGL). To acquire the required 60% forwardlap in the images, the helicopter flew at 25 knots (12.8 ms^{-1}) and an intervalometer triggered the camera shutter to capture images at four-second intervals. For narrow valley sections, the flight plan



Figure 25: Helicopter aerial photography setup. Canon T5i in the vibration-isolating mount with GPS and intervalometer (upper left). Robinson R44 helicopter at takeoff (upper right). Examples of ground control targets, 1-meter tarps (lower left) and roadside painted targets (lower right).

consisted of a single line of photographs that followed the river, while the wider valley sections used flight lines that covered the ground area with 60% sidelap. The flight time was approximately 2.5 hours at a total cost of \$1,300 USD.

A series of 66 ground control targets were laid out throughout the study area, which were used as ground control for the imagery. The points were marked with marking paint on roadsides (18 points) or with 2-meter blue tarp targets (48 points) (Figure 25). I recorded the coordinates for each point using a Trimble GeoXH GNSS receiver with an external antenna. I performed a differential correction on all of the points to achieve decimeter (<20cm) average error. This portion of the Middle Fork valley does not have a suitable network of previously surveyed benchmarks or control points, severely limiting the use of an RTK GNSS system. Performing the necessary static occupations to establish a network of accurate control points for an RTK survey was outside the scope of this research.

I processed the photos with Agisoft Photoscan Professional (Version 1.4). The processing steps included the initial sparse reconstruction, applying ground control to the sparse reconstruction, optimizing the photo locations/sparse reconstruction, dense reconstruction, TIN surfacing, DEM, and orthophotograph generation. The flight produced 1,483 photographs. By grouping the photos into sets of 200 to 400 photos, it was possible to facilitate processing within the memory limitations of the computer. The image groups roughly corresponded to changes in the valley morphology.

Because SfM is an emerging technique, it is important to assess both the horizontal and vertical accuracy, as well as the uncertainty in the resulting DEMs and orthophotographs. By using the adjusted root mean square error, it was possible to

measure the horizontal accuracy, while calculating horizontal uncertainty by the standard deviation of the error distribution of the control points versus their location in the SfM reconstructions. Measuring vertical accuracy and uncertainty in relation to a 2008 LiDAR dataset, which produced a spatially extensive accuracy assessment, enabled the use of all the ground control points for calibration.

Riverscape Data Extraction and Analysis

By using both manual and automated GIS methods on the SfM orthophotographs, SfM DEMs, and a 2008 LiDAR survey, it was possible to extract river data. Hand digitizing of the SfM orthophotographs produced the major geomorphic units of the river, which include the wetted channel, active channel (an approximation of bankfull), bars, islands, and in-channel vegetation. The basis for the downstream measurements were the active channel's geometric centerline, which was extracted by using a skeletonization algorithm applied to the active channel boundary (Hauert and Sester, 2008). A Savitzky-Golay filter (Legleiter and Kyriakidis, 2006) was applied to the centerline to smooth the line and remove angular joints that did not accurately follow the natural curvature of the channel. By using an automated routine to plot perpendicular cross-sections at 3-meter intervals along the centerline, it was possible to extract cross-sectional information, with any overlapping cross-section lines edited to create a continuous dataset of spatially unique samples. Intersecting these cross-sections with the digitized channel polygons produced cross-sectional width data. This permitted the conversion of the cross-section lines to point features at the intersection of the cross-section and the centerline. The point features created a master dataset at 3-meter increments used for later downstream comparisons.

Valley cross-sections were created at 100 meters intervals along the centerline to avoid them crossing each other. To calculate width, I intersected the larger cross-sections with the valley floor and floodplain polygons. Interpolating the resulting widths allowed me to add valley width measurements to each downstream sample point. The drainage area for each downstream sample point was calculated using a flow accumulation algorithm and the 1/3 arc second National Elevation Dataset for the Middle Fork John Day Basin. The 2008 LiDAR raster datasets provided the elevations for each point. Several categorical variables were manually added to the sample points using the SfM orthophotographs as reference: channel units (riffle/pool/glide), land ownership, grazing intensity, presence of restoration activity, affected by dredge mining, and underlying geology. The minimum mapping unit for these variables was one sample point, or approximately 6 meters. I classified channel units visually, guided by my field observations of the different channel segments. Areas of consistent white water were classified as riffles, calm water was classified as pools, and areas of intermittent white water were classified as glides.

By using this initial variable set, additional derived variables were then calculated. Accurate downstream distances were obtained by transforming the XY coordinates of the sample points to a stream normal coordinate system (Legleiter and Kyriakidis, 2006). Channel slopes were calculated using the LiDAR elevations and a custom moving window mean filter removed areas in the LiDAR data that resulted in negative (uphill) slopes. Discharge at all points was estimated using regional low-flow regression equations for the annual fifth percentile (Eq. 3) (Risley et al., 2008).

$$Q_{P5} = 1.05437 \cdot 10^{-2.4832} \cdot DA^{0.9304} \cdot P^{2.1271} \quad (3)$$

Where DA is the drainage area (sq. miles) at each sample point, P is the basin averaged mean annual precipitation (inches), SP is the soil permeability (in/hour), XS is the maximum slope in the basin, and F is the percent forest cover in the basin. All of the variables except drainage area were taken from the USGS StreamStats program (U.S. Geological Survey, 2012). While these regional regression equations provide estimates of discharge, at low flows the basin-averaged variables provide a smoothly varying discharge that may not account for gains or losses in discharge from hyporheic flow that may not be suitable for this type of site specific study. (Risley et al., 2008).

Extracting stream depth from the spectral information in the SfM orthophotographs (Carbonneau et al., 2012; Fonstad and Marcus, 2010; Legleiter and Fonstad, 2012) was one of the goals of this project. Unfortunately, the radiometric resolution, water turbidity, and image exposure were not conducive to using spectral depth techniques. In place of actual depths, average depths were estimated using an inverted form of Manning's equation, substituting Manning's n with Jarret's n (Jarrett, 1984; Marcus et al., 1992) and replacing the hydraulic radius with average depth:

$$Q = A \cdot v \quad (4)$$

$$\text{where } A = w \cdot d, v = \frac{d^{2/3} \cdot S^{1/2}}{n}, n = 0.32 \cdot S^{0.38} \cdot d^{-0.16} \quad (5)$$

$$Q = \frac{w \cdot d \cdot d^{2/3} \cdot S^{1/2}}{0.32 \cdot S^{0.38} \cdot d^{-0.16}} \quad (6)$$

$$Q = \frac{25 \cdot S^{3/25} \cdot d^{137/75} \cdot w}{8} \quad (7)$$

$$d = \left(\frac{8 \cdot Q}{25 \cdot S^{3/25} \cdot w} \right)^{75/137} \quad (8)$$

In Eq. 4-8, Q is discharge (cms), A is the cross-sectional area of the channel (m²), v is the average velocity (m/s), w is the cross-section width (m), d is the average depth (m), n is roughness (Jarret's n in this case), and S is the channel slope. Average depths for the each sample point were calculated for both the annual fifth percentile (P5) discharge from the regional regression equations (Eq. 3).

Pairing depth and discharge with the other variables, I was able to calculate a number of additional hydraulic equations, assuming steady state flow, to get estimates of velocity (v, m/s) (Eq. 9), unit stream power (Ω , W/m²) (Eq. 10), Froude number (F) (Eq. 11), and shear stress (τ , kg/m·s²) (Eq. 12) with the following equations:

$$v = \frac{Q}{A} \quad (9)$$

$$\Omega = \frac{\rho g S Q}{w} \quad (10)$$

$$F = \frac{v}{\sqrt{gd}} \quad (11)$$

$$\tau = \rho g d S \quad (12)$$

For Eq. 9 – 12 Q is the regional regression discharge (cms), A is the cross-sectional area (m²), ρ is the density of water, g is the acceleration of gravity (m/s²), S is the channel slope, w is the cross-sectional width, and d is the estimated depth from Eq. 8.

By creating boxplots of the grouped categorical variables, I examined relationships between several of the river variables and the geomorphic and land use variables. These boxplots help establish broad relationships across the whole study area.

To analyze the downstream patterns in active channel width of the study area, I employed hyperscale graphs (Carbonneau et al., 2012; Fonstad and Marcus, 2010). These pyramidal graphs illustrate statistical relationships of two river variables across multiple

spatial scales. For this analysis, I examined the correlation between pairs of variables using the Pearson correlation coefficient. This statistical test shows the strength of the linear relationship between the two variables and allows for a test of significance, in this case, testing for statistical significance at a 99% confidence interval ($p=0.1$). These graphs achieve this multi-scalar view by utilizing a moving window to calculate the statistical relationships for each of the different scales. For example, the very top of the pyramid represents the correlation coefficient for the entire dataset (for this dataset, $n = 10,776$). The next row of the pyramid has window size of $n = 10,774$ and continues to the bottom row, which has a window size of $n = 2$. This type of analysis can illustrate patterns not always visible with other types of reach or segment scale analysis.

Habitat Mapping

All of these hydrologic variables can be used as indicators of geomorphic patterns in the river; however, we can take these data and apply them to questions about the river beyond geomorphology. One potential application is using these data as the basis for spatial continuous habitat maps for fish or other lotic species. The Middle Fork John Day River provides important habitat for populations of spring run Chinook salmon and summer Steelhead. By using the extracted and derived geomorphic variables, it is possible to calculate a habitat suitability index (HSI) for adult migrating Chinook. One such index was published by Raleigh et al. (1986) and included five habitat variables for adult migrating chinook on a scale of 0 to 1: water pH, water temperature, dissolved oxygen, percent pools, and a measure of pool quality (width/depth ratio). The water pH, temperature, and dissolved oxygen are important physiological requirements for fish, but for this example, the assumption is that these variables are within normal ranges and

would have an HSI value of one. Pools are an important habitat requirement for migrating Chinook because they provide cool, lower velocity areas for fish to hold and rest as they migrate to spawning sites (Raleigh et al., 1986) . Percent pools was calculated by averaging the length of the river classified as pools over a one-kilometer moving window, 500 meters upstream and 500 meters downstream, for each sample point along the river centerline. Pools were classified by their width/depth ratio (active channel width and derived depths for the P5 discharge) and the dominant pool class in each one-kilometer moving window determined the HSI value. The HSI values for percent pools and pool class were assigned based on the linear functions outlined by Raleigh et al. (1986). Calculating the mean HSI value for the five habitat components identified the overall HSI for each sample point.

Results

Aerial Photography

The flight collected 1,483 photographs, all of which were within the target ground resolution of 5 to 7 cm per pixel. The planned flight lines and camera timing provided sufficient forwardlap and sidelap for a SfM reconstruction with only a few small gaps in the coverage. The seven sections of photographs took approximately 60 hours to process through the Photoscan workflow to the orthophoto and DEM outputs. Of the 60 hours, approximately 20 hours required direct interaction and 40 hours of unattended processing time. The output datasets had uniform pixel resolutions of 10 cm that accounted for the effects of the mosaicing and orthorectification processes in Photoscan (Figure 26 and Figure 27).

The SfM orthophoto results were excellent, with sufficient resolution to identify individual logs in engineered logjams along the river, but too coarse to identify sediment sizes (Dugdale et al., 2010). The exceptions were in a few areas where the helicopter drifted from its flight lines and created gaps in the photo coverage (Figure 28). Most of these gaps were in the floodplain areas of the valleys, so there was little impact on river data extraction. Two small areas (less than 10 meters each) in the narrow canyon sections had additional gaps in the photo coverage. I filled the resulting gaps with data from the 2008 NAIP orthophotos. The orthorectification and mosaicking process created artifacts in several locations (Figure 28) that resulted in blurry or noisy sections of the orthophotos. These areas only slightly affected the visual interpretation of the imagery and likely were the result of an incomplete and noisy DEM underlying the orthophotos.



Figure 26: Sample orthophotograph located in segment E. The Middle Fork is at the bottom of the photo and tributary is the recently reconstructed Granite Boulder Creek. Flow is right to left.

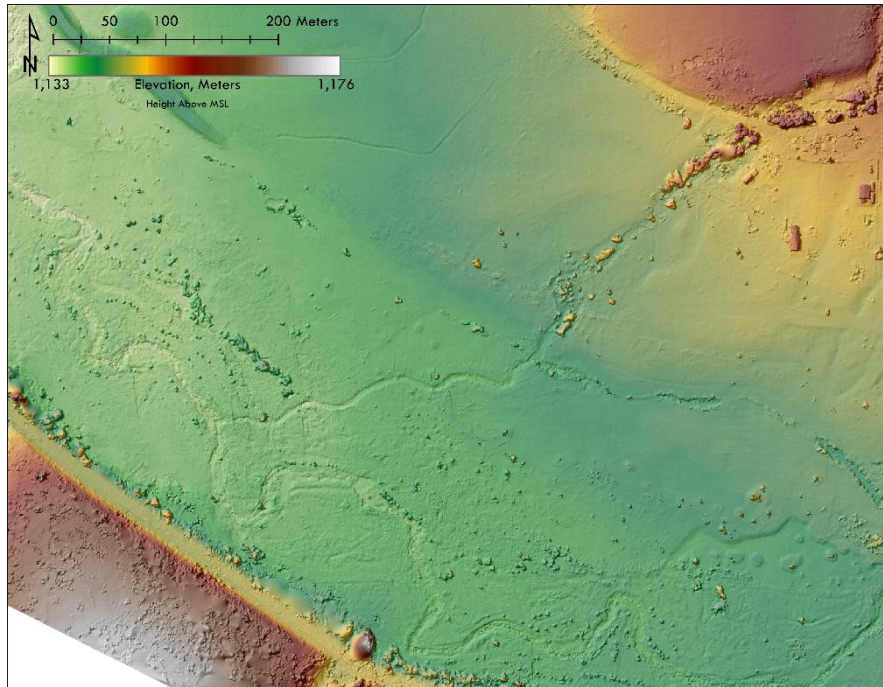


Figure 27: Sample DEM of the same area as Figure 3.



Figure 28: Examples of the effects of missing photo coverage (left) and orthorectification artifacts (right).

The accuracy of the georeferencing of the SfM data was excellent (Table 9), with sub-centimeter scale mean absolute errors (MAE) in all three axes and centimeter scale uncertainties (RMSE and standard deviations). These statistics do not include the raw errors and uncertainties from the GPS points (Table 9). The post-processed GPS points had mean absolute errors of 17.5 cm horizontal and 29.3 cm vertical. The errors in the GPS points ranged from 10 cm to more than a meter in both horizontal and vertical directions.

Table 9: Error, accuracy, and uncertainty for SfM georeferencing (top) and the post-processed GPS points (bottom). All values are in meters.

<u>SfM</u>	X Error	Y Error	Z Error
Mean Absolute Error	5.85×10^{-5}	1.56×10^{-5}	5.34×10^{-5}
Standard Deviation	0.016	0.026	0.017
RMSE	0.014	0.018	0.015
Minimum Error	-0.035	-0.095	-0.075
Maximum Error	0.063	0.086	0.061
<u>GPS</u>			
	Horz	Vert	
Mean Absolute Error	0.175	0.293	
Standard Deviation	0.183	0.198	
RMSE	0.252	0.354	
Minimum Error	0.100	0.100	
Maximum Error	1.200	1.100	

The SfM-derived DEMs at first glance were extremely detailed and precise, but on closer inspection, it was apparent the accuracy of the elevation data was outside an acceptable error range when compared to LiDAR data. The most serious problem was a systematic error in the DEMs, discovered by comparing the SfM data to a 2008 LiDAR survey. An example of this systematic error, an alternating pattern of positive and negative differences, is visible along the valley floor in Figure 29. The error in the elevation values can be attributed to two factors, the orientation of the photos along the

flight lines and the imprecision in the vertical component of the GPS control points. James and Robson (2014) have shown that systematic error in SfM similar to this can be the result of the parallel geometry of photographs along the flight lines. This parallel geometry allows the SfM algorithms to accumulate error from radial lens distortions, affecting the accuracy of the reconstruction. The imprecision in the GPS elevations of the ground control points (Table 9) contributed to the overall error in the DEMs. The error in individual GPS points was not systematic, leading to the conclusion that these errors affected the overall accuracy of the SfM DEMs but not in a quantifiable way that could be separated from the systematic errors created by parallel geometry. Two other problems affected the vertical accuracy of the DEMs: errors where photo overlap was low, and inconsistency in capturing vegetation. Low overlap and incomplete coverage have the effect of creating abrupt edges in the DEMs, creating a stair-step pattern in the DEM that is visible in the left side of Figure 29. While some researchers have had success mapping vegetation with SfM (Dandois and Ellis, 2013; Mathews and Jensen, 2013), I found that the DEMs did not consistently reflect accurate vegetation heights. In one area along the riparian corridor of a tributary, the DEM contained a dense stand of Alder bushes 1-2 meters tall, but adjacent 15-20 meter conifers were absent from the DEM.

Riverscape Mapping

The primary and derived data for all 10,776 sample points are plotted in Figure 30 and Figure 31. The largely automated process produced reliable data with no obvious outliers or anomalous results and the conversion of the data to a stream normal coordinate system greatly simplified the processing and display of the data. Because the level of uncertainty in the derived datasets (depth, stream power, velocity, Froude number) is

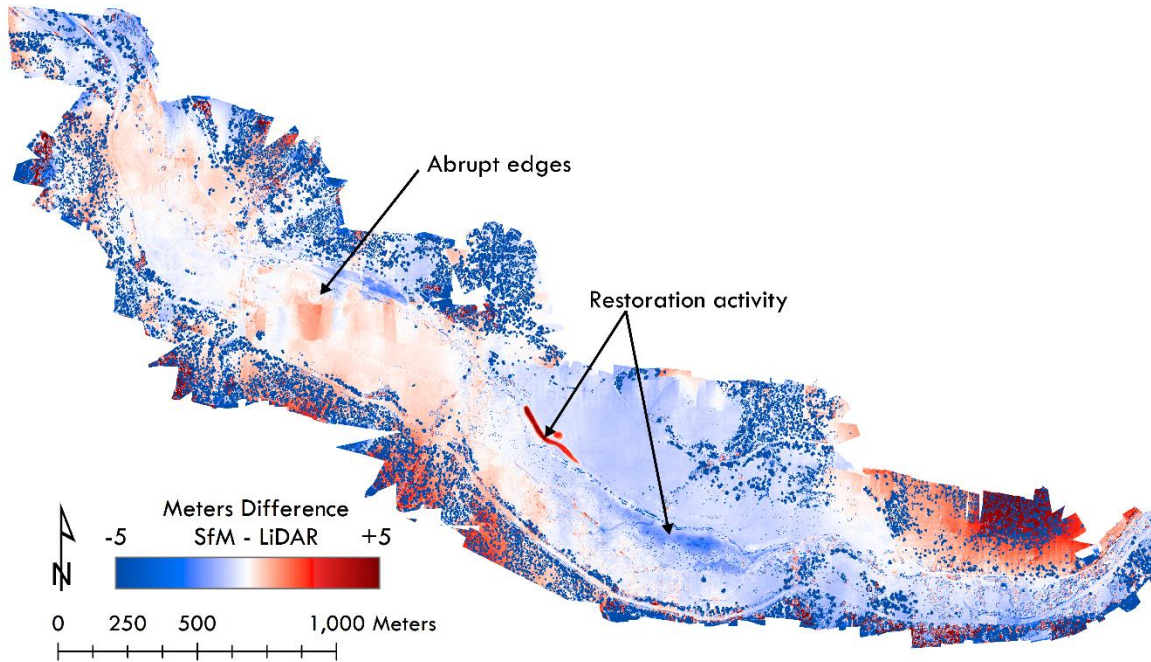


Figure 29: Map of SfM - LiDAR differences showing systematic errors in the SfM data from the parallel camera geometry and abrupt edges from incomplete coverage. Flow is right to left.

high, they are purely exploratory in this study.

Aggregating the data using the classified variables eliminated some of the noise from the plots of the downstream variables shown in Figure 30. Figure 32 shows the active channel width distributions of each of the nine segments of the river. Most segments exhibit a long-tailed distribution, but the median values show increased active channel width with downstream distance. The distributions of active channel widths across the three channel units (Figure 33) also exhibit long-tailed distributions, but there are only small differences in the median values. The influence of the underlying geology on both active channel width (Figure 34) and valley width (Figure 35) are seen with the weaker rocks of the Clarno formation giving rise to wider channels and valleys. Current cattle grazing intensity (Figure 36) illustrates that intensely grazed segments have wider

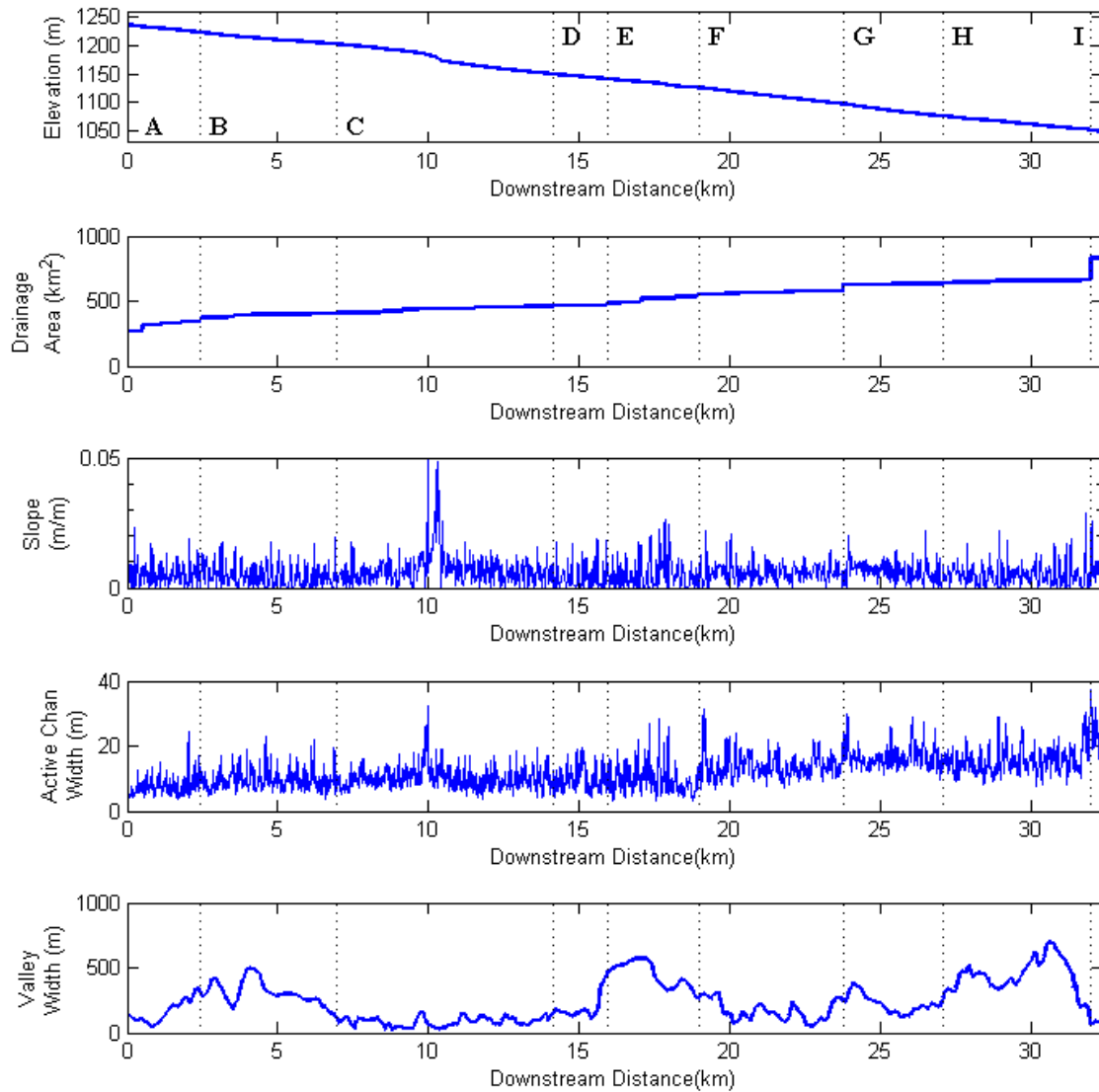


Figure 30: Primary morphologic variables for the study area. Dotted lines represent river segment breaks, labels are at the top.

active channels than those with moderate or no grazing. The amount of stream restoration (Figure 37) does not seem to influence channel width.

Hyperscale graphs help explore the relationships between active channel widths and variables such as downstream distance, slope, and valley width. Active channel width versus downstream distance (Figure 38) is an illustration of downstream hydraulic geometry. At the larger spatial scales, above an 18 km window, width and downstream

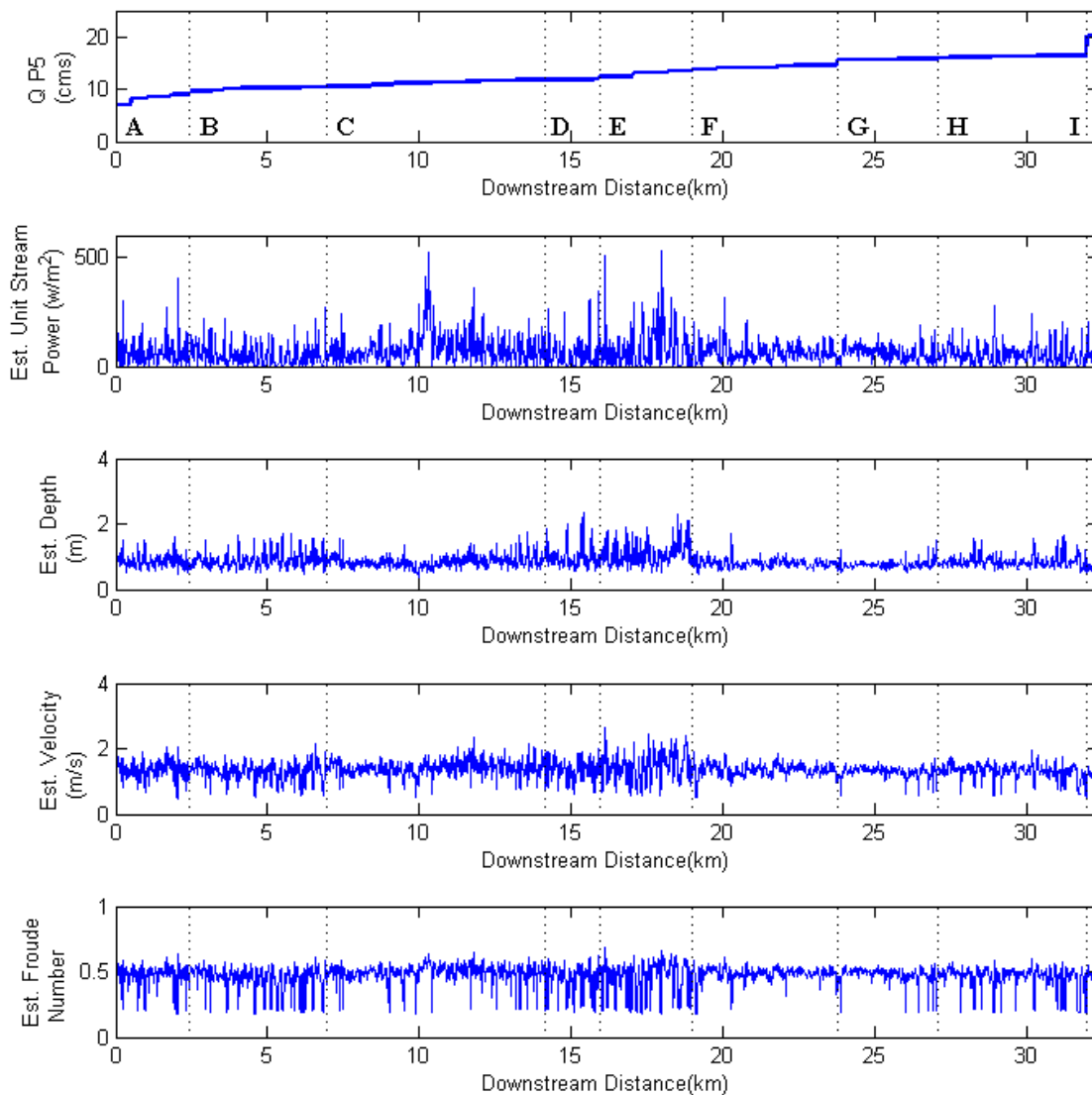


Figure 31: Derived hydrologic variables for the study area. Dotted lines represent river segment breaks, labels are at the top.

distance show a moderate positive correlation. Below the 18 km window, the pattern of correlations becomes more complex, with both positive and negative correlation coefficients showing that there may be other factors contributing to width. In Figure 39, active channel width versus slope shows no to very weak positive correlations at the larger and intermediate scales, while at the local scale, 1 km or less, there are stronger relationships with width. The relationship between active channel width and valley width

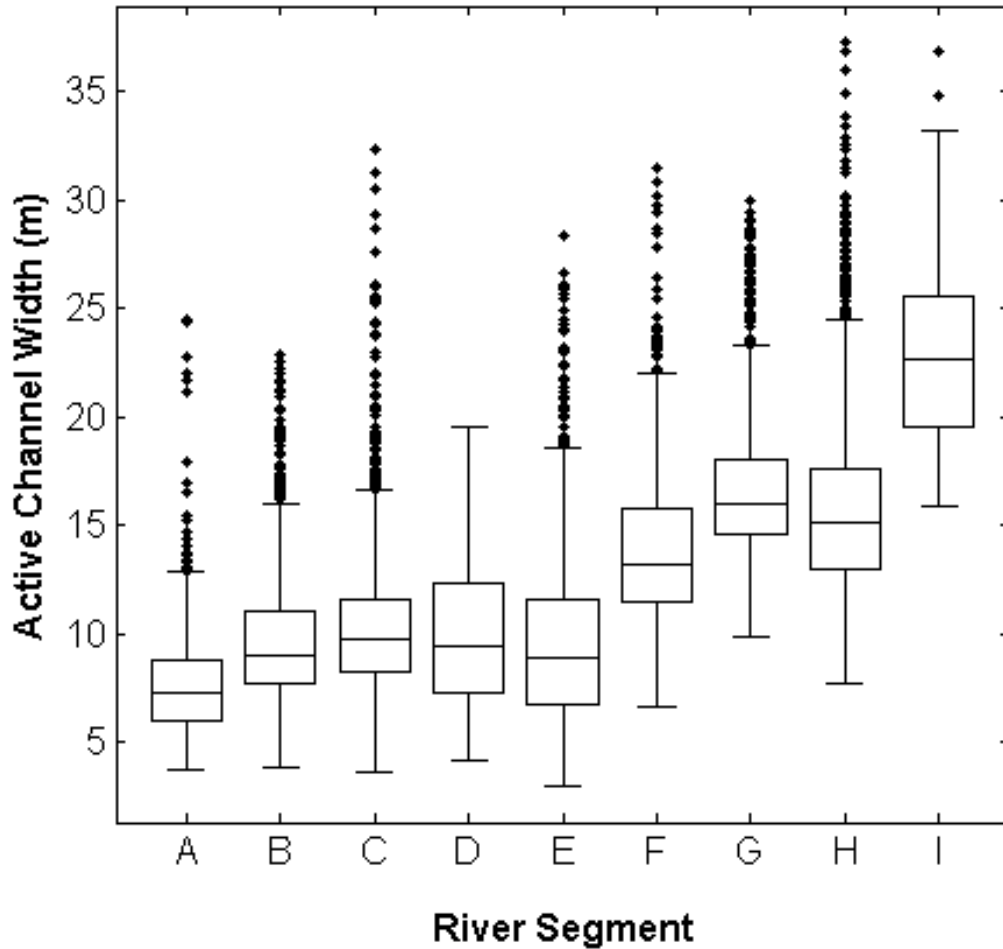


Figure 32: Boxplot of the distribution of active channel widths for each river segment.

shows a weak negative correlation throughout most scales (Figure 40). In this graph, we can see a pattern reflecting the alternating wide and narrow valleys in the 2 to 4 km range because of the alternating positive and negative correlation values.

Habitat

The average habitat suitability index values for adult migrating Chinook salmon (Figure 41) range from 0.82 to 0.92, with a majority of the river falling in the upper end of the range. The spatial pattern of suitability shows that there are large segments of the river that provide excellent habitat, which are punctuated with short sections that are less suitable and could act as impediments to upstream migration.

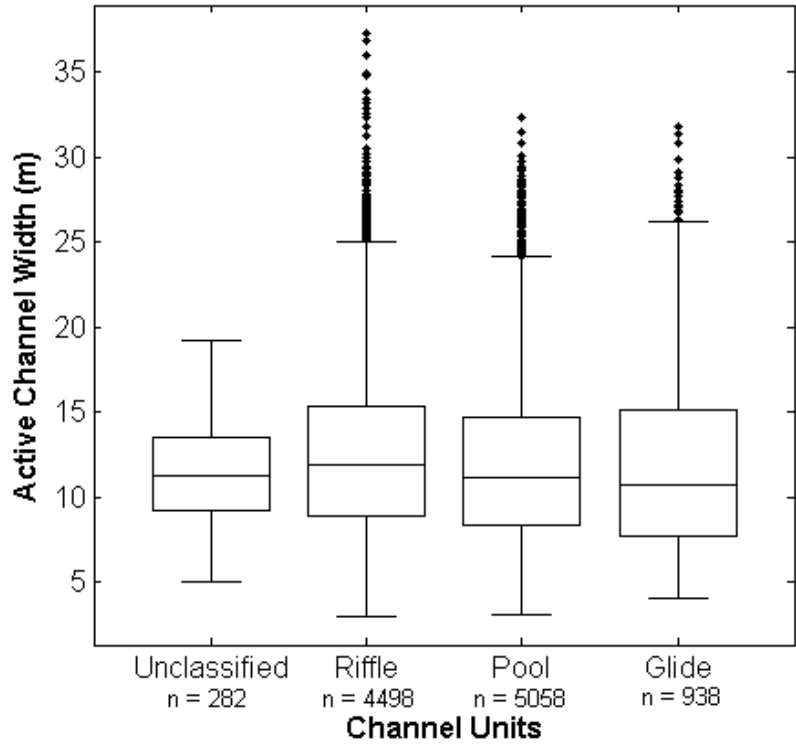


Figure 33: Boxplot of active channel widths for each of the classified channel units. N-values are the number of samples in each class (total = 10,776).

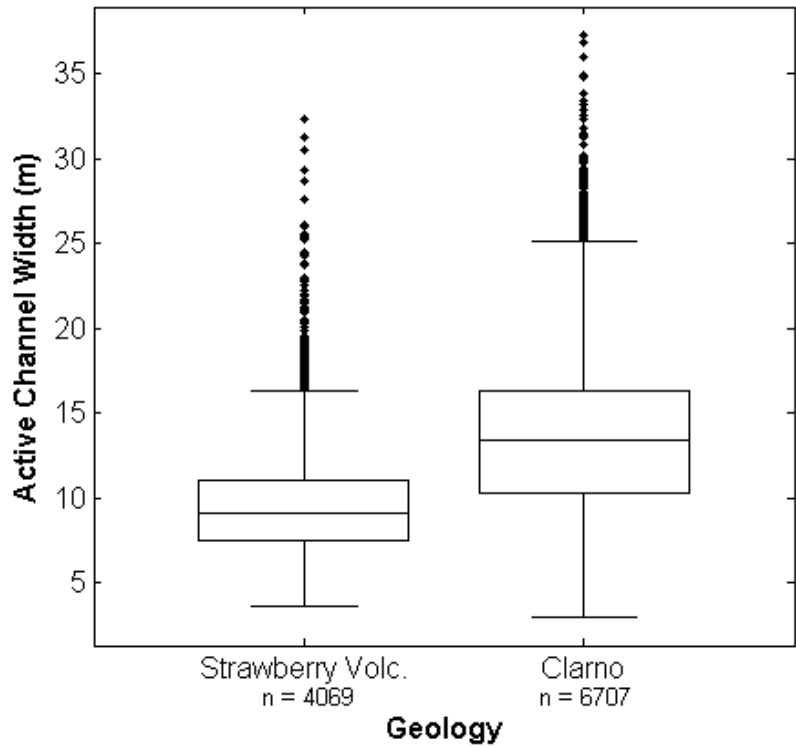


Figure 34: Boxplot of active channel widths for the different bedrock geologies. N-values are the number of samples in each class (total = 10,776)

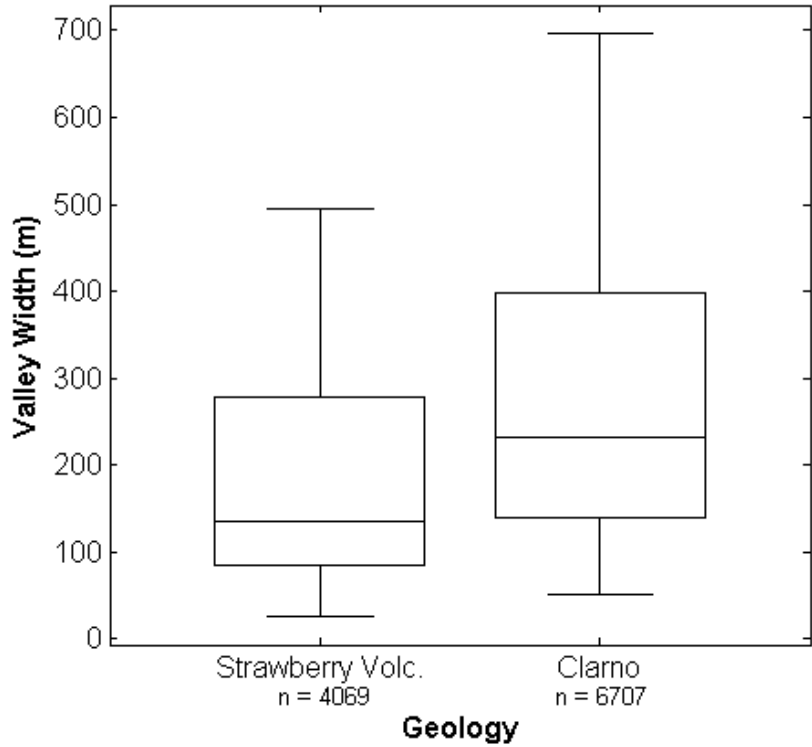


Figure 35: Boxplot of the distributions of valley widths for the different bedrock geologies. N-values are the number of samples in each class (total = 10,776)

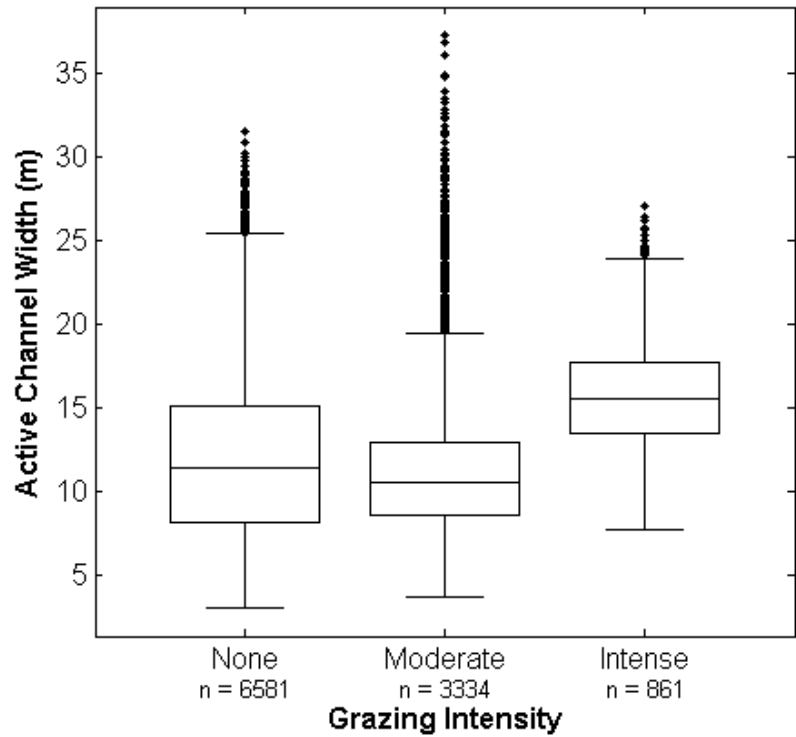


Figure 36: Boxplot of the distributions of active channel widths for each of the current cattle grazing intensities. N-values are the number of samples in each class (total = 10,776)

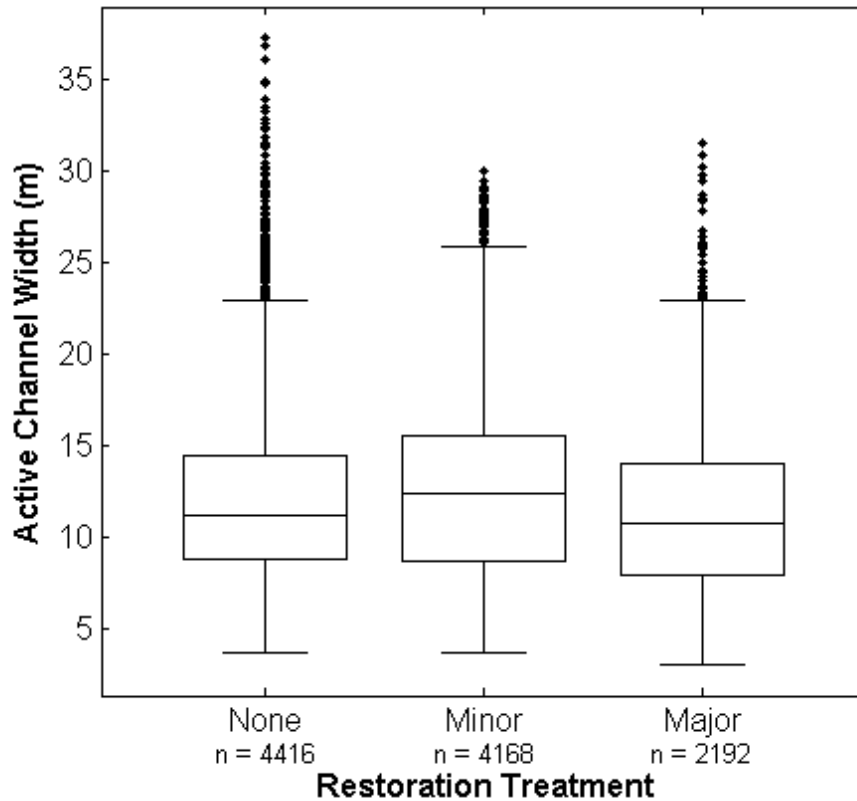


Figure 37: Boxplot of the distribution of active channel widths for the different river restoration treatments. N-values are the number of samples in each class (total = 10,776)

Discussion

Aerial Photography

One planned dataset was the extraction of bathymetric data, either by direct SfM measurements (Woodget et al., 2014) or spectral depth mapping techniques (Legleiter and Fonstad, 2012; Marcus and Fonstad, 2008; Walther et al., 2011). The SfM elevations in the river did not match depth data measured at several cross sections throughout the study area, making the dataset unusable. Instead, I used the cross section data to create color-depth regression curves for several band ratio combinations, but none of these regressions had adequate fits to enable spectral depth mapping. I can attribute the failure of both of these methods partly to the shutter speed, water turbidity, and the radiometric resolution of the camera. The shutter speed (1/800 second) was optimized to produce

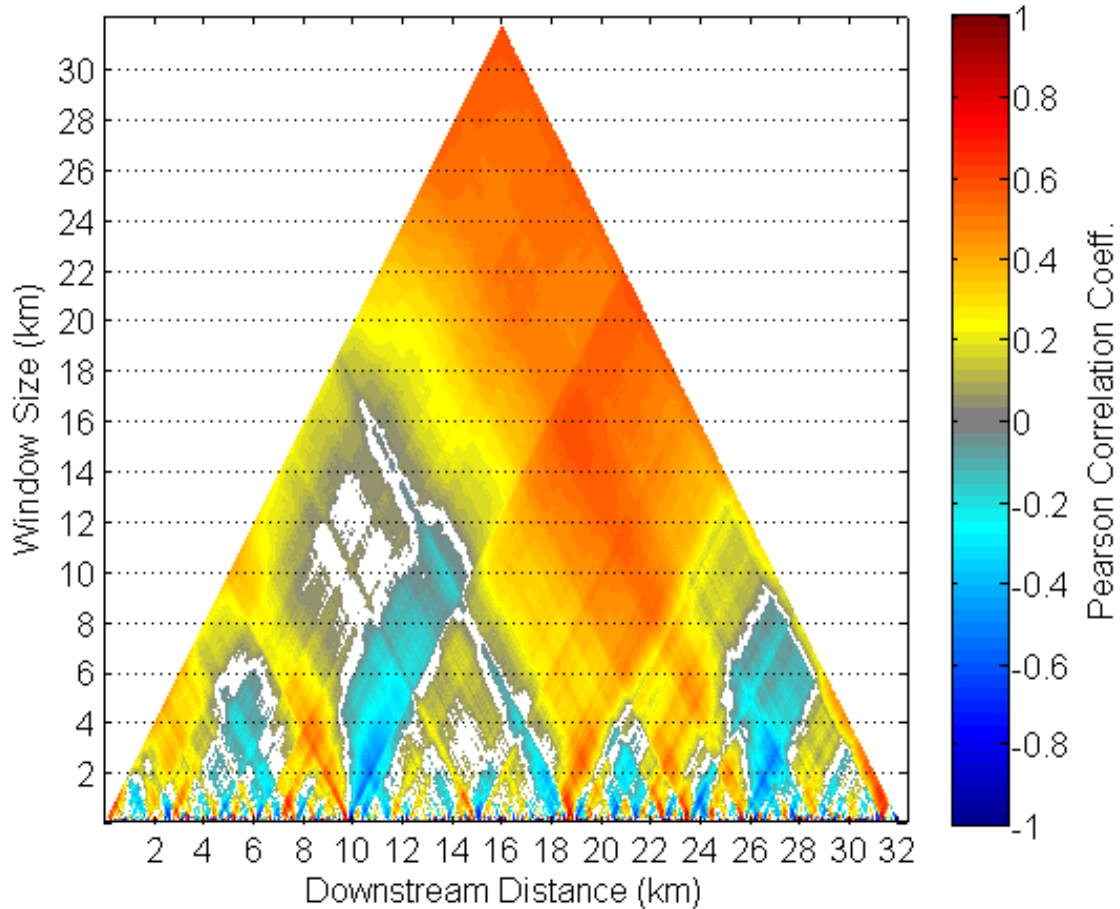


Figure 38: Hyperscale graph of Pearson correlation coefficients of active channel width as a function of downstream distance. White areas within the triangle are portions of the analysis that did not meet the significance criteria ($p = 0.05$).

evenly exposed images that balanced the brighter areas, like dry flood plain vegetation, and darker areas, such as conifers, water, and shadows. A slower shutter speed would shift the exposure to better capture the darker areas but increase the risk of over exposing brighter areas. To conserve disk space on the camera for the two-hour flight, the photographs were captured in JPEG format with 8-bit radiometric resolution (256 shades of gray per band), which limits the camera's ability to capture the true dynamic range of the scene. In principle, to increase the radiometric resolution I could have saved the images as RAW format images, though this could have led to memory issues in collection and processing. On the Canon T5i, the RAW format provides approximately

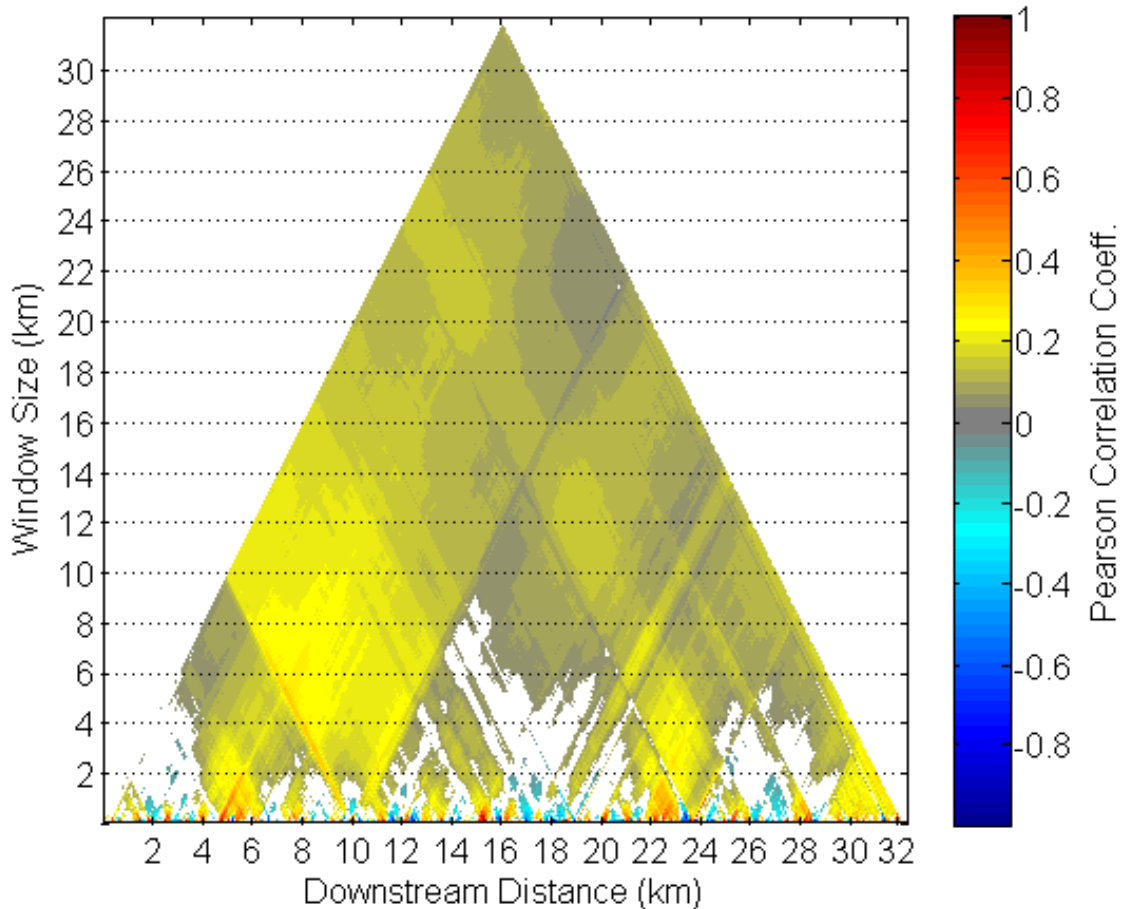


Figure 39: Hyperscale graph of Pearson correlation coefficients of active channel width as a function of slope. White areas within the triangle are portions of the analysis that did not meet the significance criteria ($p = 0.05$).

14-bit (16,384 shades of gray per band) radiometric resolution, which could have provided more color information over the darker areas on the water and shadowed areas. This extra color information may have provided enough color depth to create accurate spectral depth regressions, assuming ideal weather and water conditions.

Slight modifications to the setup and execution of future aerial photography should solve all of the issues with the orthophotos and DEMs, creating better results. To remedy coverage gaps and low overlap, I recommend increasing the camera interval and using closer flight lines. Collecting RAW imagery could reduce the difficulties with

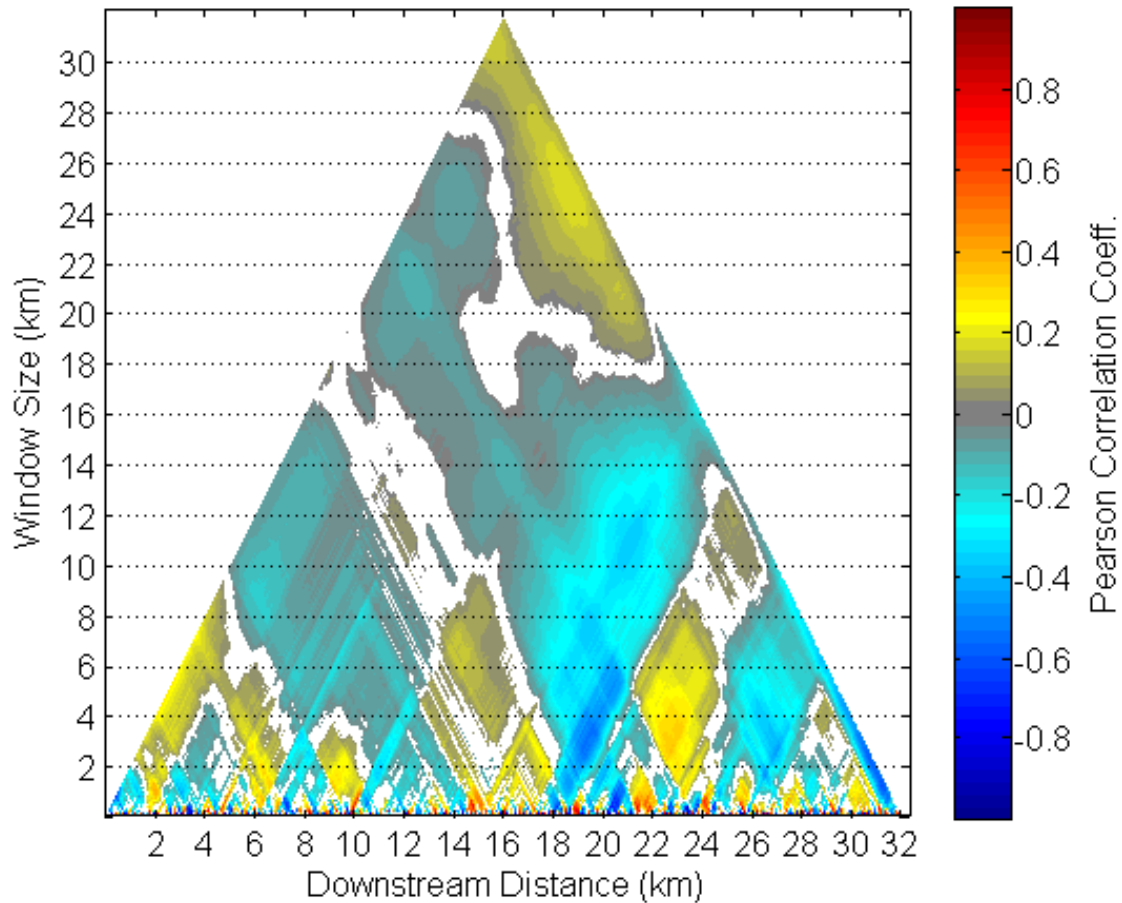


Figure 40: Hyperscale graph of Pearson correlation coefficients of active channel width as a function of valley width. White areas within the triangle are portions of the analysis that did not meet the significance criteria ($p = 0.05$).

exposure and more extensive testing could ensure that all aspects scenes have the correct exposure. By collecting ground control points with an RTK GPS, it would reduce errors in georeferencing. The greatest problem to overcome is the systematic error caused by the parallel camera geometry. The simplest solution is to create convergent camera geometry, and James and Robson (2014) suggest several solutions to achieve this geometry in small unmanned aerial systems. One solution is the use of a single camera mounted in a gimbal that can be pointed off-nadir and adjusted to create convergent geometries. Another option would be to use multiple off-nadir cameras, which would not only create convergent geometry, but also increase coverage and reduce overlap problems.

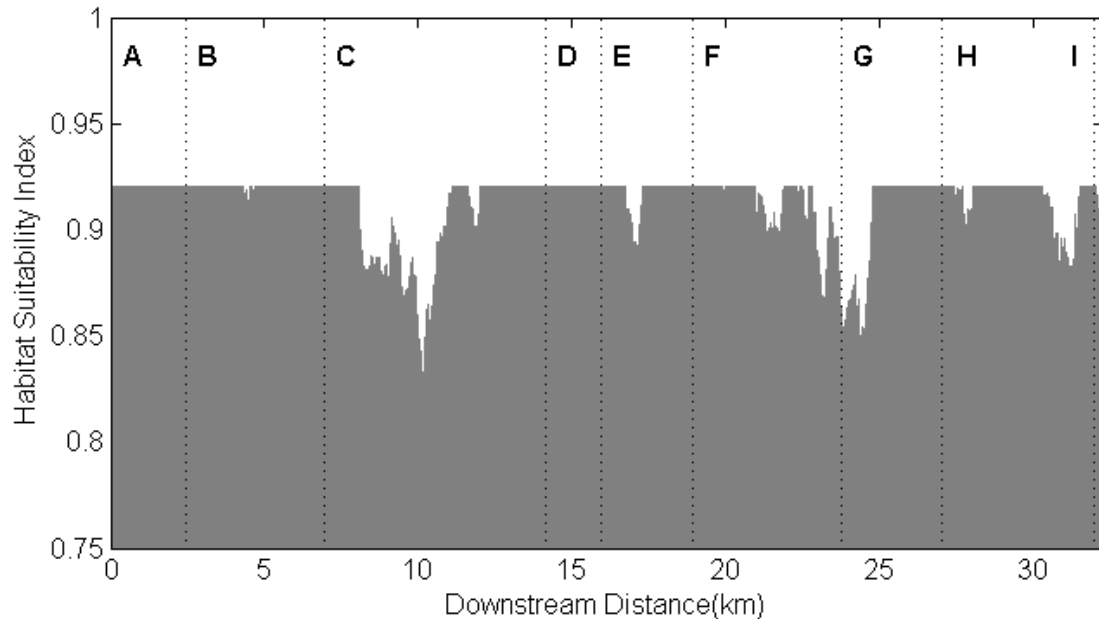


Figure 41: Downstream plot of habitat suitability index (HSI) for upstream migrating Chinook salmon.

Riverscape Mapping

The heterogeneity of the Middle Fork is apparent in the downstream plots of the extracted and derived variables (Figure 30 and Figure 31). With these raw data, it is difficult to differentiate the natural variations in the river from those that are the direct result of human influence even though we know where to look for them. The one exception is the lower portion of segment E, where the active channel width becomes very narrow compared to the surrounding channel. This section of the channel is the final path of the dredge mining activity that left an almost straight channel about four meters wide and approximately two meters deep. This straight section is visible in the plot of channel slope, where the rise in slope around 18 km marks the transition from the natural channel down into the dredged channel.

As mentioned in the results, the derived variables of discharge, depth, velocity, unit stream power, Froude number, and shear stress, are all approximations, though

reasonable, leading to a high level of uncertainty associated with each one. The uncertainty in these data originates from the uncertainty in the regional regression equation (Eq. 3), which was used in estimating depth (Eq. 8). The depths that the inverted Manning's equation predict do not actually correspond to changes in riffles and pools, which probably are a result of the channel units not having a distinct width signature (see discussion below). In the equations of the remaining derived variables, discharge and depth figure prominently, which propagates the uncertainty into these variables. Despite the high uncertainty, these variables are important in understanding the processes and form of the river. If the discharge values were validated and depths that are more accurate were obtained, these variables could be useful in creating a more complete picture of the riverscape.

The legacy of human impacts on the channel has complicated the riverscape of the Middle Fork. Despite these impacts or because of them, there are several definite relationships between the distance downstream and classified variables. Comparing the active channel widths across the nine different segments in Figure 32, we see the general downstream trend of increased width with downstream distance, expected with downstream hydraulic geometry. Two areas that do not fit that general trend are segments E and H. Segment E consists of the valley section that has been the focus of intense restoration activity in an attempt to rehabilitate the stream from historic dredge mining activity. The most recent phase of restoration, completed in the summer of 2012, filled in a second channel left by the dredge barge on the north side of the valley bottom. The meandering channel on the south side of the valley has not yet adjusted to the increased flow, causing the break in the downstream trend. Segments G and H exhibit the

largest range of active channel widths seen in all the segments. Landowners straightened and pushed sections of the river to the side of the valley in order to facilitate cattle grazing. The wide range of width in this section appears to be a reflection of these modifications to the river channel. The large increase in width in segment I is the result of the combination of the input of Camp Creek, the largest tributary in the upper part of the basin, and an increase in slope, causing the channel to become plane-bedded.

Richards (1976) demonstrated that generally rivers show a difference in the width of the channel between riffles and pools. The data from the Middle Fork (Figure 33) suggest that all three of the mapped channel units had similar width distributions. These data agree with my field observations that width does not vary greatly between riffles and pools at the reach scale. Another possible control on width could be the underlying geology of the valley floor and adjacent hill slopes, which could act as a control on valley width and channel width (May et al., 2013; McDowell, 2001). In Figure 34 and Figure 35, the parts of the river in the Clarno formation have a higher median valley and channel width. Because these data also incorporate the downstream hydraulic geometry signal from Figure 32, it is difficult to determine how much the geology is influencing the width throughout the study area.

From my field observations of the intensely grazed portions of the study area, I hypothesized that the intensity of cattle grazing would increase the active channel width when compare to other sections of the river. In the downstream plot of active channel width (Figure 30), it is difficult to identify any reaches that are anomalously wider than others based on the current grazing intensities. Aggregating the data by grazing intensity confirms that the intensely grazed portion of the study area does have a higher median

width compared to areas with moderate or no grazing. The last categorical control on width was at restoration treatment. In the field, the sections of the river that have different restoration treatments visually look different. The analysis showed that the distributions of width in each of the three categories were almost identical. Because the restoration activities are a recent addition to the river, they may not have yet expressed their influence.

In the hyperscale analysis of active channel width versus downstream length, the positive correlations coefficients in the larger window sizes, 18 – 32 km, are indicative of the expected DHG relationship of a channel that widens as drainage area increases with distance downstream. From the 18 km window down to 8 km, the river divides into two zones, with the lower half of the river holding on to the DHG relationship, but in the upper half, that relationship begins to breakdown. This breakdown appears to be triggered by the steep, narrow section of the river at the 10 km downstream mark, where the river narrows slightly. The narrowing of the river over a relatively short section has a large effect on the relationship at these intermediate scales. In the 2 – 6 km window, the frequency of the alternating pattern of positive and negative correlations corresponds to the alternating wide and narrow valleys, suggesting that valley width may be a control on width at these scales. Below the 2 km window, the oscillation of positive and negative correlations becomes more frequent. Carbonneau et al. (2012) suggested that that the patterns at this scale could relate to riffle pool sequences, but an initial examination of the pattern in relation to the classified channel units data does not support that relationship. It will require additional investigation to determine what drives these patterns.

The other two hyperscale analyses do not have the same well-defined patterns as active channel width and downstream distance. The graph of active channel width versus slope shows weak positive correlations at most scales, suggesting that slope has little influence on width at most scales. There is a relationship at the finer window sizes of 1 km or less, where there is again a high frequency switching of the coefficients. In the comparison of active channel width versus valley width, the notable relationships are the weak negative correlations, which suggest that stream width decreases in wider valleys. In this case, large changes in valley width compared to small fluctuations in channel width are causing a false signal.

Most of the larger scale patterns in these hyperscale analyses I can attribute to physical aspects of the river such as geology or the downstream hydraulic geometry. By comparison, the smaller scale patterns are more difficult to interpret and an important next step for this type of analysis would be to export the hyperscale results into a GIS environment where hyperscale patterns could be better visualized in the context of other GIS data and imagery. This could reveal what other variables might be causing variations in width, from such features as bank or in-stream vegetation or position in relation to meander bends.

Habitat

Without spatial data on water pH, dissolved oxygen, and water temperature, this HSI for the Middle Fork is only an estimate. A majority of the river had an HSI value 0.92 indicating that the Middle Fork provides excellent habitat. All of the stretches of river that fall below the maximum value I can attribute to the physical setting of the river. The large dips in the C and F segments are located in steeper, narrow valleys where the

river transitions away from a regular riffle-pool sequence and incorporates long plane bed stretches with significantly fewer pools. The small dip in the E section is located at the lower end of an ongoing major restoration project that will take time to adjust to the impact of the restoration activity. The drops in HSI at the beginning of the G and H sections are in wider valley sections that are now in conservation ownership, but were straightened by past land owners to facilitate grazing, leading to a lower percent pools value. Straightening also occurred along the last major dip at the downstream end of the H segment, currently used for active cattle grazing.

The two narrow valley sections are natural features in the riverscape and have not been impediments to the upstream migration of Chinook. The other areas with lower HSI values show the impact of human modifications to the river. By collecting continuous variables, like those collected for this HSI for the spawning and rearing habitat, it would be possible to combine them to create a spatial HSI that accounts for all of the life stages of the Chinook. Implementing these data could then help identify areas of the river that are lacking sufficient habitat, which could prioritize them for future restoration.

Conclusions

Using an off the shelf digital SLR camera, I was able to collect 5 cm resolution aerial photography for a 32-km segment of the Middle Fork John Day River. The outputs from the SfM process provided high-quality orthophotographs for the study area with only a few gaps in coverage. The corresponding 10 cm resolution digital elevation model suffered from systematic errors caused by the parallel geometry of the aerial imagery, but current research shows that the errors can be eliminated in future studies. Despite the issues that I encountered, SfM has the potential to be a powerful and inexpensive tool for

fluvial remote sensing with a few refinements. These refinements include correcting the camera geometry from parallel to convergent, collecting control points with high-accuracy GPS, improving flight planning to avoid gaps in the imagery, and correcting the exposure and increasing the radiometric resolution of the imagery to facilitate spectral or SfM-derived bathymetric measurements.

While the impacts of human activity on the Middle Fork are apparent in the field, in the collected data it is difficult, with few exceptions, to differentiate human activity from natural patterns in the current downstream patterns of channel morphology. Both the boxplots of classified data and the hyperscale analysis show that there exist differences in the downstream patterns at several different spatial scales, but these will need to be investigated further to determine the causal relationships. One explanation could be that enough time has passed for the river to adjust partially to the historic human disturbances and that the river has not had enough time to adjust to the recent restoration activities.

Mapping the habitat suitability index for migrating adult Chinook showed that the river has high quality habitat for this particular life stage of the salmon. The HSI highlighted areas that could act as an impediment to their upstream migration and could be potential targets for future restoration. Of course, migrating adult salmon are only one piece of the complex puzzle that is fish habitat in the Middle Fork. To better effectively map habitat and potential restoration sites, we would need to consider the spawning and juvenile habitats of salmon and for Steelhead and Bull Trout to ensure that wide range of habitats are present to help maintain and, hopefully, start to recover the populations of these critical species.

CHAPTER V

SUMMARY

My research objectives for this dissertation were to determine the error and uncertainty that are inherent in SfM datasets, use SfM to map and monitor geomorphic change in a small river restoration project, and use SfM to map and extract data to examine multi-scale geomorphic patterns for 32 kilometers of the Middle Fork John Day River. The three chapters of this dissertation illustrate how SfM can be used to collect high spatial resolution topographic data for fluvial geomorphology. The methods and analyses can also extend beyond fluvial geomorphology into all facets of earth surface process mapping and monitoring. The three studies, done at a variety of spatial scales demonstrate the versatility of SfM as a topographic data collection technique. A significant portion of each chapter was devoted to learning what aspects of SfM worked as expected and what parts of the method can be improved for future studies.

In Chapter II, I found that SfM produces extremely consistent results that exhibit an average uncertainty of approximately two centimeters. The uncertainty includes a pronounced systematic distortion that resulted from the survey method and camera calibration. I will be undertaking future research on the effects of the non-linear errors and how to eliminate these errors in SfM. Other areas of future research include how differences in georeferencing affect uncertainty at different spatial scales and how the magnitude of uncertainty in SfM might impact change detection studies at a variety of spatial scales.

By combining the CTWSRO data with my own in Chapter III, I found that Granite Boulder Creek has shown some minor channel and vegetation changes in its first year since reconstruction. The changes were associated with surficial changes in bed and bank sediments and identified throughout the new channel. Continued monitoring by a variety of methods is going to be important in the future in order to assess the evolution of this restoration project through time. The SfM results in this chapter had several shortcomings that will help inform additional research on the optimal number and spacing of ground control points, the best survey patterns and platforms, and the possibility of extracting bathymetry from the images and point clouds.

In Chapter IV, the large volume of spatially continuous channel morphology data extracted from the SfM orthophotos provided a holistic view of the downstream patterns in channel morphology. While it was difficult to differentiate the impacts of human activities from the natural variations in the stream, the statistical and hyperscale analyses did show that there are downstream patterns in the river that exist at a variety of spatial scales. The SfM data also showed that using an off-the-shelf digital SLR camera is an acceptable method to collect high-resolution aerial photography. The imagery and the SfM process provided high-quality orthophotographs, but the digital surface model suffered from systematic errors, similar to the systematic errors seen in Chapter II from the parallel geometry of the photographs. For future helicopter-based SfM collection missions, I will be actively working to correct the camera geometry from parallel to convergent, finding efficient ways to collect control points with high-accuracy GPS, improving flight planning to avoid gaps in the imagery, and correcting the exposure and

increasing the radiometric resolution of the images to facilitate spectral or SfM-derived bathymetric measurements.

SfM offers many benefits to researchers in the fields of remote sensing and geomorphology. It is a highly flexible method and can be used at a variety of spatial scales and with a wide range of instruments and platforms. SfM has been used to create 3D reconstructions at the widest range of scales of any remote sensing method, ranging from only a few centimeters (Koutsoudis et al., 2014) to mapping tens of kilometers (Chapter IV). With images collected from just about any digital camera SfM can be used to build a 3D scene. There is even potential to use scanned film images to create reconstructions of historical landscapes. The flexibility in scale and instruments also allows for a wide-range of platforms including hand-held cameras on the ground to a variety of aerial platforms.

Compared to other survey techniques, SfM is a lower cost method in terms of both equipment and field time. The most expensive part of a SfM survey is a precision positioning instrument to collect ground control points, but this is a requirement of all topographic survey methods. Beyond that, the only required equipment is a digital camera. Optional equipment includes commercial software and/or camera platforms. SfM also provides a cost savings in the amount of time spent in the field collecting data. Traditional survey methods, total station and GPS, require significant time investments to achieve high resolution surveys (Bangen et al., 2014) and SfM can reduce the time necessary to cover both large and small areas. The lower price point and flexibility of SfM increases its accessibility to a wider range of researchers (see Figure 42 for comparisons).

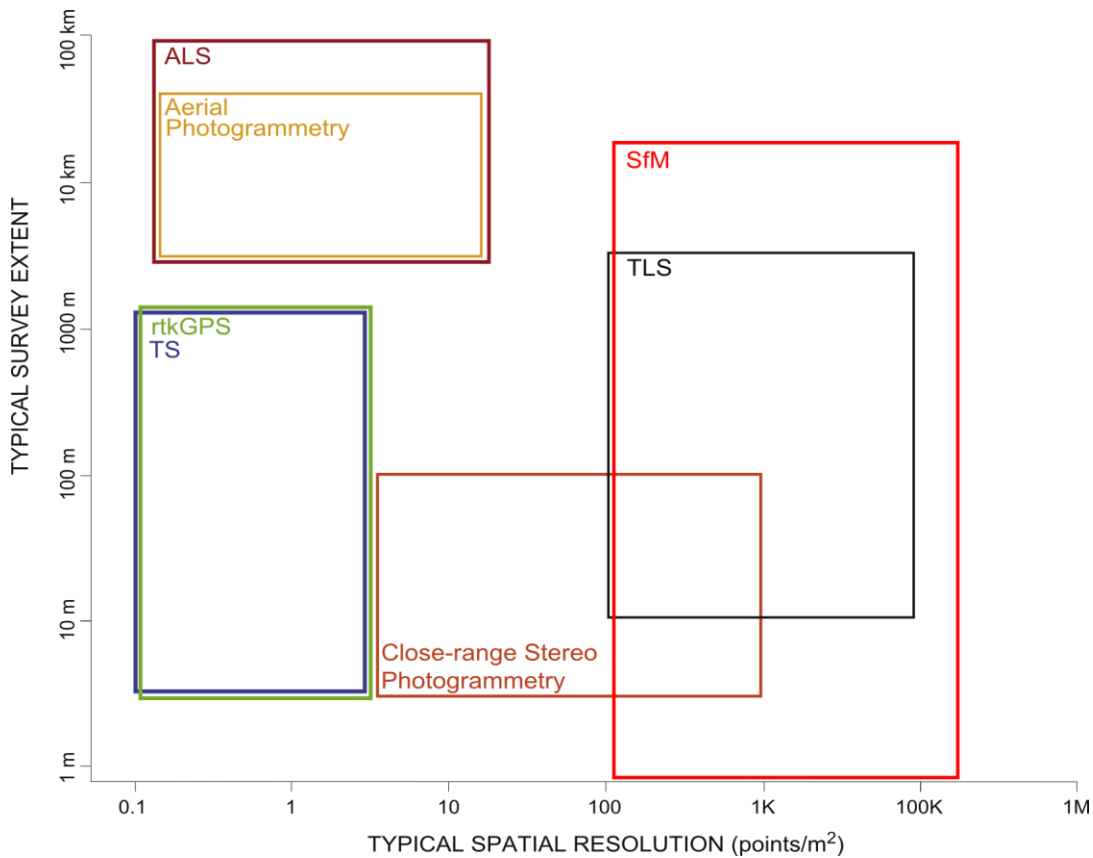


Figure 42: Comparison of topographic survey methods and their typical extents and resolutions. ALS = Airborne LiDAR, rtkGPS = real-time kinematic global positioning system, SfM = Structure-from-Motion, TLS = Terrestrial Laser Scanning, TS = Total Station (After Bangen et al., 2014).

The point cloud data that SfM produces create high quality, repeatable datasets with sufficient resolution for almost any application. All aspects of SfM surveys, from planning to collection to processing, are under the control of the researcher. This gives researchers flexibility in where, when, and how much data are collected and how the data are processed. Lastly, the simultaneous collection of imagery and three-dimensional data provide important visual context to the 3D data, especially when performing change detection studies.

SfM is still a rapidly developing technique for 3D surveys. By implementing the improvements laid out here and by other authors, SfM will be a powerful tool that will make 3D data collection more accessible to the wider geomorphic community. By

conducting this research early in the development of SfM, it will help inform the broader user community who can contribute to creating a simple set of “best practices” for SfM surveys and lay the groundwork for the successful future for this revolutionary technique.

APPENDIX
DATA MANAGEMENT

The data for this dissertation are archived on the Geography Department server. The file paths below are all located on the server named `\\cas-fs-geog`

Chapter II

- Cummins Creek photographs and GCPs
 - Projects\StructureFromMotion\MFJD_James\Cummins_Repeat
- TLS comparison data
 - Projects\StructureFromMotion\James_TLS_SfM

Chapter III

- 2012 Granite Boulder Creek Photographs and GCP data
 - Projects\StructureFromMotion\MFJD_James\2012
- 2013 Granite Boulder Creek photographs and GPS data
 - Projects\StructureFromMotion\MFJD_James\2013\GBC_SfM_2013

Chapter IV

- The final orthoimagery, DEMs, and point clouds from the helicopter flight
 - Servers\Yellowstone\MFJohnDay\Imagery\2013_sfm
- The raw photographs, GPC data, and other supporting data
 - Projects\StructureFromMotion\MFJD_James\2013\Heli

REFERENCES CITED

- Agarwal S, Furukawa Y, Snavely N, Curless B, Seitz SM, Szeliski R. 2010. Reconstructing Rome. *Computer* **43** : 40–47. DOI: 10.1109/MC.2010.175
- Agarwal S, Snavely N, Simon I, Seitz SM, Szeliski R. 2009. Building Rome in a day. presented at the Computer Vision, 2009 IEEE 12th International Conference on. 72–79 pp.
- AgiSoft LLC. 2014. PhotoScan Professional Edition v.1.0.3 . St. Petersburg, Russia [online] Available from: www.agisoft.ru
- Andrews ED. 1982. Bank stability and channel width adjustment, East Fork River, Wyoming. *Water Resources Research* **18** : 1184–1192. DOI: 10.1029/WR018i004p01184
- Angelaki V, Harbor JM. 1995. Impacts of Flow Diversion for Small Hydroelectric Power Plants on Sediment Transport, Northwest Washington. *Physical Geography* **16** : 432–443. DOI: 10.1080/02723646.1995.10642564
- Bangen SG, Wheaton JM, Bouwes N, Bouwes B, Jordan C. 2014. A methodological intercomparison of topographic survey techniques for characterizing wadeable streams and rivers. *Geomorphology* **206** : 343–361. DOI: 10.1016/j.geomorph.2013.10.010
- Bash JS, Ryan CM. 2002. Stream Restoration and Enhancement Projects: Is Anyone Monitoring? *Environmental Management* **29** : 877–885. DOI: 10.1007/s00267-001-0066-3
- Bennett SJ, Simon A, Castro JM, Atkinson JF, Bronner CE, Blersch SS, Rabideau AJ. 2011. The Evolving Science of Stream Restoration. In *Stream Restoration in Dynamic Fluvial Systems* , Simon A, Bennett SJ, and Castro JM (eds). American Geophysical Union; 1–8. [online] Available from: <http://onlinelibrary.wiley.com/doi/10.1029/2011GM001099/summary> (Accessed 31 August 2014)
- Bernhardt ES et al. 2005. Synthesizing U.S. River Restoration Efforts. *Science* **308** : 636–637. DOI: 10.1126/science.1109769
- Brasington J, Langham J, Rumsby B. 2003. Methodological sensitivity of morphometric estimates of coarse fluvial sediment transport. *Geomorphology* **53** : 299–316. DOI: 10.1016/S0169-555X(02)00320-3
- Brasington J, Rumsby BT, McVey RA. 2000. Monitoring and modelling morphological change in a braided gravel-bed river using high resolution GPS-based survey. *Earth Surface Processes and Landforms* **25** : 973–990. DOI: 10.1002/1096-9837(200008)25:9<973::AID-ESP111>3.0.CO;2-Y

- Buffington JM. 2012. Changes in Channel Morphology Over Human Time Scales. In Gravel-Bed Rivers , Church M, Biron PM, and Roy AG (eds). John Wiley & Sons, Ltd; 433–463. [online] Available from: <http://onlinelibrary.wiley.com/doi/10.1002/9781119952497.ch32/summary> (Accessed 5 November 2013)
- Butler JB, Lane SN, Chandler JH. 1998. Assessment of Dem Quality for Characterizing Surface Roughness Using Close Range Digital Photogrammetry. *The Photogrammetric Record* **16** : 271–291. DOI: 10.1111/0031-868X.00126
- Carbonneau PE. 2005. The threshold effect of image resolution on image-based automated grain size mapping in fluvial environments. *Earth Surface Processes and Landforms* **30** : 1687–1693. DOI: 10.1002/esp.1288
- Carbonneau P, Fonstad MA, Marcus WA, Dugdale SJ. 2012. Making riverscapes real. *Geomorphology* **137** : 74–86. DOI: 10.1016/j.geomorph.2010.09.030
- Chandler J. 1999. Effective application of automated digital photogrammetry for geomorphological research. *Earth Surface Processes and Landforms* **24** : 51–63. DOI: 10.1002/(SICI)1096-9837(199901)24:1<51::AID-ESP948>3.0.CO;2-H
- Cochran B. 2013. Oxbow Conservation Area Dredge Tailings Restoration Project, Phase 2 Completion Report . Confederated Tribes of the Warm Springs Reservation of Oregon Fisheries Department – Habitat Program
- Dandois JP, Ellis EC. 2013. High spatial resolution three-dimensional mapping of vegetation spectral dynamics using computer vision. *Remote Sensing of Environment* **136** : 259–276. DOI: 10.1016/j.rse.2013.04.005
- Downs PW, Kondolf GM. 2002. Post-Project Appraisals in Adaptive Management of River Channel Restoration. *Environmental Management* **29** : 477–496. DOI: 10.1007/s00267-001-0035-X
- Dugdale SJ, Carbonneau PE, Campbell D. 2010. Aerial photosieving of exposed gravel bars for the rapid calibration of airborne grain size maps. *Earth Surface Processes and Landforms* **35** : 627–639. DOI: 10.1002/esp.1936
- Fausch KD, Torgersen CE, Baxter CV, Li HW. 2002. Landscapes to Riverscapes: Bridging the Gap between Research and Conservation of Stream Fishes. *BioScience* **52** : 483–498.
- Faustini JM, Kaufmann PR, Herlihy AT. 2009. Downstream variation in bankfull width of wadeable streams across the conterminous United States. *Geomorphology* **108** : 292–311. DOI: 10.1016/j.geomorph.2009.02.005

- Ferns ML, Brooks HC. 1995. The Bourne and Greenhorn Subterranean of the Baker Terrane, Northeastern Oregon: Implications for the Evolution of The Blue Mountains Island-Arc System. In *Geology of the Blue Mountains region of Oregon, Idaho, and Washington; petrology and tectonic evolution of pre-Tertiary rocks of the Blue Mountains region*. USGS Professional Paper 1438. , Vallier LT and Brooks HC (eds). United States Geological Survey; [online] Available from: <http://pubs.er.usgs.gov/publication/pp1438> (Accessed 21 August 2014)
- Fonstad MA, Dietrich JT, Courville BC, Jensen JL, Carbonneau PE. 2013. Topographic structure from motion: a new development in photogrammetric measurement. *Earth Surface Processes and Landforms* **38** : 421–430. DOI: 10.1002/esp.3366
- Fonstad MA, Marcus WA. 2010. High resolution, basin extent observations and implications for understanding river form and process. *Earth Surface Processes and Landforms* **35** : 680–698. DOI: 10.1002/esp.1969
- Frissell CA, Liss WJ, Warren CE, Hurley MD. 1986. A hierarchical framework for stream habitat classification: Viewing streams in a watershed context. *Environmental Management* **10** : 199–214. DOI: 10.1007/BF01867358
- Furukawa Y, Ponce J. 2010. Accurate, Dense, and Robust Multiview Stereopsis. *IEEE Transactions on Pattern Analysis and Machine Intelligence* **32** : 1362–1376. DOI: 10.1109/TPAMI.2009.161
- Girardeau-Montaut D. 2014. CloudCompare [online] Available from: <http://www.cloudcompare.org/>
- Graf WL. 2000. Locational Probability for a Dammed, Urbanizing Stream: Salt River, Arizona, USA. *Environmental Management* **25** : 321–335. DOI: 10.1007/s002679910025
- Gregory SV, Swanson FJ, McKee WA, Cummins KW. 1991. An Ecosystem Perspective of Riparian Zones. *BioScience* **41** : 540–551. DOI: 10.2307/1311607
- Hartley R, Zisserman A. 2003. *Multiple View Geometry in Computer Vision* . 2nd ed. Cambridge University Press: Cambridge, UK
- Hauert J-H, Sester M. 2008. Area Collapse and Road Centerlines based on Straight Skeletons. *GeoInformatica* **12** : 169–191. DOI: 10.1007/s10707-007-0028-x
- Heritage G, Hetherington D. 2007. Towards a protocol for laser scanning in fluvial geomorphology. *Earth Surface Processes and Landforms* **32** : 66–74. DOI: 10.1002/esp.1375
- Hey R, Thorne C. 1986. Stable Channels with Mobile Gravel Beds. *Journal of Hydraulic Engineering* **112** : 671–689. DOI: 10.1061/(ASCE)0733-9429(1986)112:8(671)

- James LA, Hodgson ME, Ghoshal S, Latiolais MM. 2012. Geomorphic change detection using historic maps and DEM differencing: The temporal dimension of geospatial analysis. *Geomorphology* **137** : 181–198. DOI: 10.1016/j.geomorph.2010.10.039
- James MR, Quinton JN. 2014. Ultra-rapid topographic surveying for complex environments: the hand-held mobile laser scanner (HMLS). *Earth Surface Processes and Landforms* **39** : 138–142. DOI: 10.1002/esp.3489
- James MR, Robson S. 2012. Straightforward reconstruction of 3D surfaces and topography with a camera: Accuracy and geoscience application. *Journal of Geophysical Research: Earth Surface* **117** : F03017. DOI: 10.1029/2011JF002289
- James MR, Robson S. 2014. Mitigating systematic error in topographic models derived from UAV and ground-based image networks. *Earth Surface Processes and Landforms* : n/a–n/a. DOI: 10.1002/esp.3609
- James MR, Varley N. 2012. Identification of structural controls in an active lava dome with high resolution DEMs: Volcán de Colima, Mexico. *Geophysical Research Letters* **39** : L22303. DOI: 10.1029/2012GL054245
- Jarrett R. 1984. Hydraulics of High-Gradient Streams. *Journal of Hydraulic Engineering* **110** : 1519–1539. DOI: 10.1061/(ASCE)0733-9429(1984)110:11(1519)
- Javernick L, Brasington J, Caruso B. 2014. Modeling the topography of shallow braided rivers using Structure-from-Motion photogrammetry. *Geomorphology* **213** : 166–182. DOI: 10.1016/j.geomorph.2014.01.006
- Jett SM. 1998. Alluvial fan development in a confined montane valley, Middle Fork John Day River, eastern Oregon, MS Thesis, University of Oregon
- Knighton D. 1998. *Fluvial forms and processes: a new perspective* . Rev. and updated ed. Arnold: London ; New York
- Kondolf GM. 1994. Geomorphic and environmental effects of instream gravel mining. *Landscape and Urban Planning* **28** : 225–243. DOI: 10.1016/0169-2046(94)90010-8
- Kondolf GM. 1995. Five Elements for Effective Evaluation of Stream Restoration. *Restoration Ecology* **3** : 133–136. DOI: 10.1111/j.1526-100X.1995.tb00086.x
- Kondolf GM. 1997. Hungry Water: Effects of Dams and Gravel Mining on River Channels. *Environmental Management* **21** : 533–551. DOI: 10.1007/s002679900048
- Kondolf GM, Larson M. 1995. Historical channel analysis and its application to riparian and aquatic habitat restoration. *Aquatic Conservation: Marine and Freshwater Ecosystems* **5** : 109–126. DOI: 10.1002/aqc.3270050204
- Kondolf GM, Micheli ER. 1995. Evaluating stream restoration projects. *Environmental Management* **19** : 1–15. DOI: 10.1007/BF02471999

- Korpak J. 2007. The influence of river training on mountain channel changes (Polish Carpathian Mountains). *Geomorphology* **92** : 166–181. DOI: 10.1016/j.geomorph.2006.07.037
- Koutsoudis A, Vidmar B, Arnaoutoglou F. 2013. Performance evaluation of a multi-image 3D reconstruction software on a low-feature artefact. *Journal of Archaeological Science* **40** : 4450–4456. DOI: 10.1016/j.jas.2013.07.007
- Koutsoudis A, Vidmar B, Ioannakis G, Arnaoutoglou F, Pavlidis G, Chamzas C. 2014. Multi-image 3D reconstruction data evaluation. *Journal of Cultural Heritage* **15** : 73–79. DOI: 10.1016/j.culher.2012.12.003
- Lague D, Brodu N, Leroux J. 2013. Accurate 3D comparison of complex topography with terrestrial laser scanner: Application to the Rangitikei canyon (N-Z). *ISPRS Journal of Photogrammetry and Remote Sensing* **82** : 10–26. DOI: 10.1016/j.isprsjprs.2013.04.009
- Lane SN, Chandler JH. 2003. Editorial: the generation of high quality topographic data for hydrology and geomorphology: new data sources, new applications and new problems. *Earth Surface Processes and Landforms* **28** : 229–230. DOI: 10.1002/esp.479
- Lane SN, James TD, Crowell MD. 2000. Application of Digital Photogrammetry to Complex Topography for Geomorphological Research. *The Photogrammetric Record* **16** : 793–821. DOI: 10.1111/0031-868X.00152
- Lane SN, Richards KS, Chandler JH. 1994. Developments in monitoring and modelling small-scale river bed topography. *Earth Surface Processes and Landforms* **19** : 349–368. DOI: 10.1002/esp.3290190406
- Lane SN, Westaway RM, Murray Hicks D. 2003. Estimation of erosion and deposition volumes in a large, gravel-bed, braided river using synoptic remote sensing. *Earth Surface Processes and Landforms* **28** : 249–271. DOI: 10.1002/esp.483
- Legleiter CJ, Fonstad MA. 2012. An Introduction to the Physical Basis for Deriving River Information by Optical Remote Sensing. In *Fluvial Remote Sensing for Science and Management* , . John Wiley & Sons, Ltd; 43–69. [online] Available from: <http://dx.doi.org/10.1002/9781119940791.ch3>
- Legleiter CJ, Kyriakidis PC. 2006. Forward and Inverse Transformations between Cartesian and Channel-fitted Coordinate Systems for Meandering Rivers. *Mathematical Geology* **38** : 927–958. DOI: 10.1007/s11004-006-9056-6
- Legleiter CJ, Kyriakidis PC, McDonald RR, Nelson JM. 2011. Effects of uncertain topographic input data on two-dimensional flow modeling in a gravel-bed river. *Water Resources Research* **47** : n/a–n/a. DOI: 10.1029/2010WR009618

- Leopold LB, Maddock T. 1953. The hydraulic geometry of stream channels and some physiographic implications . United States Geological Survey [online] Available from: <http://pubs.er.usgs.gov/publication/pp252> (Accessed 17 January 2013)
- Longley PA, Goodchild MF, Maguire DJ, Rhind DW. 2011. Geographic information systems & science . Wiley: Hoboken, NJ
- Magilligan FJ, McDowell PF. 1997. Stream Channel Adjustments Following Elimination of Cattle Grazing. *Journal of the American Water Resources Association* **33** : 867–878. DOI: 10.1111/j.1752-1688.1997.tb04111.x
- Marcus WA, Fonstad MA. 2008. Optical remote mapping of rivers at sub-meter resolutions and watershed extents. *Earth Surface Processes and Landforms* **33** : 4–24. DOI: 10.1002/esp.1637
- Marcus WA, Fonstad MA. 2010. Remote sensing of rivers: the emergence of a subdiscipline in the river sciences. *Earth Surface Processes and Landforms* **35** : 1867–1872. DOI: 10.1002/esp.2094
- Marcus WA, Roberts K, Harvey L, Tackman G. 1992. An Evaluation of Methods for Estimating Manning's n in Small Mountain Streams. *Mountain Research and Development* **12** : 227–239. DOI: 10.2307/3673667
- Marston RA, Girel J, Pautou G, Piegay H, Bravard J-P, Arneson C. 1995. Channel metamorphosis, floodplain disturbance, and vegetation development: Ain River, France. *Geomorphology* **13** : 121–131. DOI: 10.1016/0169-555X(95)00066-E
- Mathews AJ, Jensen JLR. 2013. Visualizing and Quantifying Vineyard Canopy LAI Using an Unmanned Aerial Vehicle (UAV) Collected High Density Structure from Motion Point Cloud. *Remote Sensing* **5** : 2164–2183. DOI: 10.3390/rs5052164
- May C, Roering J, Eaton LS, Burnett KM. 2013. Controls on valley width in mountainous landscapes: The role of landsliding and implications for salmonid habitat. *Geology* **41** : 503–506. DOI: 10.1130/G33979.1
- McDowell PF. 2001. Spatial Variations in Channel Morphology at Segment and Reach Scales, Middle Fork John Day River, Northeastern Oregon. In *Geomorphic Processes and Riverine Habitat* , Dorava JM, Montgomery DR, Palcsak BB, and Fitzpatrick FA (eds). American Geophysical Union; 159–172. [online] Available from: <http://onlinelibrary.wiley.com/doi/10.1029/WS004p0159/summary> (Accessed 18 August 2014)
- McGlone JC, Lee GY. (eds). 2013. Manual of photogrammetry . 6th ed. American Society for Photogrammetry and Remote Sensing: Bethesda, Md.
- Milan DJ, Heritage GL, Large ARG, Fuller IC. 2011. Filtering spatial error from DEMs: Implications for morphological change estimation. *Geomorphology* **125** : 160–171. DOI: 10.1016/j.geomorph.2010.09.012

- Montgomery DR, Buffington JM. 1998. Channel processes, classification, and response. In *River ecology and management: lessons from the Pacific coastal ecoregion*, Naiman RJ and Bilby RE (eds). Springer: New York;
- Mowrer HT. 2000. Accuracy (re)assurance: Selling uncertainty assessment to the uncertain. In *Spatial Accuracy Assessment: Land Information Uncertainty in Natural Resources*, Lowell K and Jaton A (eds). CRC Press;
- NOAA. 2005. Endangered and Threatened Species; Designation of Critical Habitat for 12 Evolutionarily Significant Units of West Coast Salmon and Steelhead in Washington, Oregon, and Idaho (50 CFR Part 226). *Federal Register* **70**
- Olsen M, Johnstone E, Driscoll N, Ashford S, Kuester F. 2009. Terrestrial Laser Scanning of Extended Cliff Sections in Dynamic Environments: Parameter Analysis. *Journal of Surveying Engineering* **135** : 161–169. DOI: 10.1061/(ASCE)0733-9453(2009)135:4(161)
- Ouédraogo MM, Degré A, Debouche C, Lisein J. 2014. The evaluation of unmanned aerial system-based photogrammetry and terrestrial laser scanning to generate DEMs of agricultural watersheds. *Geomorphology* **214** : 339–355. DOI: 10.1016/j.geomorph.2014.02.016
- Palmer M a. et al. 2005. Standards for ecologically successful river restoration. *Journal of Applied Ecology* **42** : 208–217. DOI: 10.1111/j.1365-2664.2005.01004.x
- Palmer MA, Allen JD. 2006. Restoring Rivers. *Issues in Science and Technology* **Winter 2006** [online] Available from: <http://www.issues.org/22.2/palmer.html>
- Pavelsky TM, Smith LC. 2008. RivWidth: A Software Tool for the Calculation of River Widths From Remotely Sensed Imagery. *IEEE Geoscience and Remote Sensing Letters* **5** : 70–73. DOI: 10.1109/LGRS.2007.908305
- Pizzuto JE. 2008. Streambank Erosion and River Width Adjustment. In *Sedimentation Engineering*, . American Society of Civil Engineers; 387–438. [online] Available from: <http://ascelibrary.org/doi/abs/10.1061/9780784408148.ch07> (Accessed 26 August 2014)
- Poole GC. 2002. Fluvial landscape ecology: addressing uniqueness within the river discontinuum. *Freshwater Biology* **47** : 641–660. DOI: 10.1046/j.1365-2427.2002.00922.x
- Raleigh RF, Miller WJ, Nelson PC. 1986. Habitat Suitability Index Models and Instream Flow Suitability Curves: Chinook Salmon . Biological Report. U.S. Fish and Wildlife Service [online] Available from: <http://www.nwrc.usgs.gov/wdb/pub/hsi/hsi-122.pdf>
- Richards KS. 1976. Channel width and the riffle-pool sequence. *Geological Society of America Bulletin* **87** : 883–890. DOI: 10.1130/0016-7606(1976)87<883:CWATRS>2.0.CO;2

- Richards KS, Wood R. 1977. Urbanization, water redistribution, and their effect on channel processes. In *River channel changes*, Gregory KJ (ed). Wiley: Chichester; New York; 369–388.
- Risley J, Stonewall A, Haluska T. 2008. Estimating Flow-Duration and Low-Flow Frequency Statistics for Unregulated Streams in Oregon . Scientific Investigations Report. U.S. Geological Survey: Reston, VA
- Roni P, Beechie TJ, Bilby RE, Leonetti FE, Pollock MM, Pess GR. 2002. A Review of Stream Restoration Techniques and a Hierarchical Strategy for Prioritizing Restoration in Pacific Northwest Watersheds. *North American Journal of Fisheries Management* **22** : 1–20. DOI: 10.1577/1548-8675(2002)022<0001:AROSRT>2.0.CO;2
- Ryan S. 1997. Morphologic Response of Subalpine Streams to Transbasin Flow Diversion. *Journal of the American Water Resources Association* **33** : 839–854. DOI: 10.1111/j.1752-1688.1997.tb04109.x
- Schwartz JJ, Snoke AW, Frost CD, Barnes CG, Gromet LP, Johnson K. 2009. Analysis of the Wallowa-Baker terrane boundary: Implications for tectonic accretion in the Blue Mountains province, northeastern Oregon. *Geological Society of America Bulletin* : B26493.1. DOI: 10.1130/B26493.1
- Sharp HO. 1951. *Practical Photogrammetry* . Macmillan Company: New York
- Snively KN. 2008. Scene reconstruction and visualization from Internet photo collections, Ph.D., University of Washington
- Snively N, Seitz SM, Szeliski R. 2006. Photo tourism. presented at the ACM SIGGRAPH 2006 Papers. Boston, Massachusetts. 835 pp. [online] Available from: <http://portal.acm.org/citation.cfm?doid=1179352.1141964> (Accessed 14 December 2010)
- Snively N, Seitz SM, Szeliski R. 2007. Modeling the World from Internet Photo Collections. *International Journal of Computer Vision* **80** : 189–210. DOI: 10.1007/s11263-007-0107-3
- Szeliski R, Kang SB. 1994. Recovering 3D Shape and Motion from Image Streams Using Nonlinear Least Squares. *Journal of Visual Communication and Image Representation* **5** : 10–28. DOI: 10.1006/jvci.1994.1002
- Taylor JR. 1997. *An introduction to error analysis: the study of uncertainties in physical measurements* . University Science Books: Sausalito, Calif.
- Trimble SW, Mendel AC. 1995. The cow as a geomorphic agent — A critical review. *Geomorphology* **13** : 233–253. DOI: 10.1016/0169-555X(95)00028-4

- Ullman S. 1979. *The Interpretation of Visual Motion* . MIT Press: Cambridge, Mass
- U.S. Fish & Wildlife Service. 2010. *Bull Trout Final Critical Habitat Justification: Rationale for Why Habitat is Essential, and Documentation of Occupancy* . Portland, Oregon
- U.S. Geological Survey. 2012. *The StreamStats program for Oregon* [online] Available from: <http://water.usgs.gov/osw/streamstats/oregon.html>
- Vannote R, Minshall G, Cummins K, Sedell J, Cushing C. 1980. The river continuum concept. *Canadian Journal of Fisheries and Aquatic Sciences* **37** : 130–137.
- Walther SC, Marcus WA, Fonstad MA. 2011. Evaluation of high-resolution, true-colour, aerial imagery for mapping bathymetry in a clear-water river without ground-based depth measurements. *International Journal of Remote Sensing* **32** : 4343–4363. DOI: 10.1080/01431161.2010.486418
- Ward JV, Stanford JA. 1995. The serial discontinuity concept: Extending the model to floodplain rivers. *Regulated Rivers: Research & Management* **10** : 159–168. DOI: 10.1002/rrr.3450100211
- Wechsler SP, Kroll CN. 2006. Quantifying DEM Uncertainty and its Effect on Topographic Parameters. *Photogrammetric Engineering & Remote Sensing* **72** : 1081–1090.
- Westoby MJ, Brasington J, Glasser NF, Hambrey MJ, Reynolds JM. 2012. “Structure-from-Motion” photogrammetry: A low-cost, effective tool for geoscience applications. *Geomorphology* **179** : 300–314. DOI: 10.1016/j.geomorph.2012.08.021
- Wheaton JM, Brasington J, Darby SE, Sear DA. 2010. Accounting for uncertainty in DEMs from repeat topographic surveys: improved sediment budgets. *Earth Surface Processes and Landforms* **35** : 136–156. DOI: 10.1002/esp.1886
- Whittaker AC, Cowie PA, Attal M, Tucker GE, Roberts GP. 2007. Bedrock channel adjustment to tectonic forcing: Implications for predicting river incision rates. *Geology* **35** : 103–106. DOI: 10.1130/G23106A.1
- Wohl E, Angermeier PL, Bledsoe B, Kondolf GM, MacDonnell L, Merritt DM, Palmer MA, Poff NL, Tarboton D. 2005. River restoration. *Water Resources Research* **41** : W10301. DOI: 10.1029/2005WR003985
- Woodget AS, Carbonneau PE, Visser F, Maddock I. 2014. Quantifying submerged fluvial topography at hyperspatial resolutions with UAS imagery and SfM-photogrammetry. *Earth Surface Processes and Landforms* DOI: 10.1002/esp.3613
- Yamazaki D, O’Loughlin F, Trigg MA, Miller ZF, Pavelsky TM, Bates PD. 2014. Development of the Global Width Database for Large Rivers. *Water Resources Research* **50** : 3467–3480. DOI: 10.1002/2013WR014664

Yuan X. 2009. Quality assessment for GPS-supported bundle block adjustment based on aerial digital frame imagery. *The Photogrammetric Record* **24** : 139–156. DOI: 10.1111/j.1477-9730.2009.00527.x

Zhang J, Goodchild MF. 2002. *Uncertainty in geographical information* . Taylor & Francis: London ; New York